ULTRASOUND MATERIAL CHARACTERIZATION OF COMPLEX MATRIX MATERIAL AND MITIGATION OF NOISE USING SIGNAL PROCESSING TECHNIQUES

by

Shwetha Jakkidi

A Dissertation
Submitted to the
Graduate Faculty
of
George Mason University
in Partial Fulfillment of
The Requirements for the Degree
of
Doctor of Philosophy
Electrical and Computer Engineering

Committee:

| | |
|---|---|
| _____ | Dr. Gerald Cook, Dissertation Director |
| _____ | Dr. Jill Nelson, Committee Member |
| _____ | Dr. Brian Mark, Committee Member |
| _____ | Dr. Siddhartha Sikdar, Committee Member |
| _____ | Dr. James C.P McKeon, Committee Member |
| _____ | Dr. Monson H. Hayes, Department Chair |
| _____ | Dr. Kenneth S. Ball, Dean, The Volgenau School of Engineering |
| Date: _____ | Fall 2015<br>George Mason University<br>Fairfax, VA |

# Ultrasound Material Characterization of Complex Matrix Material and Mitigation of Noise using Signal Processing Techniques

A Dissertation submitted in partial fulfillment of the requirements for the degree of Doctor of Philosophy at George Mason University

by

Shwetha Jakkidi
Master of Science
George Mason University, 2002
Bachelor of Engineering
Manukau Institute of Technology (Auckland, New Zealand), 2000

Director: Gerald Cook, Earle C. Williams Professor
Department of Electrical and Computer Engineering

Fall Semester 2015
George Mason University
Fairfax, VA

## DEDICATION

To my wonderful daughter Divika.

To my loving and supportive parents, Manohar and Aruna.

## ACKNOWLEDGEMENTS

I came to George Mason University in fall of 2000 for my M.S degree. After successfully completing my thesis with Dr. Gerald Cook as my advisor I decided to work in industry. After working for a couple of years, I enrolled in the Ph.D. program on a part-time basis while working for Sonix, Inc. I have met many wonderful people who have contributed to this thesis and my personal development. First, I would like to thank my committee members: Gerald Cook, Brian Mark, Jill Nelson, Siddhartha Sikdar and Jim McKeon. In particular, I would like to thank Dr. Gerald Cook for once again serving as my advisor throughout the Ph.D. program and his invaluable support and encouragement on all of my academic work. I want to thank Dr. Jim McKeon for hiring me at Sonix, Inc and teaching me everything I know about Ultrasonic Inspection for Non Destructive testing. His knowledge and guidance has been the foundation to my success in my career and this research work.

After completing my course work and passing the hurdle of qualifying for the Ph.D, I took a break for 3 years. I relocated to California for my job, had a child and was contemplating whether to go back and finish my research. I would like to thank Dave Carr, who was the general manager at Sonix, Inc at that time for encouraging me to take the last few sprints to finish my research, Rick Gravley, Director of Sales and Marketing and Brandon Edlefsen, General Manager at Sonix, Inc for always believing in me and encouraging me to explore my strengths and take on new challenges. I would like to thank all of my colleagues at Sonix, Inc for their valuable support through the last 11 years.

I would like to thank Ashour Kamber from Silicon Turnkey Solutions for dedicating resources, time and helping me make samples for this research work. Thank you to all my friends, especially Deepthi and Goutham Chilamkuri, Lakshmi Kalahasthi, Debamita and Swapna for helping me and supporting me in my personal life so that I could dedicate time towards my research.

I owe it to my family for everything I am today. I would like to thank my mum and dad for their unconditional support, love and encouragement. Special thanks to Sandeep Jakkidi, my brother and Shravanthi Kallem, my sister-in-law for their guidance. I would like to show my gratitude to my six year old daughter, Divika for understanding that I am unable to spend time with her that she rightfully deserves. She made me realize that it is better to try and fail than not try at all. All the things I have asked her to do in order to learn and progress have applied to me in these last years when I wanted to give up. As a mother, I want to lead by example and I hope that sometime in the future this Ph.D. journey will be my success story that I share with her.

## TABLE OF CONTENTS

## LIST OF TABLES

Table Page

## LIST OF FIGURES

## ABSTRACT

ULTRASOUND MATERIAL CHARACTERIZATION OF COMPLEX MATRIX MATERIAL AND MITIGATION OF NOISE USING SIGNAL PROCESSING TECHNIQUES

Shwetha Jakkidi, Ph.D.

George Mason University, 2015

Dissertation Director: Dr. Gerald Cook

Ultrasonic inspection as a non-destructive technique is used to inspect various materials for subsurface defects caused by air, cracks, material variation etc. Sometimes particles are added to clean materials to improve the strength and thermal conductivity of the material. While this improves the material properties, the presence of these particles causes attenuation of the ultrasonic signal, loss of signal strength and also signal scattering. Due to this, imaging subsurface interfaces with the complex matrix material as a primary interface is challenging. The images from subsurface interfaces are noisy and the features are not well resolved. This dissertation addresses the development of a transfer function for the noise caused by the filler particles that corrupts the ultrasonic signal. The transfer function is based on frequency domain transform of modeled ultrasonic reflection from clean material and modeled ultrasonic reflection from the complex matrix material with particles in the size range of 150um-250um. A real sample with particles was made and imaged ultrasonically. The transfer function was

applied to the A-scan data from the sample with particles to assess the performance of the transfer function for this application. The transfer function approach was extended to a case where the sample has a pattern on the back wall to assess the performance of this method.

It was concluded that the transfer function was effective in improving the quality of the image by mitigating the shadow effects caused by the presence of filler particles in the propagation path of the ultrasound.

# CHAPTER 1: INTRODUCTION

Ultrasound has been used in various applications such as medicine, SONAR, and Non-Destructive testing (NDT) [1][2][3] applications in aerospace, electronics, transportation field to monitor cracks in rail tracks, nuclear industry for defect detection and to monitor the health of nuclear reactors, composites etc. Ultrasonic Imaging has become a very common method in non-destructive testing and quality assurance of materials, because of its ease of use and its high reliability. Nevertheless, the quality of ultrasonic images can be seriously degraded when the signal-to-noise ratio of the flaw target and its surrounding grain reflections is small [4].

## 1.1 Background

Ultrasonic signal is often scattered due to particles in its propagation path causing the signal to be distorted and resulting in poor image quality. The concept of signal scattering due to graininess of a material is not uncommon and has been explored previously. There has been abundant research conducted in improving the flaw to grain signal to noise ratio in materials where grain sizes can cause signal scattering resulting in weaker and corrupted signal returned from the back wall of the material [ 5 - 12]. Stainless steel, titanium and composite material samples were a popular choice to show the improvement in the flaw to grain signal to noise ratio [13]. Some key assumptions

behind the mathematical modeling were that the material is linear, homogenous, isotropic etc. However, the samples were thick (several inches) and the grain sizes were several millimeters across. Low frequency transducers (<1MHz) were used to inspect these samples as lower frequency transducers have greater penetration. Also, the research was focused on improving the flaw signal compared to the area around it. The flaws of interest are caused by air. Air is a strong reflector of ultrasound and therefore the reflected signal is relatively stronger than that of the area around it.

## 1.2 Motivation: Complex Matrix Material

Over the last two decades there have been major advancements in electronics resulting in thinner and more compact designs. These in turn have driven technological developments in ultrasonic inspection not only in terms of higher frequency transducer designs but also in signal processing and image processing to detect and image smaller defects and features.

Recently, a complex matrix material has come into use as an outside coating on samples that were previously inspected with no coating. With ever-finer area-array, lead spacing, thinner packages and smaller device feature size, control of highly filled molding compound's properties and processing parameters become more important to satisfy the needs of current and new technologies. This is especially important to the electrical devices used in a high temperature environment. The properties and distribution of the binders and filler particles affect properties like coefficient of thermal expansion (CTE) and stiffness, both of which determine the package stresses and thus contribute to

reliability [14-15]. Imaging the sub-surface interfaces without this material serving as the surface gives exceptional image quality and features can be imaged or detected down to 5um in spatial resolution.

An example image of an internal interface of an electronics component is shown along with the ultrasonic signal (A-scan) at a single x-y location in Figure 1b. It can be noted from the A-scan that there is a clear separation between the ultrasonic signal from the surface and the bond interface. Also, the features from the bond interface are well resolved in Figure 1a.

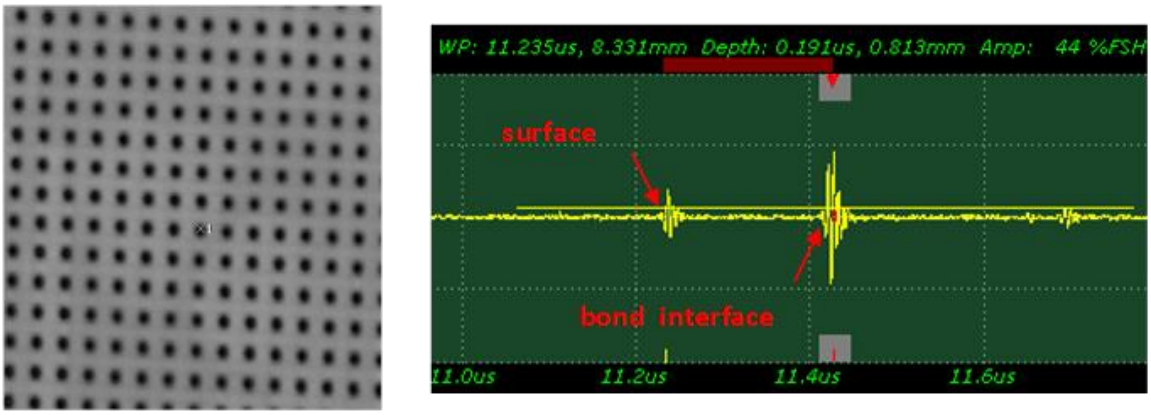


**(a)** **(b)**

**Figure 1: (a) internal interface of an electronic component; (b) A-scan with reflected signal for a clean sample**

The addition of the complex matrix material as a surface material however distorts or corrupts the ultrasonic signal making it difficult to resolve the features at deeper interfaces. An example image from the bond interface for this case is shown in Figure 2a along with the ultrasonic signal (A-scan) at a single x-y location as shown in Figure 2b. It was noted that the signal separation between the surface and the bond

interface has reduced. Also, the image from the bond interface in Figure 2a is of poor quality compared to the image shown in Figure 1a.

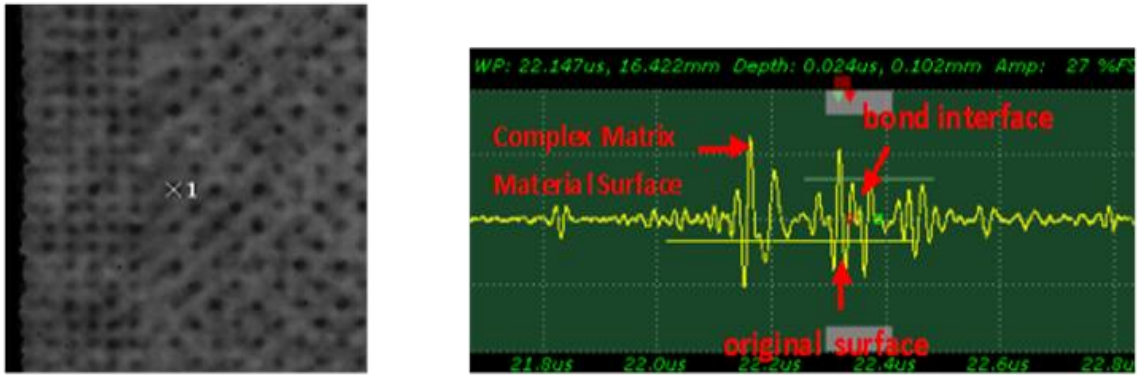


**(a)** **(b)**

**Figure 2: (a) Internal interface of an electronic component with complex matrix material coating; (b) A-scan with reflected signal for complex matrix material sample**

The complex matrix material is a homogeneous material with filler particles mixed into it. The filler particles can be of various sizes, oval in shape and different orientation to each other. These properties of the filler particles make this complex matrix material non-homogeneous and non-linear causing scattering of the ultrasonic signal resulting in distortion and corruption of this signal. To overcome the effects of the filler particles, it is necessary to understand the properties of the filler particles' size and distribution in order to model the noise. The effect of filler particles' size and filler content dispersion on ultrasonic signal has been studied. The experimental results showed that when a filler particle has a mean diameter (D) that is smaller than the sound

wavelength (λ), the ratio of λ to D is in the Rayleigh scattering region. Therefore, the effect of scattering was reduced dramatically resulting in clear ultrasonic images [16].

## 1.3 Objectives

The idea behind this research work is to improve image quality of a backwall in resin sample in the presence of filler particles whose size is not similar to the value determined by the theory of Rayleigh Scattering. The reflection of the signal from a feature may not be as strong as a signal reflected from a flaw and only marginally stronger or even weaker than the signal from the area around it in terms of amplitude. The samples of interest could be no more than 1-2mm in thickness and the filler particles in the range of 150um-250um. A 75MHz transducer will be used to inspect these samples.

### 1.3.1 Modeling of Ultrasonic Reflections

Modeling of the ultrasonic reflections is an important step in determining the appropriate noise mitigating technique. First, ultrasonic reflections from a clean resin sample were modeled. The resulting signal was compared with a real signal from a clean resin sample. The signals were overlapped to determine the correlation between the two data sets. It is assumed that the filler particles were made of glass, spherical and in the size range of 150um-250um. A resin sample with filler particles mixed into it was imaged to understand the obstructions caused by these particles.

### 1.3.2 Noise Mitigation - Method and Contribution

The main problem that this dissertation addresses is that of developing a transfer function to mitigate noise caused by filler particles in resin material. The results obtained by applying the transfer function to corrupted modeled signal are discussed. The transfer function is also applied to signals from a real resin sample with filler particles to mitigate the noise. The image is reconstructed from the filtered signals to show improvement. The transfer function is also applied to a case where there is a pattern on the backwall of the resin. The effectiveness of the transfer function based approach on this type of sample is evaluated.

## 1.4 Organization

In Chapter 2, an overview of Ultrasonic Inspection as a Non-destructive technique is provided to give an understanding of the context, applicability and foundation for the rest of the dissertation. A review of literature related to modeling ultrasonic reflections and the method chosen for the purpose of this dissertation is discussed in Chapter 3. Chapter 4 discusses the literature related to noise mitigation and the methodology used in this dissertation. Chapter 5 discusses simulated data and the results obtained using the transfer function approach to remove the effect of filler particles. Chapter 6 discusses results from real samples and the performance for the transfer function method. The overall conclusions, limitations and future work are discussed in Chapter 7.

# CHAPTER 2: ULTRASONIC THEORY FOR NON-DESTRUCTIVE TESTING - BACKGROUND

Ultrasound has been used as a non-destructive technique for over six decades. Ultrasonic waves are sound waves above 20 KHz. These waves are not audible to the human ear. These waves propagate freely through liquids and solids, are capable of being focused in straight transmission, interact differently with material flaws compared to the area surrounding it and are harmless to the human body.

## 2.1 Ultrasonic Inspection Setup

An ultrasonic inspection setup for pulse-echo or reflective mode inspection is shown in Figure 3. A transducer is used to produce a high frequency sound wave. Since higher frequencies cannot propagate through air, a coupling medium is required so that the ultrasonic waves can interact with the sample. Due to the properties and availability of water, it is the most commonly used couplant. In this inspection mode, the transducer is a transmitter as well as a receiver. Since pulse echo inspection does not require the ultrasound to penetrate through the entire sample, high frequency (>50MHz) transducers can be used to inspect the sample based on its material properties and thickness. Using this inspection mode, one can identify signals corresponding to the various interfaces and isolate defects to specific interfaces. The spatial resolution is superior and in some cases can detect down to 5um resolution.

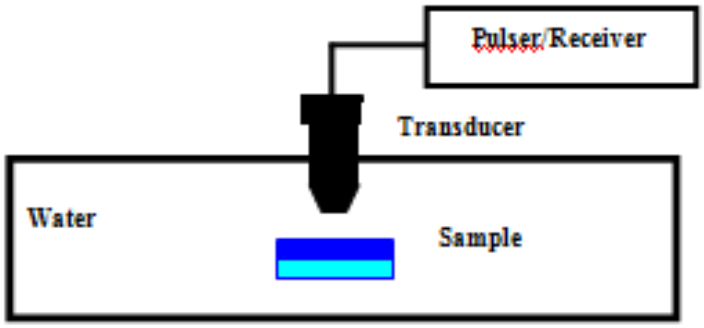


**Figure 3: Ultrasonic Inspection setup for Pulse-Echo Scan**

## 2.2 Data Representation

Various formats are used to collect and display Ultrasonic data. The three most common formats known in the non-destructive inspection area are A-scan, B-scan and C-scan. Each display mode provides a different approach to looking at and evaluating the area of interest in a material that is being inspected. With evolution in modern computerized ultrasonic scanning systems, data can be displayed in all three imaging formats simultaneously [17].

### 2.2.1 A-scan

The A-scan is an oscilloscope reading from a transducer at a single x-y location on the sample that is being inspected. The time it takes for the ultrasonic pulse to travel through the couplant to the sample and through the sample material is displayed on the horizontal axis of the oscilloscope. It also represents the physical depth within the sample that is being inspected. The amplitude of the reflected signal is displayed on the vertical axis of the oscilloscope [18]. Therefore, the amount of received ultrasonic energy is

displayed as the function of time in the A-scan. In other words, the relative amplitude of the received reflected signal is plotted along the vertical axis and the time taken for the ultrasound to propagate through the material is displayed on the horizontal axis. An example of an A-scan is shown in Figure 4. Most instruments in the industry today that have an A-scan display allow the signal to be displayed in its natural radio frequency (RF) form as either the positive or negative half of the RF signal or as a fully rectified RF signal [17].

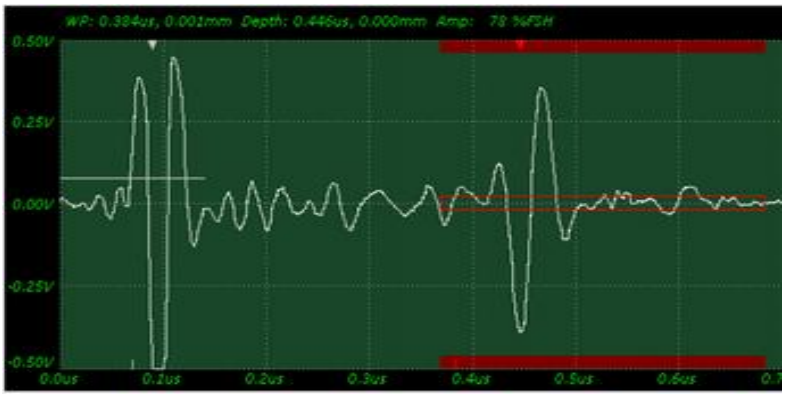


**Figure 4: Example A-scan - Courtesy Sonix, Inc.**

In the A-scan display mode, the signal from a defect such as a void, delamination, crack or material/density variation can be compared to the amplitude of the signal from the area around it. The time of occurrence of these defects can also be determined by noting the position of the signal on the horizontal axis. The time along with the acoustic longitudinal velocity of the material of ultrasonic propagation is used to determine the

depth in (mm). As an example, a gate (red box) shown in Figure 4 is used to collect information at specific depths as determined by the placement and length of the gate.

### 2.2.2 B-scan

The B-scan display mode is a cross-section view of the sample being inspected. A B-scan is produced by moving the transducer along a scan line on the sample. The A-scans along the scan line when combined together produce a B-scan curtain [18]. In the B-scan, the vertical axis represents the travel time or time-of-flight of the sound energy in the material and the horizontal axis represents the linear position of the transducer on the sample. The positive amplitudes are plotted as bright lines and negative amplitudes are plotted as dark lines. The approximate linear dimensions in scan direction and the depth of the reflector can be determined from a B-scan. To obtain a B-scan, a trigger gate is placed on the reflections of interest in the A-scan. A point is produced in the B-scan whenever the intensity of the signal is enough to trigger the gate. Either the sound reflecting from the backwall of the sample or from small features/defects within the material can trigger the gate [17].

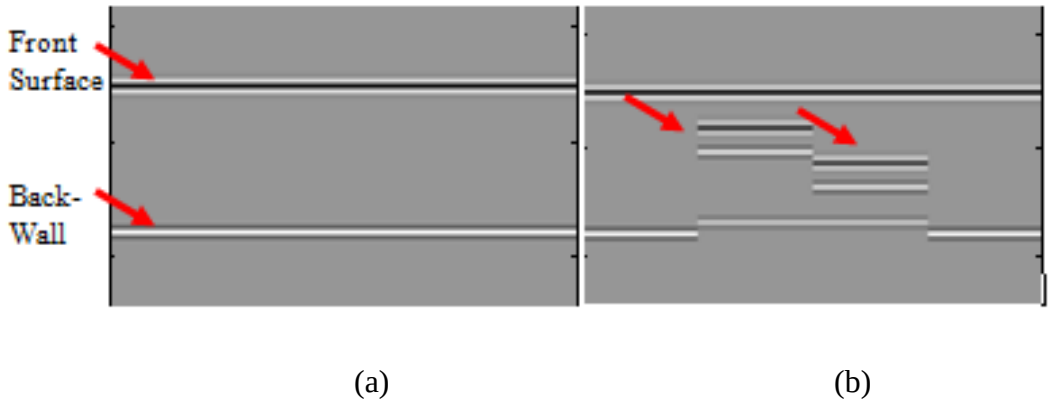


(a) (b)

**Figure 5: (a) B-scan with surface and backwall (b) B-scan with inclusion in the bulk of the material**

In the B-scan image shown in Figure 5a, the front surface and backwall interfaces have been indicated. When a particle is present, the depth at which the particle occurs is seen. Also, the backwall interface is shifted and has weaker amplitude. This is illustrated in Figure 5b. When the transducer is over particles, lines that are similar to the length of the particles and depths at which these particles occur within the material are shown on this B-scan. It should be noted that a limitation to this display technique is that the presence of larger reflectors near the surface may mask the presence of smaller reflectors within the material.

### 2.2.3 C-scan

The C-scan display mode provides a two-dimensional view of the location and size of features and defects from a specific depth of the test sample. The surface of the sample is parallel to the face of the transducer. An automated data acquisition system such as an immersion scanning system controlled by a computer is used to produce C-scans. Usually, a data collection gate is placed on the A-scan. As the transducer is

scanned over the test sample, the amplitude of the signal of interest or the time-of-flight of the signal is recorded at regular intervals. Either a gray scale or color palette is used to display the relative signal amplitude or the time-of-flight for each of the positions where data was recorded [17]. The C-scan display mode provides an image of the features that reflect and scatter the sound within and on the surfaces of the test sample. The size of a flaw or feature and position can be determined from the resulting data [18].

A dime sample was covered with resin material and a side view sketch is shown in Figure 6a. The sample was scanned to image the resin to the dime interface. The resulting image is shown in Figure 6b. The features on the dime can be seen. High resolution scans can produce very detailed images. The gate was setup to capture the amplitude of the sound reflecting from the resin to dime interface for the sample. Light areas in the image indicate areas that reflected a greater amount of energy back to the transducer.

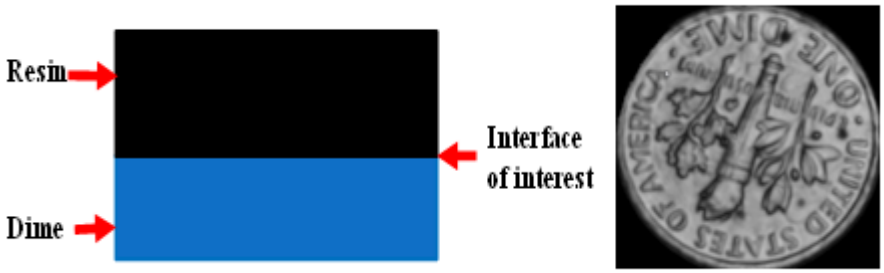


(a) (b)

**Figure 6: (a) Side view of the sample (b) C-scan image from the resin to the dime interface *Courtesy Sonix, Inc**

## 2.3 Ultrasonic Propagation Path

The setup used to scan a bulk resin sample is shown in Figure 7. As mentioned before, in pulse-echo inspection mode, the transducer acts as both a transmitter and receiver of the ultrasonic signal. The ultrasound interacts with a resin material without any features, flaws or particles in it. The reflection from the surface of the sample and the backwall of the sample are received by the same transducer. The resulting A-scan from a clean area in a resin sample is shown in Figure 8. The reflection from the front surface of the sample was noted at 14.55us and the reflection from the back wall of the sample was noted at 14.8us in this A-scan.

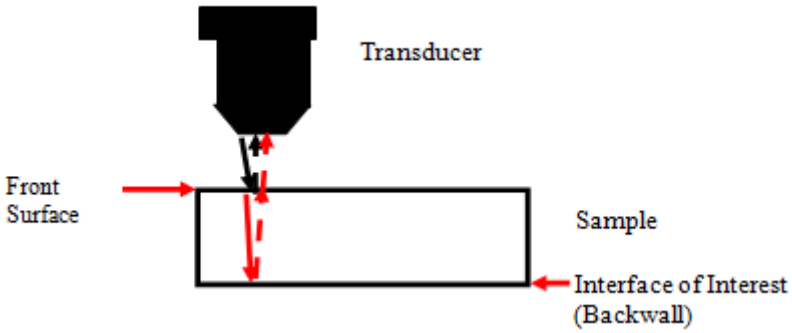


**Figure 7: Ultrasonic Signal in a Clean Sample**

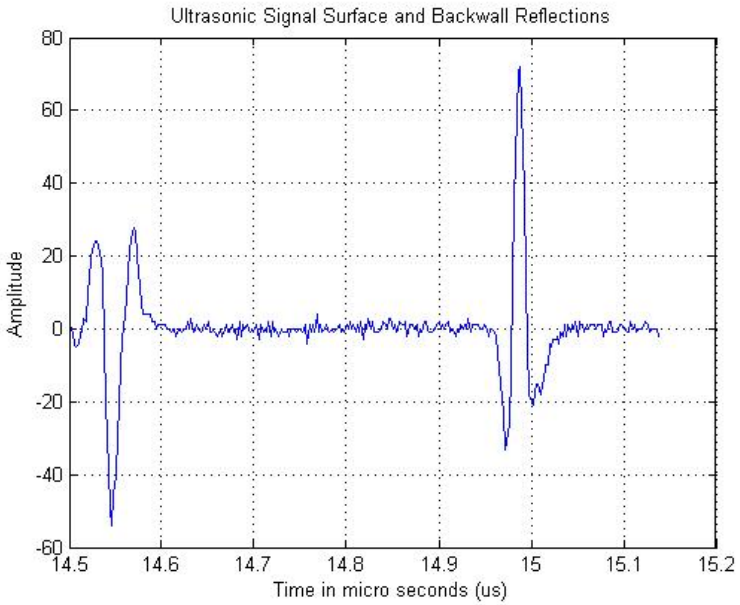


**Figure 8: A-scan from clean resin sample**

When the ultrasound interacts with a material that has filler particles in it, these fillers can cause the signal to scatter causing signal attenuation. This has been illustrated in Figure 9.

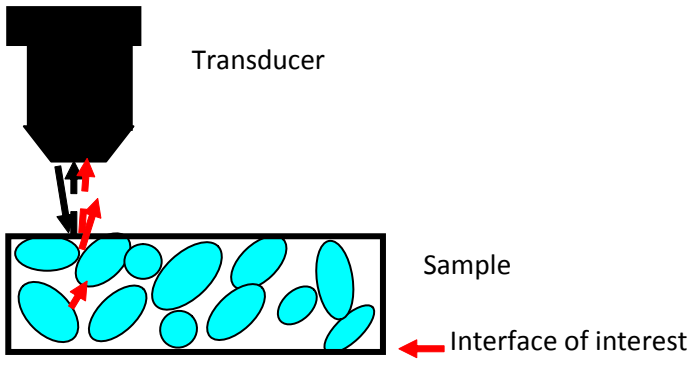


**Figure 9: Ultrasonic Signal in a Filler Particle Sample**

The resulting A-scan from location where there is a filler particle present in the propagation path of the Ultrasonic signal is shown in Figure 10.The front surface reflection was noted at 14.55us and three reflections were noted between 14.8us and 15.1us.

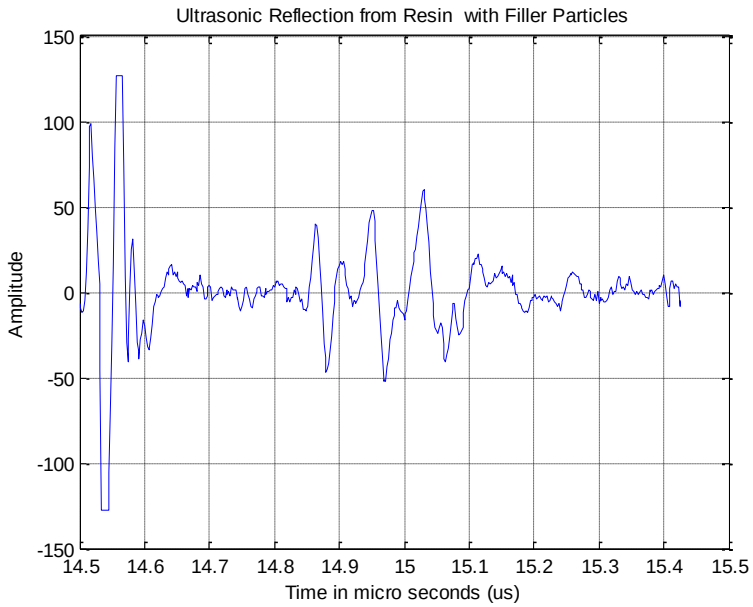


**Figure 10: A-scan from resin sample with filler particles**

# CHAPTER 3: MODELING OF ULTRASONIC REFLECTIONS

It is a well-known fact that the presence of background noise in the measured signal due to the grain boundaries and microstructure is one of the possible limitations in ultrasonic non-destructive testing. It makes it difficult to detect potential defects such as voids, cracks or delaminations inside a material due to the structural noise that scatters the ultrasonic signal [19] 20] [21].

Such materials have wide use in the industry. Some examples of these materials are stainless steel pipes that are used in nuclear plants, concrete and composite materials that are used in construction and aeronautical industries respectively. The grain boundaries in the case of stainless steel act as an impedance contrast. Sometimes the amplitude of the noise can become even higher than the amplitude of the reflection from defects within the structure. The quality of inspection is compromised as a result of this. Scattering models can be used to predict the performance of ultrasonic inspection in complex media [20]. The scattering and absorption can result in loss of signal energy when the ultrasonic signal passes through such material. Both scattering and absorption are functions of frequency and grain size distribution in large grained materials such as polycrystallines.

## 3.1 Background: Modeling of Ultrasonic Backscattered Echoes

In order to understand the Pulse-Echo reflection from the back wall of complex matrix material using a transducer, a parametric model that would best represent the reflection from the material without filler particles is desired.

With technological advancements in ultrasonic digital instruments, a significant amount of work has been focused on using digital signal processing and algorithms to extend the measuring capabilities of these instruments. The ultrasonic signals are digitized and then real-time signal processing is performed to provide the measurement result. Therefore, system engineering techniques can be used to mathematically describe the ultrasonic measurement [22].

Several different parametric and non-parametric techniques have been used to model materials of known structures [23-27]. Freemantle et al. use a $z$-transform technique [23] to inverse filter the reverberant echoes from a thin first layer to locate flaws in underlying layers, and in [24] a V (z) curve method was applied to a multi-layered thin film system. The techniques in [25-27] estimate properties (thickness, phase velocity, density, attenuation) from within the multi-layered structure in a successful manner, but these techniques usually do not provide information of the entire material structure.

A technique where a series of impulses are used to model the ultrasonic signal traveling through a multilayer structure has been described in [28]. Here the amplitudes

are the reflection coefficients at the interfaces and the position in time is the time- of-flight between the interfaces.

A model-based estimation has been proposed recently [29, 30], which uses a space-alternating generalized expectation-maximization algorithm (SAGE) to model the ultrasonic echo signals and estimate the thickness of the thin layers with high precision, accuracy and computational efficiency. The method is based on modeling the ultrasound as a superposition of Gaussian wavelets. Consequently, the multilayer signal can be represented by a sum of amplitude modulated and time delayed Gaussian echoes [31]. The advantage of this approach is that it translates a complex N-echo estimation problem into a series of one- echo estimation problems thus providing computational versatility and flexibility.

The parametric models for back-scattered echoes from a sample that has been developed in earlier research work [22] [32] are of interest. The patterns of ultrasonic backscattered echoes represent valuable information pertaining to the geometric shape, size and orientation of reflectors as well as the microstructure of the propagation path. Accurate estimation of the ultrasonic echo pattern is essential in determining the object or propagation path properties. The Ultrasonic backscattered echoes were modeled in terms of superimposed Gaussian echoes. Each Gaussian echo in the model is a nonlinear function of a set of parameters: echo bandwidth, arrival time, center frequency, amplitude and phase. These parameters are sensitive to the echo shape and can be linked to the physical properties of reflectors and frequency characteristics in the propagation path. [2][22][33].

The parametric model based on wave propagation theory is discussed in [32]. The Expectation Maximization (EM) based algorithm is discussed in [22] where the ultrasonic signals are modeled as Gaussian echoes. The techniques discussed in [29-31] are also extensions of the Gaussian Echo model.

A method for estimating the structural properties such as size, number density and scattering strength of particles is discussed in [34]. The effect of shear waves are used separately to model the backscatter from spherical particles and describe the structure of the medium.

The basic Gaussian Echo model discussed in [22] has been used as the basis for all the modeling work in this dissertation due to ease, simplicity of implementation and parameters known based on a physical pulse-echo inspection setup.

## 3.2 Parametric Model: Clean Signal

The model for ultrasonic reflection is given by

$$S(t) = R_c \beta e^{-\alpha(t-\tau)^2} \cos(2\pi f_c (t-\tau) + \phi) \quad \text{.....(1)}$$

$$\theta = [\alpha \;\; \tau \;\; f_c \;\; \phi \;\; \beta]$$

This model is called the Gaussian model and the signal parameters of the echo are as follows: α is the bandwidth factor; τ is the arrival time, $f_c$ is the center frequency of reflected signal, ϕ is the angle of the reflected signal, β is the intensity reflection coefficient and $R_c$ is the pressure reflection coefficient. In the setup used to inspect the samples, the angle of the reflected signal ϕ = 0.

If $x(t) = e^{-\propto t^2}$ , the transmitted signal can be written as

$$S(t) = x(t)\cos(2\pi f_c t) \quad \text{.....(2)}$$

In the frequency domain

$$\Im\{S(t)\} = \Im\{x(t)\cos(2\pi f_c)\} \quad \text{.....(3)}$$

$$\Im\{S(t)\} = \frac{1}{2}[X(\omega + 2\pi f_c) + X(\omega - 2\pi f_c)] \quad \text{.....(4)}$$

$$\Im\{x(t)\} == \frac{1}{\sqrt{2\alpha}}\left[ e^{\frac{-\omega^2}{4\alpha}} \right] \quad \text{.....(5)}$$

$$\Im\{S(t)\} = \frac{1}{2}\left[ e^{\frac{-(\omega+2\pi f_c)^2}{4\alpha}} + e^{\frac{-(\omega-2\pi f_c)^2}{4\alpha}} \right] \quad \text{.....(6)}$$

Similarly for

$$S(t-\tau) = e^{-\alpha(t-\tau)^2}\cos(2\pi f_c(t-\tau)) \quad \text{.....(7)}$$

the Fourier Transform is

$$\Im\{S(t-\tau)\} = \Im\{S(t)\}e^{-j\omega\tau} \quad \text{.....(8)}$$

Therefore,

$$\Im\{\sum_{i=1}^{n} R_i\beta_i S(t-\tau_i)\} = \Im\{S(t)\}\sum_{i=1}^{n} R_i\beta_i e^{-j\omega\tau_i} \quad \text{.....(9)}$$

The focus of this research is only on one layer of material as shown in Figure 11. Therefore, the parametric model is focused on $S_{FS}$ which is the front surface reflection and $S_{BW}$ which is the backwall reflection.

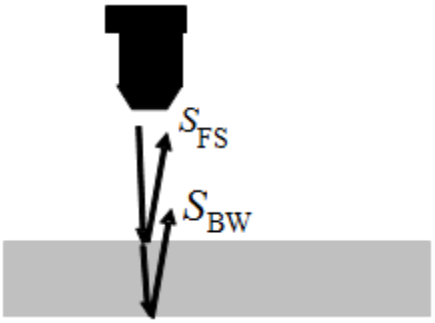


**Figure 11:Illustration for interfaces related to $S_{FS}$ and $S_{BW}$**

The angle of the reflected signal $\phi = 0$ in this research work as that is the typical setup for inspecting the samples of interest. The pulse echo reflection from the front surface, $S_{FS}$ is given by

$$S_{FS}(t) = R_{FS}\beta_{FS}\, e^{-\alpha(t-\tau_{FS})^2} \cos(2\pi f_c(t-\tau_{FS}))\text{.....(10)}$$

where

$$\beta_{FS} = \frac{(z_1 - z_2)^2}{(z_1 + z_2)^2} \text{ and } R_{FS} = \frac{(z_1 - z_2)}{(z_1 + z_2)}$$

in which $z_1$and $z_2$ are the acoustic impedances of water and resin material respectively. The acoustic impedance of water is given by

$$z_1 = \rho_1 * c_1$$

$\rho_1$ is the density of the water and $c_1$ is the longitudinal material velocity of water.

$$z_2 = \rho_2 * c_2$$

$\rho_2$ is the density of the resin and $c_2$ is the longitudinal material velocity of resin. The pulse echo reflection from the backwall, $S_{BW}$ is given by

$$S_{BW}(t) = R_{BW}\beta_{BW}\, e^{-\alpha(t-\tau_{BW})^2}\cos(2\pi f_c(t-\tau_{BW}))\text{.....(11)}$$

$$\beta_{BW} = T_r\frac{(z_2-z_1)^2}{(z_1+z_2)^2} \text{ and } R_{BW} = \frac{(z_2-z_1)}{(z_1+z_2)}$$

$$T_r = 1-\beta_{FS}$$

The resulting ultrasonic reflection from the entire clean sample $S_{CL}(t)$ is modeled as

$$S_{CL}(t) = S_{FS}(t) + S_{BW}(t)\text{.....(12)}$$

$$S_{CL}(t) = R_{FS}\beta_{FS}\, e^{-\alpha(t-\tau_{FS})^2}\cos(2\pi f_c(t-\tau_{FS})) + R_{BW}\beta_{BW}\, e^{-\alpha(t-\tau_{BW})^2}\cos(2\pi f_c(t-\tau_{BW}))\text{....(13)}$$

$$\Im\{S_{CL}(t)\} = R_{FS}\beta_{FS}\,\Im\{e^{-\alpha(t-\tau_{FS})^2}\cos(2\pi f_c(t-\tau_{FS}))\} + R_{BW}\beta_{BW}\,\Im\{e^{-\alpha(t-\tau_{BW})^2}\cos(2\pi f_c(t-\tau_{BW}))\}\text{.....(14)}$$

$$\Im\{S_{CL}(t)\} = R_{FS}\beta_{FS}\, e^{-j\omega\tau_{FS}}\Im\{S(t)\} + R_{BW}\beta_{BW}e^{-j\omega\tau_{BW}}\Im\{S(t)\}\text{.....(15)}$$

$$\Im\{S_{CL}(t)\} = \Im\{S(t)\}(R_{FS}\beta_{FS}\, e^{-j\omega\tau_{FS}} + R_{BW}\beta_{BW}e^{-j\omega\tau_{BW}})\text{.....(16)}$$

$$\Im\{S_{CL}(t)\} = \frac{1}{2}\left[e^{\frac{-(\omega+2\pi f_c)^2}{4\alpha}} + e^{\frac{-(\omega-2\pi f_c)^2}{4\alpha}}\right] * (R_{FS}\beta_{FS}\, e^{-j\omega\tau_{FS}} + R_{BW}\beta_{BW}e^{-j\omega\tau_{BW}})\text{ .....(17)}$$

### 3.2.1 Clean Signal: Frequency Domain Analysis

In order to understand the difference between the transmitted signal and the reflected signal from the surface and backwall of the sample without any particles as well as its interpretation in the frequency domain, eq.(17) was further analyzed. Let

$$H(s) = (\alpha_1 e^{-s\tau_{FS}} + \alpha_2 e^{-s\tau_{BW}}) \quad \text{.....(18)}$$

where $\alpha_1 = R_{FS}\beta_{FS}$ and $\alpha_2 = R_{BW}\beta_{BW}$

In order to find the zeros of the transform, let $H(s) = (\alpha_1 e^{-s\tau_{FS}} + \alpha_2 e^{-s\tau_{BW}}) = 0$

$$\alpha_1 e^{-s\tau_{FS}} = -\alpha_2 e^{-s\tau_{BW}} \quad \text{.....(19)}$$

$$\frac{e^{-s\tau_{FS}}}{e^{-s\tau_{BW}}} = \frac{-\alpha_2}{\alpha_1} \quad \text{.....(20)}$$

$$e^{-s\tau_{FS}+s\tau_{BW}} = \frac{-\alpha_2}{\alpha_1} \quad \text{.....(21)}$$

$$e^{-s(\tau_{FS}-\tau_{BW})} = \frac{-\alpha_2}{\alpha_1} \quad \text{.....(22)}$$

Let $s = \sigma + j\omega$ and $T = \tau_{BW} - \tau_{FS}$

$$e^{(\sigma+j\omega)T} = \frac{-\alpha_2}{\alpha_1} \quad \text{.....(23)}$$

$$e^{\sigma T + j\omega T} = -\frac{\alpha_2}{\alpha_1} \quad \text{.....(24)}$$

The magnitude of eq. (24) is

$$|e^{\sigma T} e^{j\omega T}| = |-\frac{\alpha_2}{\alpha_1}| \quad \text{.....(25)}$$

The magnitude of $e^{j\omega T} = 1$, therefore, $|e^{\sigma T}| = |-\frac{\alpha_2}{\alpha_1}|$. Taking natural log on both sides, we get

$$\sigma T = \ln|-\frac{\alpha_2}{\alpha_1}| \quad \text{.....(26)}$$

$$\sigma = \frac{1}{T}\ln|-\frac{\alpha_2}{\alpha_1}| \quad \text{.....(27)}$$

The angle of ( $e^{\sigma T}e^{j\omega T}$ ) is

$$\angle e^{\sigma T}e^{j\omega T} = \angle -\frac{\alpha_2}{\alpha_1} \quad \text{.....(28)}$$

$$\angle e^{j\omega T} = \angle -\frac{\alpha_2}{\alpha_1} \quad \text{.....(29)}$$

$$\omega T = \angle -\frac{\alpha_2}{\alpha_1} \quad \text{.....(30)}$$

If $-\frac{\alpha_2}{\alpha_1}$ is positive and real,

$$\angle\frac{\alpha_2}{\alpha_1} = \pm 0, \pm 2\pi, \pm 4\pi, \pm 6\pi, \ldots \quad \text{.....(31).}$$

$$\omega T = \pm 0, \pm 2\pi, \pm 4\pi, \pm 6\pi, \ldots \quad \text{.....(32)}$$

$$\omega = \pm 0, \pm\frac{2\pi}{T}, \pm\frac{4\pi}{T}, \pm\frac{6\pi}{T}, \ldots \quad \text{.....(33)}$$

$$F = \pm 0, \pm\frac{1}{T}, \pm\frac{2}{T}, \pm\frac{3}{T}, \ldots \quad \text{.....(34)}$$

If $-\frac{\alpha_2}{\alpha_1}$ is negative and real, then

$$\angle\frac{\alpha_2}{\alpha_1} = \pm\pi, \pi \pm 2\pi, \pi \pm 4\pi, \pi \pm 6\pi \ldots \quad \text{.....(35)}$$

$$\omega T = \pm\pi, \pi \pm 2\pi, \pi \pm 4\pi, \pi \pm 6\pi, .... \quad \text{.....(36)}$$

$$\omega = \pm\frac{\pi}{T}, \frac{\pi \pm 2\pi}{T}, \frac{\pi \pm 4\pi}{T}, \frac{\pi \pm 6\pi}{T}, .. \quad \text{.....(37)}$$

$$F = \pm\frac{1}{2T}, \pm\frac{3}{2T}, \pm\frac{5}{2T}, \pm\frac{7}{2T}, .. \quad \text{.....(38)}$$

Using the parameters $\rho_1 = 1, c_1 = 1.483, \rho_2 = 3.721, c_2 = 1.18,\ \alpha_1 = -0.1213$, $\alpha_2 = 0.0916$, we get $\frac{\alpha_2}{\alpha_1} = -0.7549$. Since $-\frac{\alpha_2}{\alpha_1}$ is positive for this case, $F = \pm 0, \pm\frac{1}{T}, \pm\frac{2}{T}, \pm\frac{3}{T}, ...$ . For a material thickness of 850um, $\tau_{FS} = 14.567us$ and $\tau_{BW} = 15.0239us$. Therefore, T= 0.4569us and $\sigma = 0.6153$. Eq (17) has been graphed in two parts as $\Im\{S(t)\}$ and $R_{FS}\beta_{FS}\, e^{-j\omega\tau_{FS}} + R_{BW}\beta_{BW} e^{-j\omega\tau_{BW}}$ shown in Figure 12 and Figure 13 respectively. The notches are expected at frequencies in MHz at 0, 2.188, 4.376, 6.564... and have been observed in Figure 13. $\Im\{S_{CL}(t)\}$, given by eq. (17) has been graphed and shown in Figure 14. The Power Spectral Density has been computed as shown in Figure 15 and the maximum power was noted as $9.36x10^{-5}$.

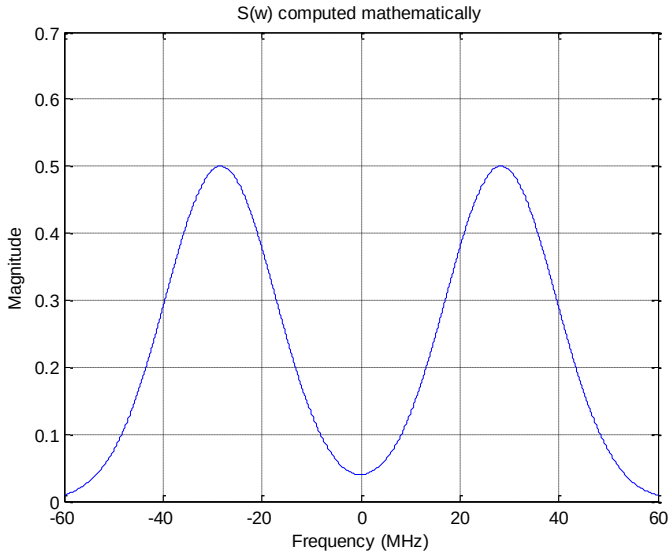


**Figure 12: Mathematically computed FFT of the transmitted signal S(t)**

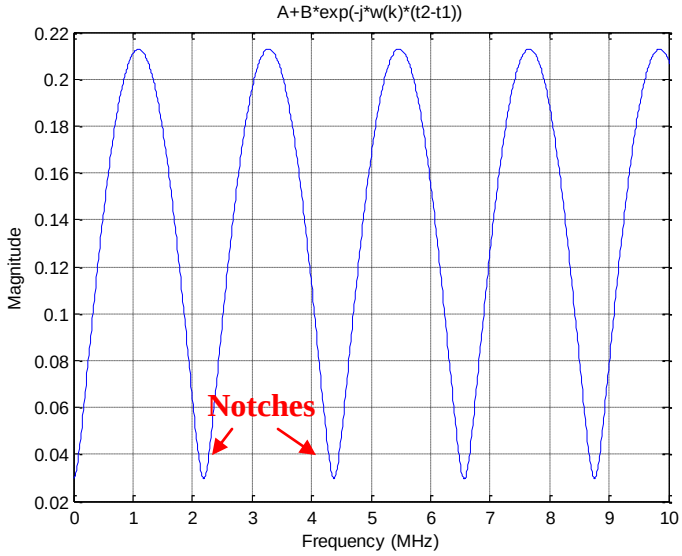


**Figure 13: Mathematically computed FFT of the Surface and Backwall Reflections**

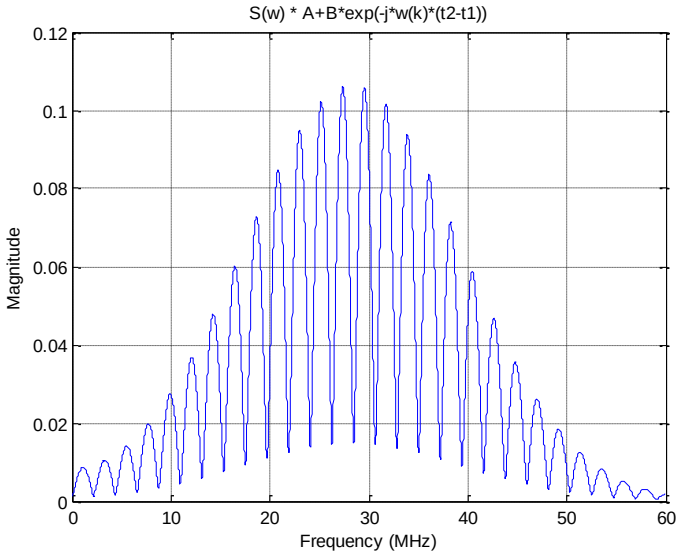


**Figure 14: Mathematically computed FFT all reflections from clean sample case**

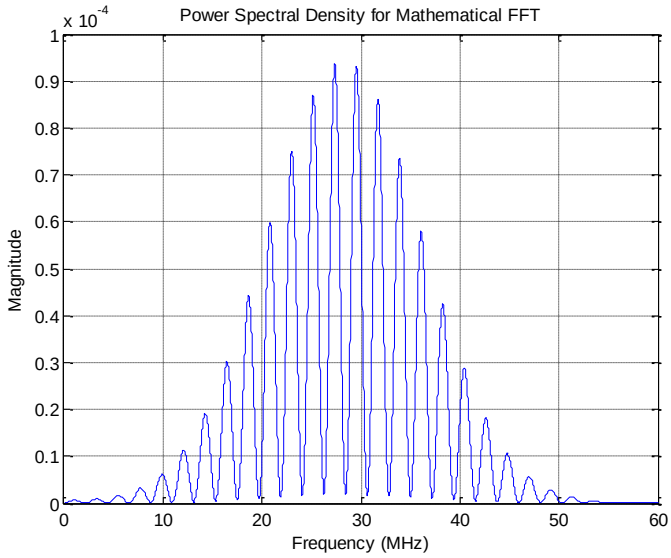


**Figure 15: Power Spectral Density for the entire signal from clean sample case**

## 3.3 Ultrasonic Reflections with Filler Particles: Corrupted Signal

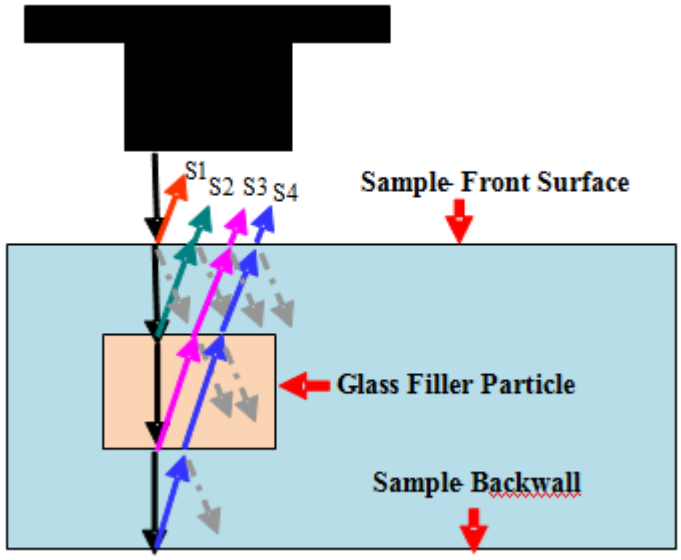


**Figure 16: Illustration of interfaces related to sample with one particle**

The ultrasonic reflection from a sample with one filler particle is illustrated in Figure 16. The resulting set of reflections from the sample in the presence of one particle is given by

$$S_{CO}(t) = S_{FS}(t) + S_{T1}(t) + S_{B1}(t) + S_{BWc}(t) \quad \text{.....(39)}$$

$S_{FS}(t) = S_1$ as illustrated in Figure 16 and is given by eq. (10) .

$S_{T1}(t) = S_2$, $S_{B1}(t) = S_3$ and $S_{BWc}(t) = S_4(t)$ and are also as illustrated in Figure 16.

The reflection from top of the particle $S_{T1}(t)$ which is at the resin to the glass interface is given by

$$S_{T1}(t) = R_{T1}\beta_{T1}\, e^{-\alpha(t-\tau_{T1})^2}\cos(2\pi f_c(t-\tau_{T1}))\text{.....(40)}$$

$$\beta_{T1} = T_{T1}\frac{(z_2 - z_3)^2}{(z_2 + z_3)^2} \text{ and } R_{T1} = \frac{(z_2 - z_3)}{(z_2 + z_3)}$$

$$T_{T1} = 1 - \beta_{FS}$$

$z_2$ and $z_3$ are the acoustic impedances of resin and glass material respectively and $c_3$ is the longitudinal material velocity of glass. The acoustic impedance of a material is given by

$$z_3 = \rho_3 * c_3$$

The reflection from the bottom of the particle $S_{B1}(t)$ which is at the glass to the resin interface is given by

$$S_{B1}(t) = R_{B1}\beta_{B1}\, e^{-\alpha(t-\tau_{B1})^2}\cos(2\pi f_c(t-\tau_{B1}))\text{.....(41)}$$

$$\beta_{B1} = T_{B1}\frac{(z_3 - z_2)^2}{(z_2 + z_3)^2} \text{ and } R_{B1} = \frac{(z_3 - z_2)}{(z_2 + z_3)}$$

$$T_{B1} = 1 - \beta_{T1}$$

The backwall reflection for the case where there is a one particle is given by

$$S_{BWc}(t) = R_{BWc}\beta_{BWc}\, e^{-\alpha(t-\tau_{BWc})^2}\cos(2\pi f_c(t-\tau_{BWc}))\text{.....(42)}$$

$$\beta_{BWc} = T_{BWc}\frac{(z_2 - z_1)^2}{(z_1 + z_2)^2} \text{ and } R_{BWc} = \frac{(z_2 - z_1)}{(z_2 + z_1)}$$

$$T_{BWc} = 1 - \beta_{B1}$$

$$S_{CO}(t) = R_{FS}\beta_{FS}\, e^{-\alpha(t-\tau_{FS})^2}\cos(2\pi f_c(t-\tau_{FS})) +$$
$$R_{T1}\beta_{T1}\, e^{-\alpha(t-\tau_{T1})^2}\cos(2\pi f_c(t-\tau_{T1})) + R_{B1}\beta_{B1}\, e^{-\alpha(t-\tau_{B1})^2}\cos(2\pi f_c(t-\tau_{B1})) +$$
$$R_{BWc}\beta_{BWc}\, e^{-\alpha(t-\tau_{BWc})^2}\cos(2\pi f_c(t-\tau_{BWc})) \quad \text{.....(43)}$$

This equation can be extended to "n" particle scenario in the path of the ultrasound.

$$S_{CO}(t) = S_{FS}(t) + S_{BWc}(t) + \sum_{i=1}^{n} R_{Ti}\beta_{Ti}\, e^{-\alpha(t-\tau_{Ti})^2}\cos(2\pi f_c(t-\tau_{Ti})) +$$
$$\sum_{i=1}^{n} R_{Bi}\beta_{Bi}\, e^{-\alpha(t-\tau_{Bi})^2}\cos(2\pi f_c(t-\tau_{Bi})) \quad \text{.....(44)}$$

Taking the Fourier Transform of $S_{co}(t)$

$$\Im\{S_{CO}(t)\} = \Im\{S_{FS}(t)\} + \Im\{S_{BWc}(t)\} + \sum_{i=1}^{n} R_{Ti}\beta_{Ti}\,\Im\{e^{-\alpha(t-\tau_{Ti})^2}\cos(2\pi f_c(t-\tau_{Ti}))\} +$$
$$\sum_{i=1}^{n} R_{Bi}\beta_{Bi}\,\Im\{e^{-\alpha(t-\tau_{Bi})^2}\cos(2\pi f_c(t-\tau_{Bi}))\} \quad \text{.....(45)}$$

$$\Im\{S_{CO}(t)\} = \Im\{S(t)\}R_{FS}\beta_{FS}e^{-j\omega\tau_{FS}} + \Im\{S(t)\}R_{BWc}\beta_{BWc}e^{-j\omega\tau_{BWc}} + \Im\{S(t)\}\sum_{i=1}^{n} R_{Ti}\beta_{Ti}\, e^{-j\omega\tau_{Ti}} +$$
$$\Im\{S(t)\}\sum_{i=1}^{n} R_{Bi}\beta_{Bi}\, e^{-j\omega\tau_{Bi}} \quad \text{.....(46)}$$

### 3.3.1 Corrupted Signal: Frequency Domain Analysis

To understand the effect of particles' size and position in depth of the sample at a specific (x,y) location, one particle case is considered. Therefore, the values of $n$ are set to "1". The reflected signal from all the interfaces is given by

$$\Im\{S_{CO}(t)\} = \Im\{S(t)\}[R_{FS}\beta_{FS}e^{-j\omega\tau_{FS}} + R_{BWc}\beta_{BWc}e^{-j\omega\tau_{BWc}} + R_{T1}\beta_{T1}\, e^{-j\omega\tau_{T1}} + R_{B1}\beta_{B1}\, e^{-j\omega\tau_{B1}}]$$
$$\text{.....(47)}$$

In order to understand the difference between the reflections from a clean resin case and resin sample with filler particles as well as its interpretation in the frequency domain, eq. (47) was further analyzed similar to the one discussed in section 3.2.1. Let

$$H_1(s) = \alpha_1 e^{-s\tau_{FS}} + \alpha_3 e^{-s\tau_{BWc}} \quad \text{.....(48)}$$

where $\alpha_1 = R_{FS}\beta_{FS}$ , $\alpha_3 = R_{BWc}\beta_{BWc}$

$$\alpha_1 e^{-s\tau_{Fs}} = -\alpha_3 e^{-s\tau_{BWc}} \quad \text{.....(49)}$$

$$\frac{e^{-s\tau_{Fs}}}{e^{-s\tau_{BWc}}} = -\frac{\alpha_3}{\alpha_1} \quad \text{.....(50)}$$

$$e^{-s\tau_{Fs}+s\tau_{BWc}} = \frac{-\alpha_3}{\alpha_1} \quad \text{.....(51)}$$

$$e^{-s(\tau_{Fs}-\tau_{BWc})} = \frac{-\alpha_3}{\alpha_1} \quad \text{.....(52)}$$

Let $s = \sigma + j\omega$ and $T = \tau_{BWc} - \tau_{Fs}$

$$e^{(\sigma+j\omega)T} = \frac{-\alpha_3}{\alpha_1} \quad \text{.....(53)}$$

$$e^{\sigma T + j\omega T} = -\frac{\alpha_3}{\alpha_1} \quad \text{.....(54)}$$

The magnitude of eq. (54) is

$$|e^{\sigma T} e^{j\omega T}| = |-\frac{\alpha_3}{\alpha_1}| \quad \text{.....(55)}$$

The magnitude of $e^{j\omega T}$ =1, therefore, $|e^{\sigma T}| = |-\frac{\alpha_3}{\alpha_2}|$. Taking natural log on both sides, we get

$$\sigma T = \ln|-\frac{\alpha_3}{\alpha_1}| \quad \text{.....(56)}$$

$$\sigma = \frac{1}{T}\ln|-\frac{\alpha_3}{\alpha_1}| \quad \text{.....(57)}$$

The angle of ( $e^{\sigma T}e^{j\omega T}$ ) is

$$\angle e^{\sigma T}e^{j\omega T} = \angle -\frac{\alpha_3}{\alpha_1} \quad \text{.....(58)}$$

$$\angle e^{j\omega T} = \angle -\frac{\alpha_3}{\alpha_1} \quad \text{.....(59)}$$

$$\omega T = \angle -\frac{\alpha_3}{\alpha_1} \quad \text{.....(60)}$$

If $-\frac{\alpha_3}{\alpha_1}$ is positive and real, then

$$\angle -\frac{\alpha_3}{\alpha_1} = \pm 0, \pm 2\pi, \pm 4\pi, \pm 6\pi, \ldots \quad \text{.....(61)}$$

$$\omega T = \pm 0, \pm 2\pi, \pm 4\pi, \pm 6\pi, \ldots \quad \text{.....(62)}$$

$$\omega = \pm 0, \pm \frac{2\pi}{T}, \pm \frac{4\pi}{T}, \pm \frac{6\pi}{T}, \ldots \quad \text{.....(63)}$$

$$F = \pm 0, \pm \frac{1}{T}, \pm \frac{2}{T}, \pm \frac{3}{T}, \ldots \quad \text{.....(64)}$$

If $-\frac{\alpha_3}{\alpha_1}$ is negative and real, then

$$\angle -\frac{\alpha_3}{\alpha_1} = \pm \pi, \pi \pm 2\pi, \pi \pm 4\pi, \pi \pm 6\pi \ldots \quad \text{.....(65)}$$

$$\omega T = \pm \pi, \pi \pm 2\pi, \pi \pm 4\pi, \pi \pm 6\pi, \ldots \quad \text{.....(66)}$$

$$\omega = \pm\frac{\pi}{T}, \frac{\pi \pm 2\pi}{T}, \frac{\pi \pm 4\pi}{T}, \frac{\pi \pm 6\pi}{T}, . \quad \text{.....(67)}$$

$$F = \pm\frac{1}{2T}, \pm\frac{3}{2T}, \pm\frac{5}{2T}, \pm\frac{7}{2T}, . \quad \text{.....(68)}$$

Using the parameters $\rho_1 = 1, c_1 = 1.483, \rho_2 = 3.721, c_2 = 1.18, \rho_3 = 5.77, c_3 = 2.6$ we get

$\alpha_1 = -0.1213, \alpha_3 = 0.0932$. Therefore, $\frac{\alpha_3}{\alpha_1} = -0.6441$. Also, $\tau_{T1} = 14.7014us$ and

$\tau_{BWc} = 14.9761us$, T=0.4091us. Therefore, $\sigma = 0.6441$. Since $-\frac{\alpha_3}{\alpha_1}$ is positive,

$F = \pm 0, \pm\frac{1}{T}, \pm\frac{2}{T}, \pm\frac{3}{T}, ...$

Let

$$H_2(s) = \beta_1 e^{-s\tau_{T1}} + \beta_2 e^{-s\tau_{B1}} \quad \text{.....(69)}$$

where $R_{T1}\beta_{T1} = \beta_1$ and $R_{B1}\beta_{B1} = \beta_2$

$$H_2(s) = \beta_1 e^{-s\tau_{T1}} + \beta_2 e^{-s\tau_{B1}} = 0 \quad \text{.....(70)}$$

$$\beta_1 e^{-s\tau_{T1}} = -\beta_2 e^{-s\tau_{B1}} \quad \text{.....(71)}$$

$$\frac{e^{-s\tau_{T1}}}{e^{-s\tau_{B1}}} = -\frac{\beta_2}{\beta_1} \quad \text{.....(72)}$$

$$e^{-s\tau_{T1}+s\tau_{B1}} = \frac{-\beta_2}{\beta_1} \quad \text{.....(73)}$$

$$e^{-s(\tau_{T1}-\tau_{B1})} = \frac{-\beta_2}{\beta_1} \quad \text{.....(74)}$$

Let $s = \sigma + j\omega$ and $T = \tau_{B1} - \tau_{T1}$

$$e^{(\sigma+j\omega)T} = \frac{-\beta_2}{\beta_1} \quad \text{.....(75)}$$

$$e^{\sigma T+j\omega T} = -\frac{\beta_2}{\beta_1} \quad \text{.....(76)}$$

The magnitude of eq. (76) is

$$|e^{\sigma T}e^{j\omega T}| = |-\frac{\beta_2}{\beta_1}| \quad \text{.....(77)}$$

The magnitude of $e^{j\omega T}$ =1, therefore, $|e^{\sigma T}| = |-\frac{\beta_2}{\beta_1}|$. Taking natural log on both sides, we get

$$\sigma T = \ln|-\frac{\beta_2}{\beta_1}| \quad \text{.....(78)}$$

$$\sigma = \frac{1}{T}\ln|-\frac{\beta_2}{\beta_1}| \quad \text{.....(79)}$$

The angle of ($e^{\sigma T}e^{j\omega T}$) is

$$\angle e^{\sigma T}e^{j\omega T} = \angle -\frac{\beta_2}{\beta_1} \quad \text{.....(80)}$$

$$\angle e^{j\omega T} = \angle -\frac{\beta_2}{\beta_1} \quad \text{.....(81)}$$

$$\omega T = \angle -\frac{\beta_2}{\beta_1} \quad \text{.....(82)}$$

If $-\frac{\beta_2}{\beta_1}$ is positive and real, then

$$\angle -\frac{\beta_2}{\beta_1} = \pm 0, \pm 2\pi, \pm 4\pi, \pm 6\pi, \ldots \quad \text{.....(83)}$$

$$\omega T = \pm 0, \pm 2\pi, \pm 4\pi, \pm 6\pi, \ldots \quad \text{.....(84)}$$

$$\omega = \pm 0, \pm \frac{2\pi}{T}, \pm \frac{4\pi}{T}, \pm \frac{6\pi}{T}, \ldots \quad \text{.....(85)}$$

$$F = \pm 0, \pm \frac{1}{T}, \pm \frac{2}{T}, \pm \frac{3}{T}, \ldots \quad \text{.....(86)}$$

If $-\frac{\beta_2}{\beta_1}$ is negative and real, then

$$\angle -\frac{\beta_2}{\beta_1} = \pm \pi, \pi \pm 2\pi, \pi \pm 4\pi, \pi \pm 6\pi \ldots \quad \text{.....(87)}$$

$$\omega T = \pm \pi, \pi \pm 2\pi, \pi \pm 4\pi, \pi \pm 6\pi, \ldots \quad \text{.....(88)}$$

$$\omega = \pm \frac{\pi}{T}, \frac{\pi \pm 2\pi}{T}, \frac{\pi \pm 4\pi}{T}, \frac{\pi \pm 6\pi}{T}, \ldots \quad \text{.....(89)}$$

$$F = \pm \frac{1}{2T}, \pm \frac{3}{2T}, \pm \frac{5}{2T}, \pm \frac{7}{2T}, \ldots \quad \text{.....(90)}$$

Using the parameters for $\rho_2 = 3.721, c_2 = 1.18, \rho_3 = 2.6, c_3 = 5.77,$

$\beta_1 = -0.1237, \beta_2 = 0.1268$, we get $\frac{\beta_2}{\beta_1} = -1.0252$. Since $\tau_{T1} = 14.7014us$, and

$\tau_{B1} = 14.7880us$, T=0.0867 and $\sigma = 0.2855$. Also, $-\frac{\beta_2}{\beta_1}$ is positive for this case.

Therefore, $F = \pm 0, \pm \frac{1}{T}, \pm \frac{2}{T}, \pm \frac{3}{T}, \ldots$ .

In order to evaluate and understand the effect of one particle, seven different cases have been studied.

**Case 1:** The time taken for the ultrasound to be reflected from the surface is $\tau_{FS} = 14.567us$, the thickness of the sample is 850um, particle size is 250um and particle depth is 250um from the surface. The time taken for the ultrasound to be reflected from top of the particle is $\tau_{T1} = 14.7014us$, the time taken for the ultrasound to be reflected from the bottom of the particle is $\tau_{B1} = 14.7880us$ and the time taken for the ultrasound to be reflected from the backwall is calculated as $\tau_{BWc} = 14.9761us$. Using these parameters, eq (47) has been graphed in segments. The mathematically computed FFT of the transmitted signal is shown in Figure 17, the FFT of the surface and backwall reflections is shown in Figure 18 with notches occurring at frequencies in MHz at 0, 2.444, 4.888, 7.333, ...., the reflection from the top and bottom of the particle is shown in Figure 19 with notches occurring at frequencies in MHz 0, 11.4, 23.08, 34.62,..., the FFT of the entire reflected signal from the sample is shown in Figure 20 and the Power spectral density for the entire signal is shown in Figure 21 with maximum power of the signal noted as $3.9x10^{-5}$.

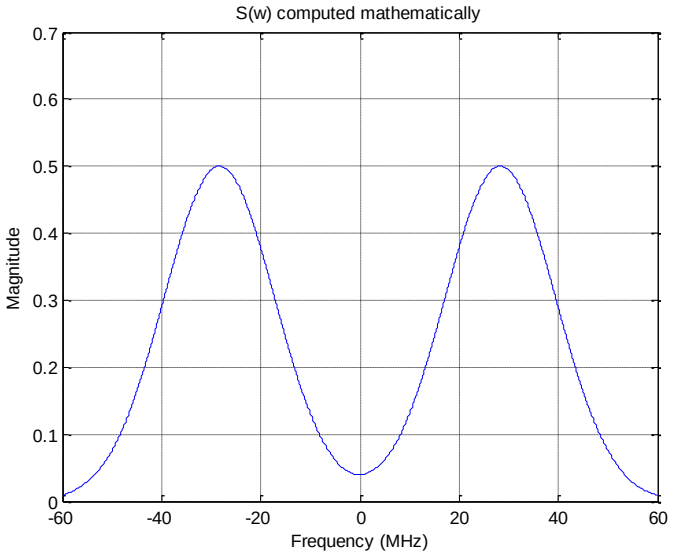


**Figure 17: Mathematically computed FFT of the transmitted signal S(t)**

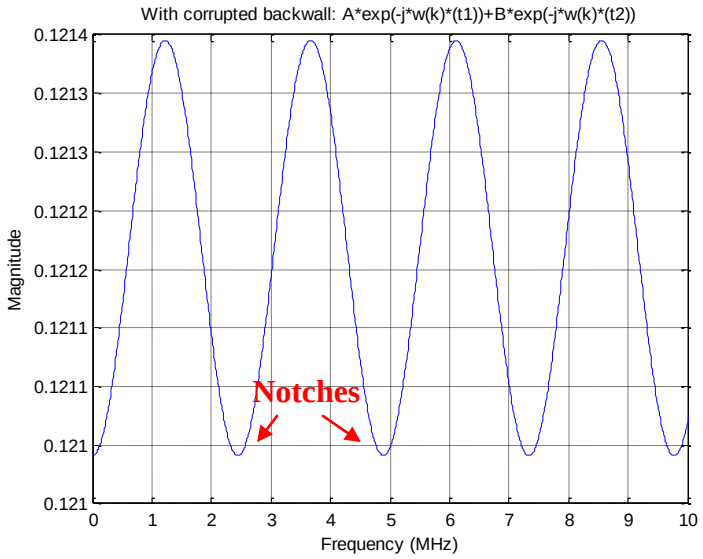


**Figure 18: Mathematically computed FFT of Front and Backwall Reflections for Case 1**

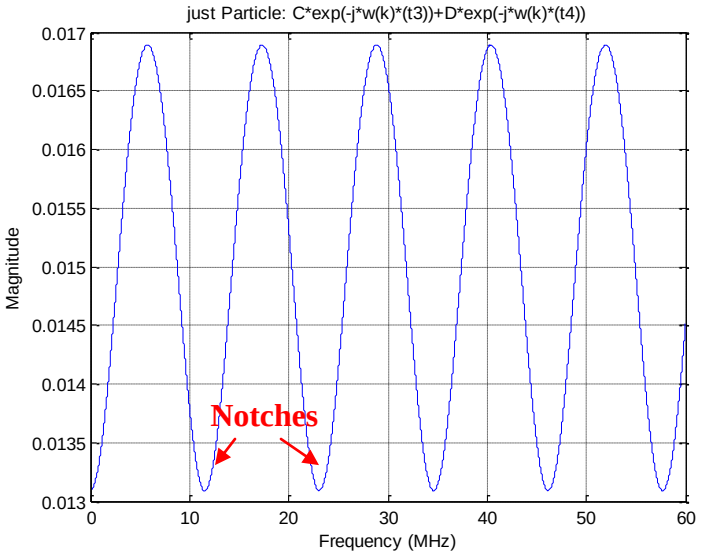


**Figure 19: Mathematically computed FFT of Particle Reflection for Case 1**

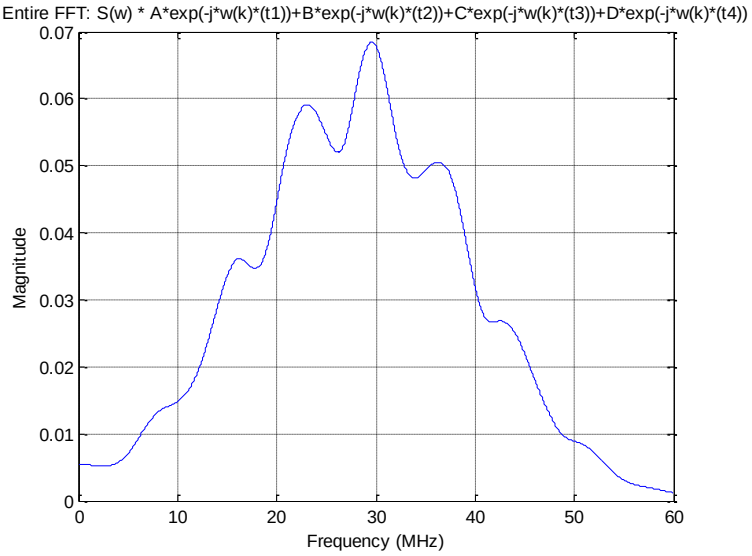


**Figure 20: Mathematically computed FFT of entire reflected signal for Case 1**

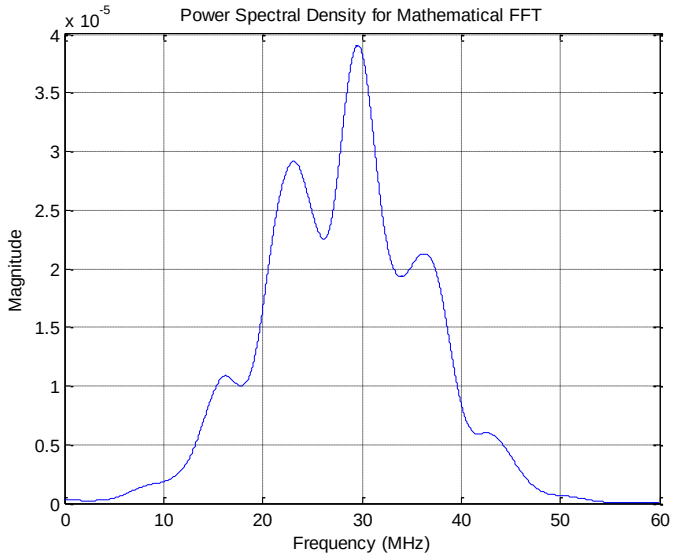


**Figure 21: Power Spectral Density for Case 1**

**Case 2:** The time taken for the ultrasound to be reflected from the surface is $\tau_{FS} = 14.567us$, the thickness of the sample is 850um, particle size is 250um and particle depth is 350um from the surface. The time taken for the ultrasound to be reflected from top of the particle is $\tau_{T1} = 14.7551us$, the time taken for the ultrasound to be reflected from the bottom of the particle is $\tau_{B1} = 14.8418us$ and the time taken for the ultrasound to be reflected from the backwall is calculated as $\tau_{BWc} = 14.9761us$. Using these parameters, eq. (47) has been graphed in segments. The mathematically computed FFT of the transmitted signal is shown in Figure 22, the FFT of the surface and backwall reflections is shown in Figure 23 with notches occurring at frequencies in MHz at 0, 2.444, 4.888, 7.333, ...., the reflection from the top and bottom of the particle is shown in Figure 24 with notches occurring at frequencies in MHz 0, 11.4, 23.08, 34.62,..., the FFT

of the entire reflected signal from the sample is shown in Figure 25 and the Power spectral density for the entire signal is shown in Figure 26 with maximum power of the signal noted as $3.825x10^{-5}$.

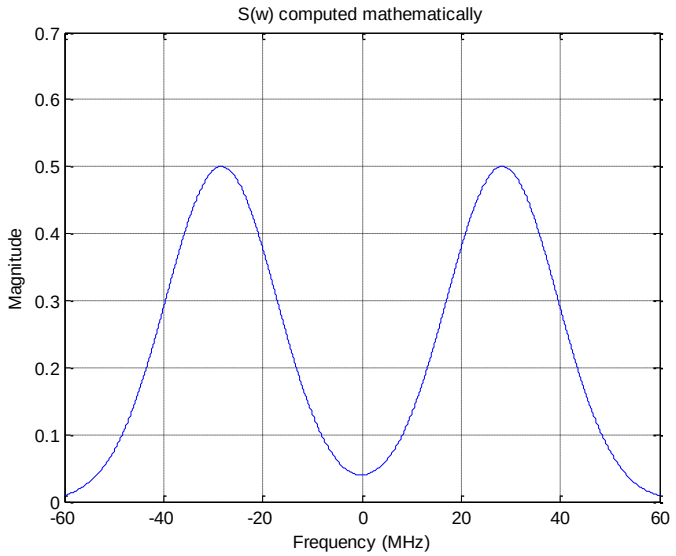


**Figure 22: Mathematically computed FFT of the transmitted signal S(t)**

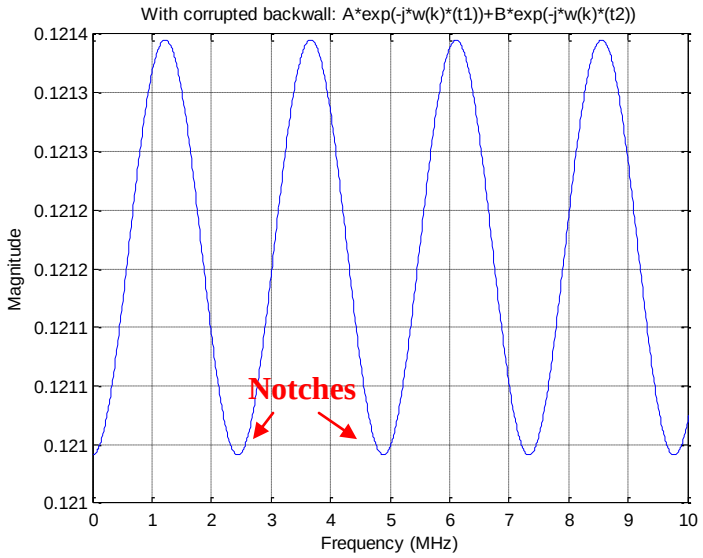


**Figure 23: Mathematically computed FFT from front and backwall reflections for Case 2**

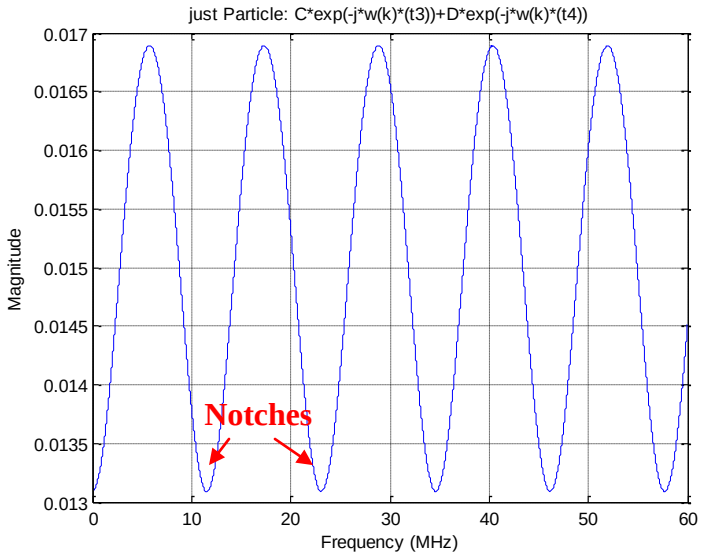


**Figure 24: Mathematically computed FFT for Particle reflection for Case 2**

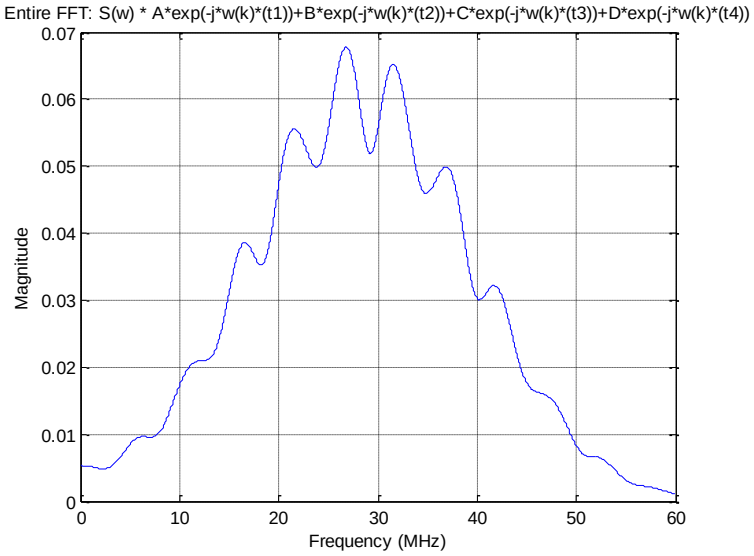


**Figure 25: Mathematically computed FFT for entire reflected signal for Case 2**

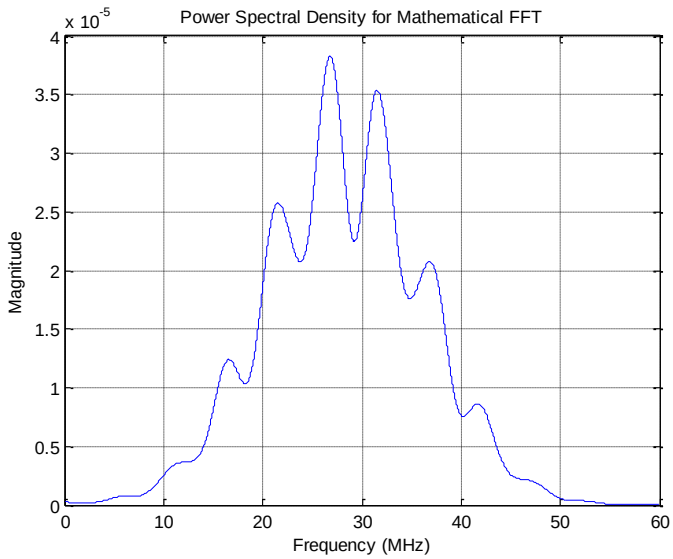


**Figure 26: Power Spectral Density for Case 2**

**Case 3:** The time taken for the ultrasound to be reflected from the surface is $\tau_{FS} = 14.567us$, the thickness of the sample is 850um, particle size is 250um and particle

depth is 500um from the surface. The time taken for the ultrasound to be reflected from top of the particle is $\tau_{T1} = 14.8357us$, the time taken for the ultrasound to be reflected from the bottom of the particle is $\tau_{B1} = 14.9224us$ and the time taken for the ultrasound to be reflected from the backwall is calculated as $\tau_{BWc} = 14.9761us$. Using these parameters, eq (47) has been graphed in segments. The mathematically computed FFT of the transmitted signal is shown in Figure 27, the FFT of the surface and backwall reflections is shown in Figure 28 with notches occurring at frequencies in MHz at 0, 2.444, 4.888, 7.333, ...., the reflection from the top and bottom of the particle is shown in Figure 29 with notches occurring at frequencies in MHz 0, 11.4, 23.08, 34.62,..., the FFT of the entire reflected signal from the sample is shown in Figure 30 and the Power spectral density for the entire signal is shown in Figure 31 with maximum power of the signal noted as $3.89x10^{-5}$.

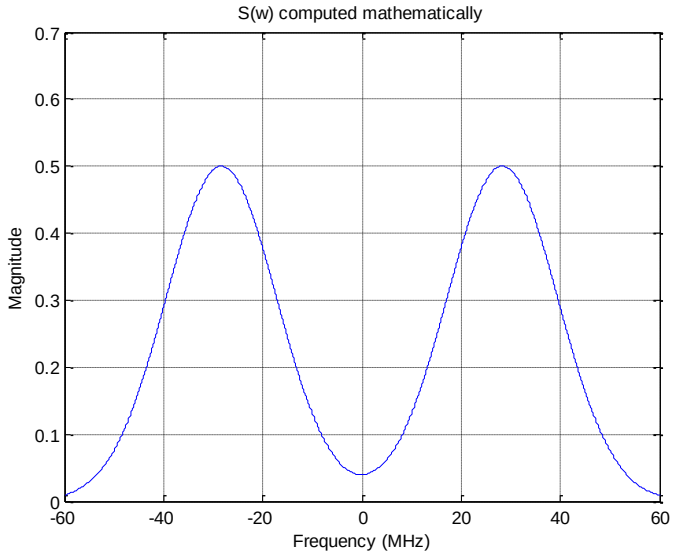


**Figure 27: Mathematically computed FFT of the transmitted signal S(t)**

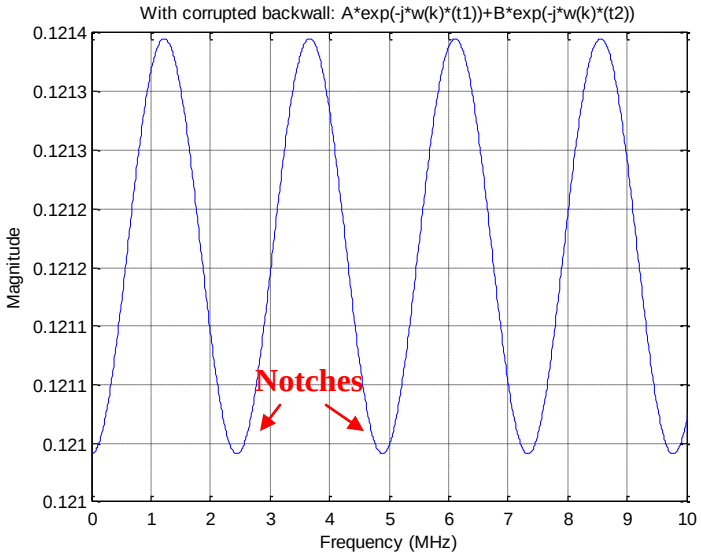


**Figure 28: Mathematically computed FFT for front and backwall reflections for Case 3**

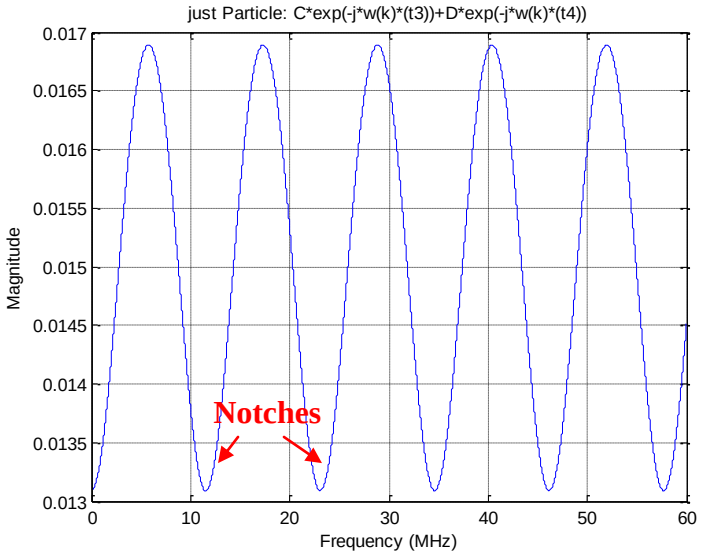


**Figure 29: Mathematically computed FFT for Particle reflection for Case 3**

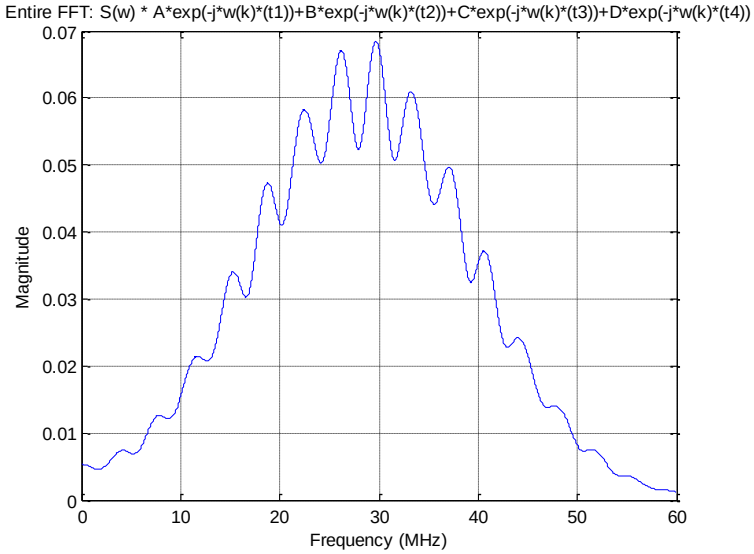


**Figure 30: Mathematically computed FFT for entire reflected signal for Case 3**

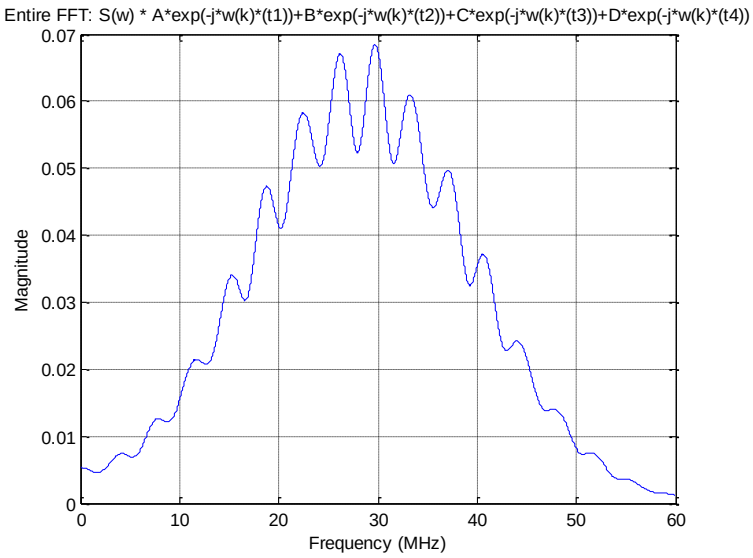


**Figure 31: Power Spectral Density for Case 3**

**Case 4:** The time taken for the ultrasound to be reflected from the surface is $\tau_{FS} = 14.567us$, the thickness of the sample is 850um, particle size is 50um and particle depth is 250um from the surface. The time taken for the ultrasound to be reflected from top of the particle is $\tau_{T1} = 14.7014us$, the time taken for the ultrasound to be reflected from the bottom of the particle is $\tau_{B1} = 14.7187us$ and the time taken for the ultrasound to be reflected from the backwall is calculated as $\tau_{BWc} = 15.0143us$. Using these parameters, eq. (47) has been graphed in segments. The mathematically computed FFT of the transmitted signal is shown in Figure 31, the FFT of the surface and backwall reflections is shown in Figure 32 with notches occurring at frequencies in MHz at 0, 2.23, 4.47, 6.706 ...., the reflection from the top and bottom of the particle is shown in Figure 33 with notches occurring at frequencies in MHz 0, 57.8, 115.6, 173.4,..., the FFT of the

entire reflected signal from the sample is shown in Figure 34 and the Power spectral density for the entire signal is shown in Figure 35 with maximum power of the signal noted as $3.915x10^{-5}$.

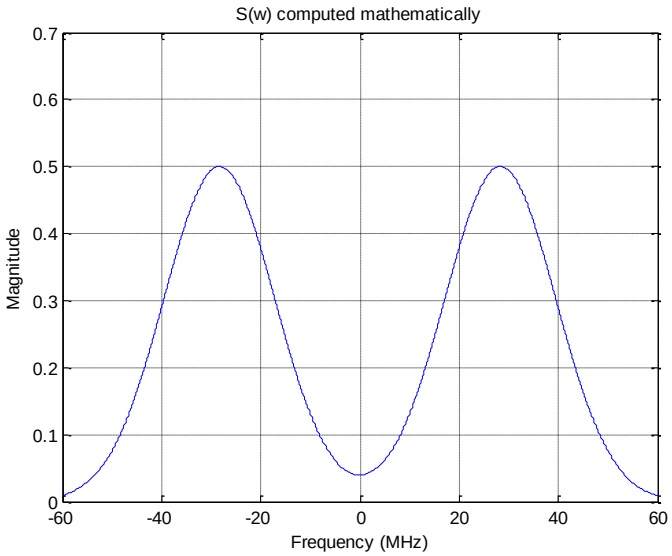


**Figure 32: Mathematically computed FFT of the transmitted signal S(t)**

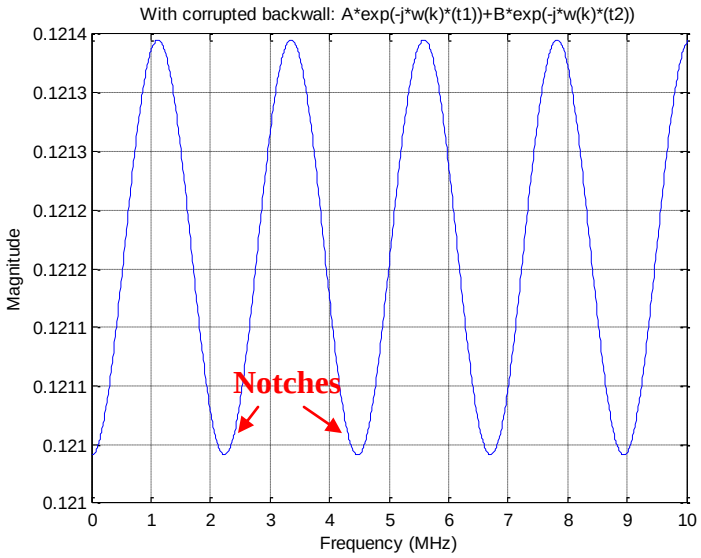


**Figure 33: Mathematically computed FFT for front and backwall reflections for Case 4**

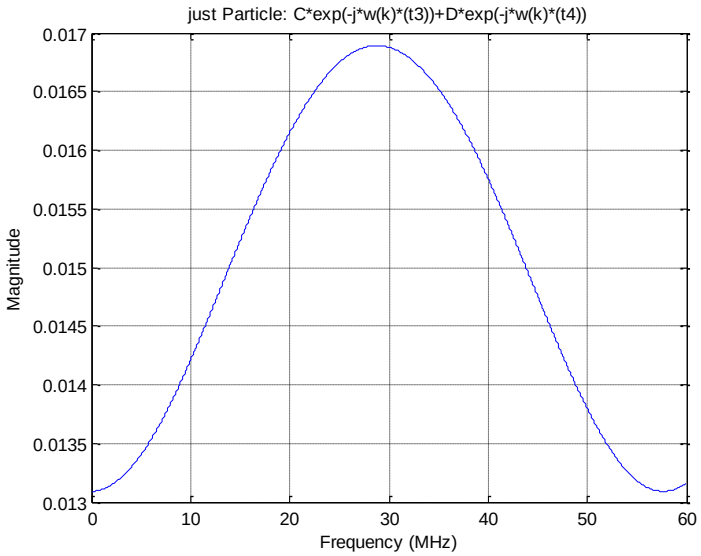


**Figure 34: Mathematically computed FFT for Particle reflection for Case 4**

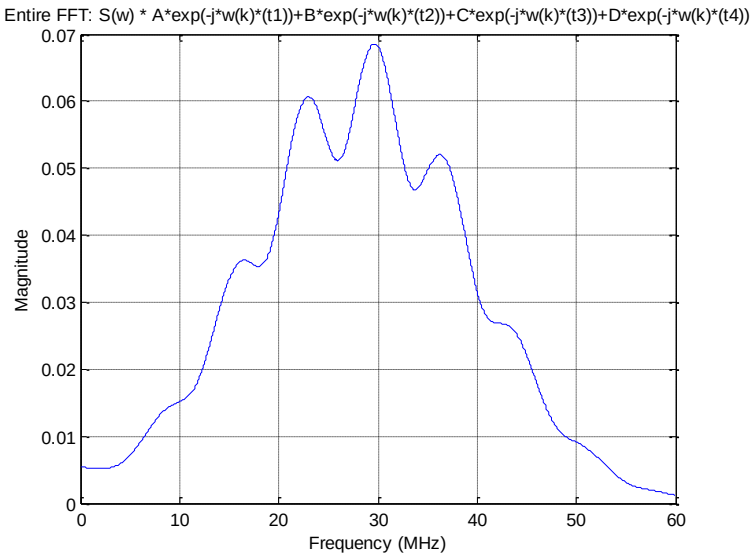


**Figure 35: Mathematically computed FFT for entire signal for Case 4**

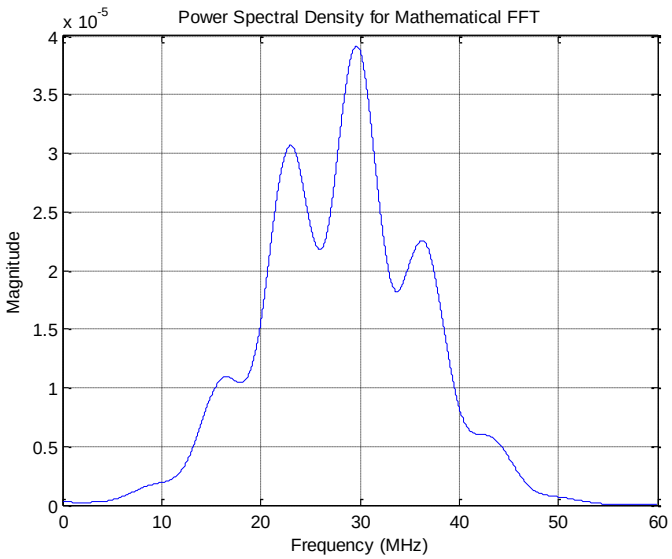


**Figure 36: Power Spectral Density for Case 4**

**Case 5:** The time taken for the ultrasound to be reflected from the surface is $\tau_{FS} = 14.567us$, the thickness of the sample is 850um, particle size is 150um and particle depth is 250um from the surface. The time taken for the ultrasound to be reflected from top of the particle is $\tau_{T1} = 14.7014us$, the time taken for the ultrasound to be reflected from the bottom of the particle is $\tau_{B1} = 14.7534us$ and the time taken for the ultrasound to be reflected from the backwall is calculated as $\tau_{BWc} = 14.9952us$. Using these parameters, eq (47) has been graphed in segments. The mathematically computed FFT of the transmitted signal is shown in Figure 36, the FFT of the surface and backwall reflections is shown in Figure 37 with notches occurring at frequencies in MHz at 0, 2.33, 4.67, 7.006, ...., the reflection from the top and bottom of the particle is shown in Figure 38 with notches occurring at frequencies in MHz 0, 19.23, 38.46, 57.69..., the FFT of the entire reflected signal from the sample is shown in Figure 39 and the Power spectral density for the entire signal is shown in Figure 40 with maximum power of the signal noted as $3.91x10^{-5}$.

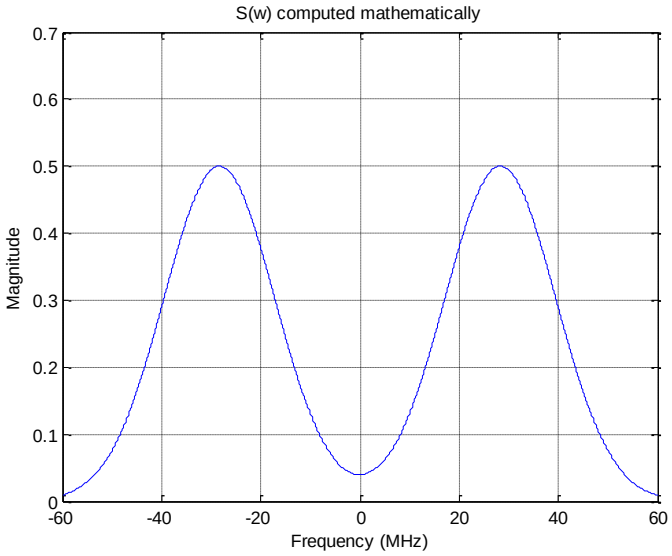


**Figure 37: Mathematically computed FFT of the transmitted signal S(t)**

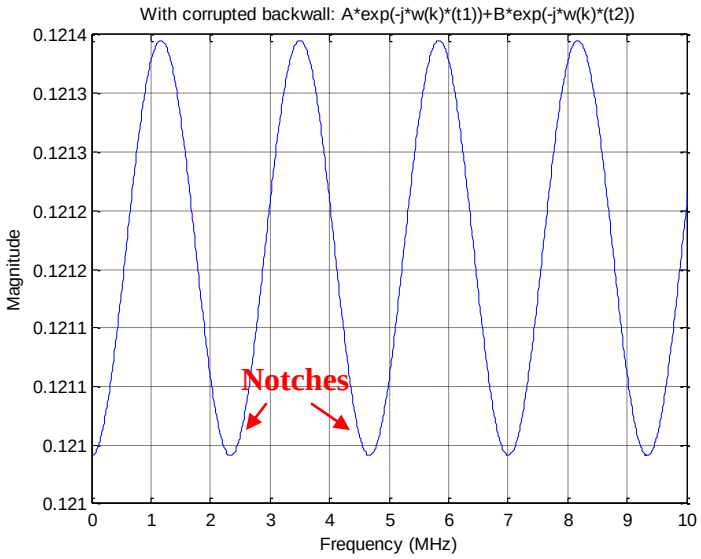


**Figure 38: Mathematically computed FFT for front and backwall reflections for Case 5**

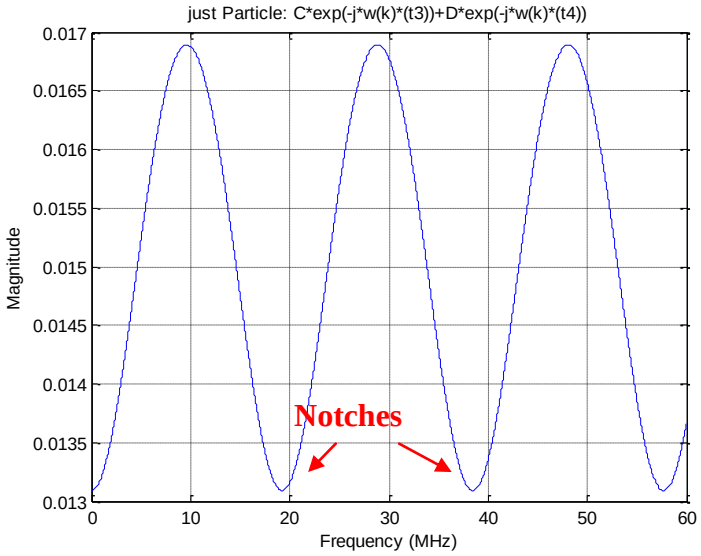


**Figure 39: Mathematically computed FFT for Particle reflection for Case 5**

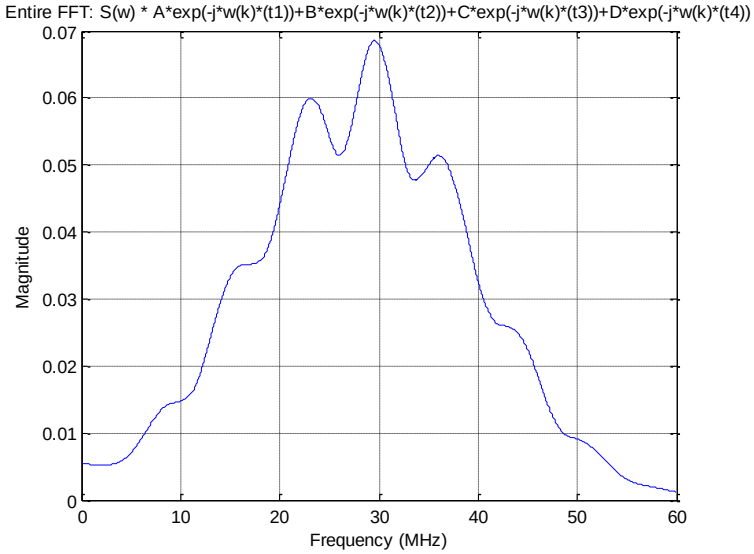


**Figure 40: Mathematically computed FFT for entire signal for Case 5**

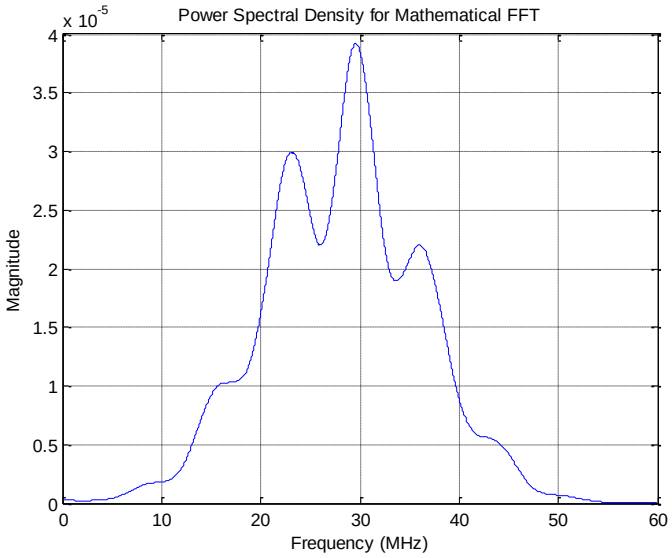


**Figure 41: Power Spectral Density for Case 5**

**Case 6:** The time taken for the ultrasound to be reflected from the surface is $\tau_{FS} = 14.567us$, the thickness of the sample is 850um, size of the first particle is 250um and at a depth is 250um from the surface, size of the second particle is 50um and at a depth of 100um from the bottom of the first particle. The time taken for the ultrasound to be reflected from top of the first particle is $\tau_{T1} = 14.7014us$, the time taken for the ultrasound to be reflected from the bottom of the first particle is $\tau_{B1} = 14.7880us$, the time taken for the ultrasound to be reflected from the top of the second particle is $\tau_{T2} = 14.8418us$, the time taken for the ultrasound to be reflected from the bottom of the second particle is $\tau_{B1} = 14.8591us$ and the time taken for the ultrasound to be reflected from the backwall is calculated as $\tau_{BWc} = 14.9666us$. Using these parameters, eq (47) has been graphed in segments. The mathematically computed FFT of the transmitted signal is

shown in Figure 42, the FFT of the surface and backwall reflections is shown in Figure 43 with zeros occurring at frequencies in MHz at 0, 2.444, 4.888, 7.333, ...., the reflection from the top and bottom of both the particles is shown in Figure 44 with zeros occurring at frequencies in MHz 0, 11.4, 23.08, 34.62,..., the FFT of the entire reflected signal from the sample is shown in Figure 45 and the Power spectral density for the entire signal is shown in Figure 46 with maximum power of the signal noted as $3.92x10^{-5}$.

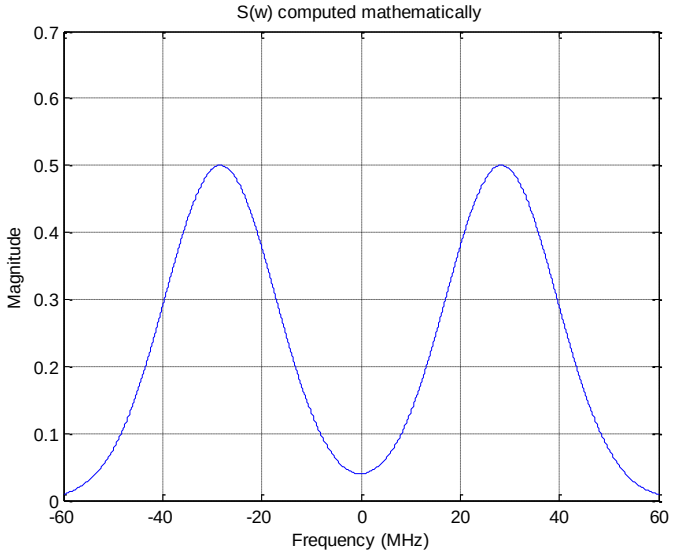


**Figure 42: Mathematically computed FFT of the transmitted signal S(t)**

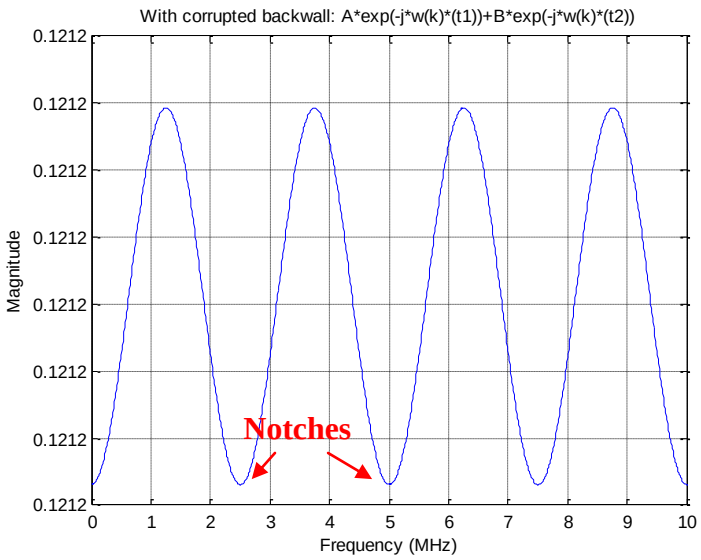


**Figure 43: Mathematically computed FFT for the front and backwall reflections for Case 6**

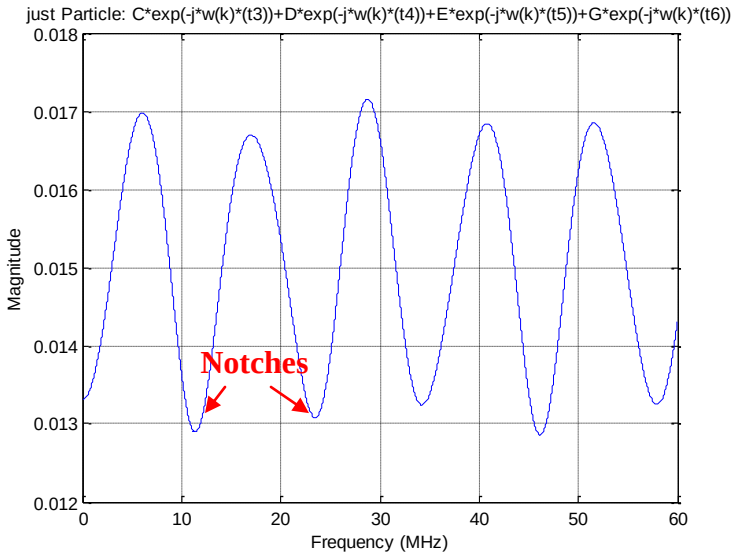


**Figure 44: Mathematically computed FFT for Particle reflections for Case 6**

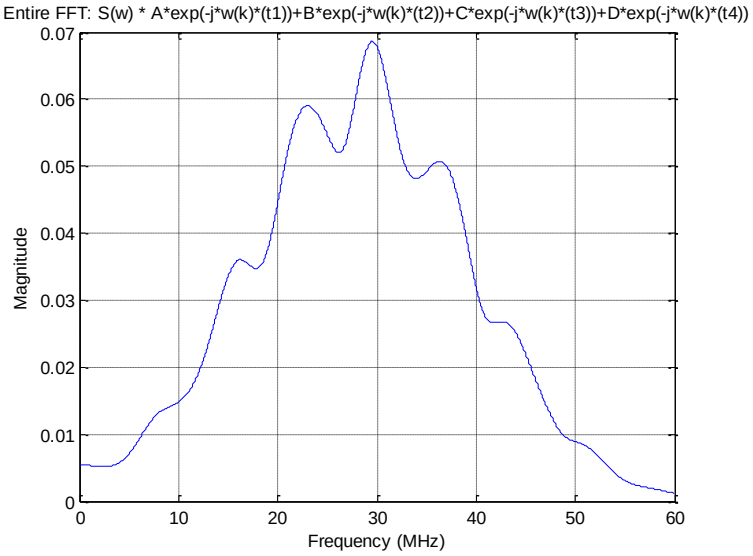


**Figure 45: Mathematically computed FFT for entire reflected signal for Case 6**

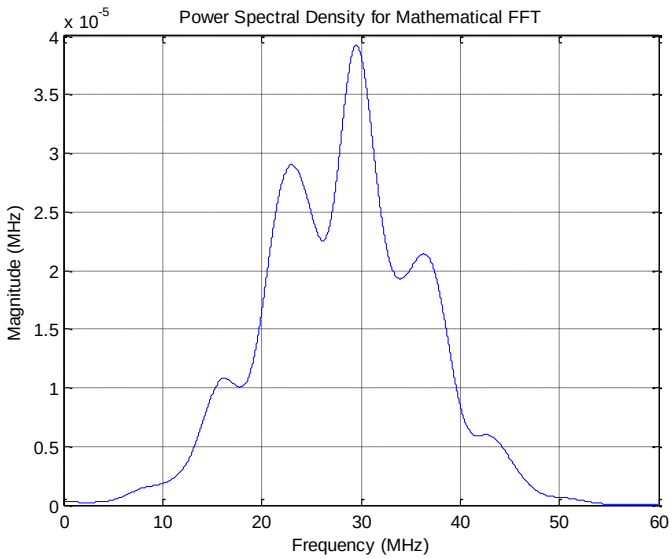


**Figure 46: Power Spectral Density for Case 6**

The power of the signal from the six cases discussed so far with sample thickness of 850um have been tabulated and shown in Table 1. It should be noted that the power

decreased by almost a third in the presence of particle(s) compared to the case with no particles. Although the power decreased further with the increase in depth of the particle as well as increase in size of the particle, the decrease was significantly smaller.

**Table 1: Power Spectral Density Comparison for various cases**

| Particle Size | Particle Depth | Power Spectral Density |
|---|---|---|
| 0 | 0 | 9.36*10^-5 |
| 250um | 250um | 3.9*10^-5 |
| 250um | 300um | 3.825*10^-5 |
| 250um | 500um | 3.89*10^-5 |
| 50um | 250um | 3.915^10^-5 |
| 150um | 250um | 3.91*10^-5 |
| 250um, 50um | 250um, 600um | 3.92*10^-5 |

**Case 7:** The time taken for the ultrasound to be reflected from the surface is $\tau_{FS} = 14.567us$, the thickness of the sample is 1.7mm, particle size is 250um and particle depth is 250um from the surface. The time taken for the ultrasound to be reflected from top of the particle is $\tau_{T1} = 14.7014us$, the time taken for the ultrasound to be reflected from the bottom of the particle is $\tau_{B1} = 14.7880us$ and the time taken for the ultrasound to be reflected from the backwall is calculated as $\tau_{BWc} = 15.433us$. Using these parameters, eq (47) has been graphed in segments. The mathematically computed FFT of the transmitted signal is shown in Figure 47, the FFT of the surface and backwall reflections is shown in Figure 48 with notches occurring at frequencies in MHz at 0, 1.154, 2.309, 3.464, ...., the reflection from the top and bottom of the particle is shown in

Figure 49 with zeros occurring at frequencies in MHz 0, 11.4, 23.08, 34.62,..., the FFT of the entire reflected signal from the sample is shown in Figure 50 and the Power spectral density for the entire signal is shown in Figure 51 with maximum power of the signal noted as $3.9x10^{-5}$.

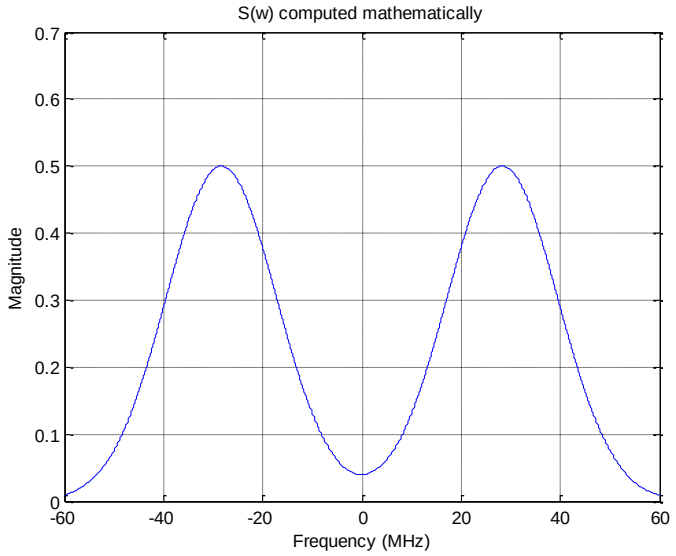


**Figure 47: Mathematically computed FFT of the transmitted signal S(t)**

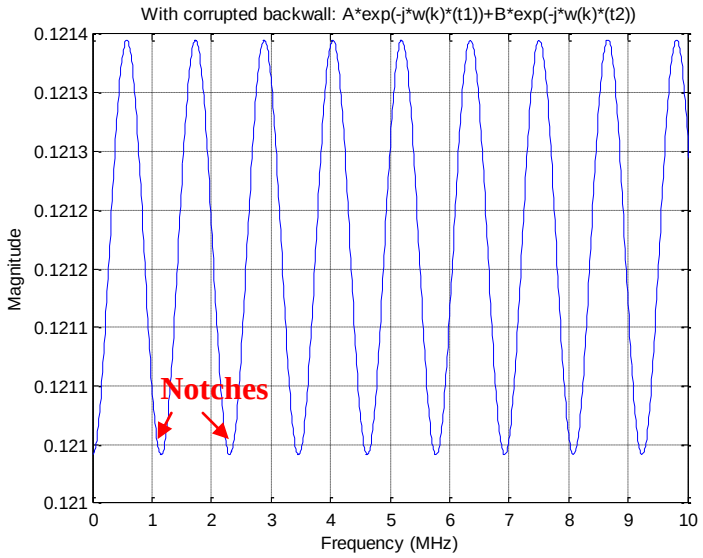


**Figure 48: Mathematically computed FFT for front and backwall reflections for Case 7**

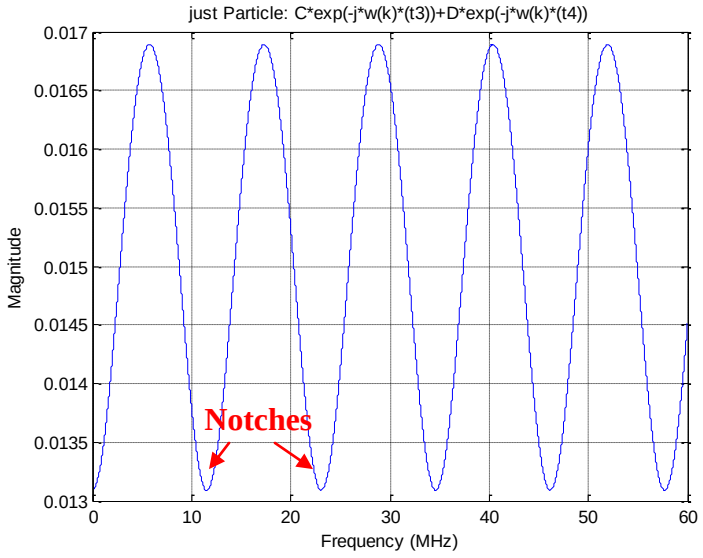


**Figure 49: Mathematically computed FFT for Particle reflection for Case 7**

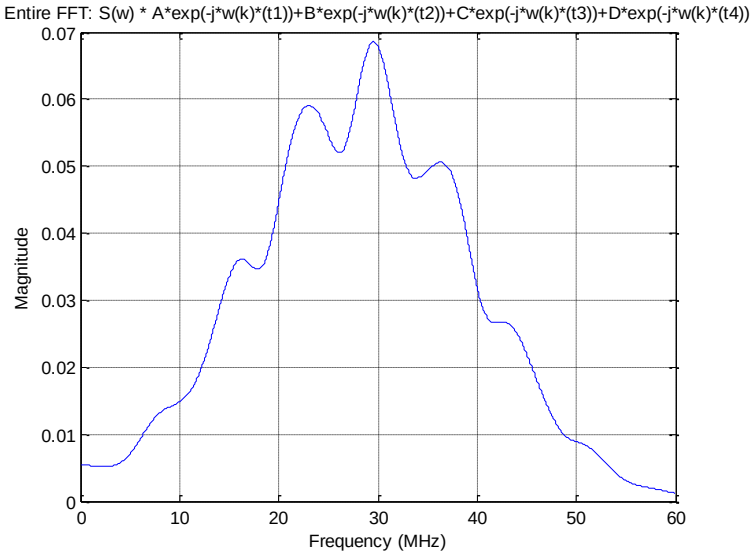


**Figure 50: Mathematically computed FFT for entire reflected signal for Case 7**

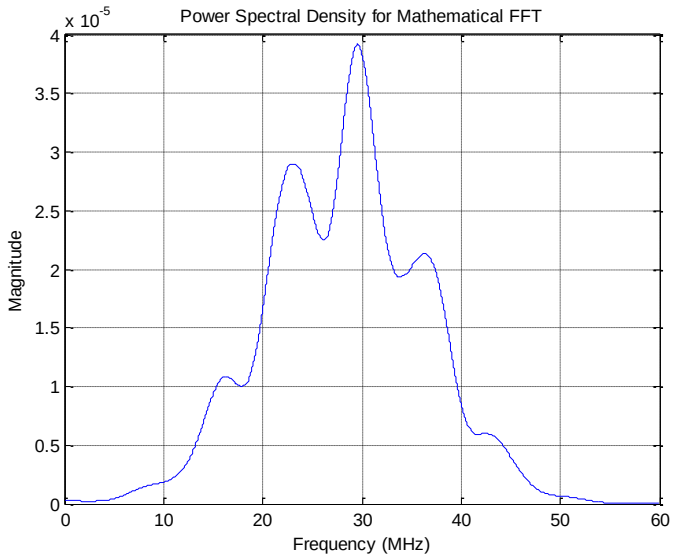


**Figure 51: Power Spectral Density for Case 7**

## 3.4 Conclusions

After analyzing the 7 cases, it was concluded that one particle in the path of the ultrasound reflected most of the ultrasonic signal and the resulting backwall reflection is weak. A second particle in its path has minimal effect in attenuating the backwall reflection further. Adjusting the position of the particle in depth did not have any noticeable impact on the power of the resulting signal. The particle sizes of 50um, 150 and 250um were studied and it was observed that the largest particle size has the most reduction in the signal power. However, the decrease in power with increase in particle size was very small.

# CHAPTER 4: NOISE MITIGATION

## 4.1 Background

In recent years, the correlation between the grain size and ultrasonic attenuation has been utilized to estimate the grain size. An upward shift in the expected frequency of a broadband is a result of scattering caused by grains. This effect can be utilized in evaluating grain size using Fourier Transform (FT) of the backscattered signal that consists of reflections with random amplitudes and phases that correspond to the complex grain structures [1][19]. The existing techniques based on frequency characteristics of grain scattering, include time/Frequency Average [35], linear bandpass filtering [36] [37] and non-linear diverse filtering, including Split Spectrum Minimization (SSM) and SSM with polarity thresholding (SSPTM) [38-45] and Adaptive Filtering [12]. The deconvolution of complex echo signals by the maximum entropy method is discussed in [46-47].

### 4.1.1 Time averaging

A conventional technique such as time averaging discussed in [35] is not effective in eliminating reflection from grains. Therefore, to improve flaw visibility, other methods that are based on the principles of frequency and spatial diversity have been developed.

It may be sufficient to use a simple bandpass filtering technique to improve the signal to noise ratio (SNR) in the cases where the defects and the noise spectra occupy distinct frequency regions. This is especially true when the grain noise echoes are primarily due to Rayleigh scattering. In such cases, the frequency component for the defect occupies the lower part of the received signal spectrum whereas the grain noise components are mainly present in the higher frequency region [21]. However, this technique will not work for mitigating noise caused by filler particles as the frequency component for the resin material and the filler particles do not occupy distinct parts of the frequency spectrum.

### 4.1.2 Split Spectrum Processing

In split spectrum processing (SSP) [2 6 7 48-52], a wideband signal is transmitted and the received signal spectrum is partitioned into different frequency bands. This is achieved by using spectral windows to obtain a set of de-correlated signals. Noise suppression algorithms can be applied to the resulting data to enhance the flaw signal once the de-correlation of the grain echoes has been achieved through SSP. The need for complex modulation techniques of multiple transmitters to achieve frequency diverse signals at the receiver is eliminated when SSP is used [11][53]. However, it is difficult to employ this technique in a practical application in industry as SSP is sensitive to processing parameters such as center frequencies and bandwidth of the filter bank [3].

#### 4.1.2.1 Polarity Thresholding (PT) Algorithm

The time instants where the flaw signal is present, the corresponding SSP data will not exhibit a polarity reversal. This is because the grain noise is dominated by the flaw signal. However, if only grain noise is present in the data set that is zero-mean, then it is likely that the data will exhibit polarity reversal. Based on this principle, polarity thresholding was developed [54][55]. The amplitude of the processed signal is set to zero at the time instants where the polarity reversal occurs but when the data set has identical polarity, it maintains the original value of the unprocessed wideband signal. This results in significant reduction in grain noise. Alternatively, the non- zero portion of the PT data can be obtained from the output of any SSP algorithm. Therefore, the polarity thresholding algorithm is a non-linear process which may be used in conjunction with other SSP algorithms to improve their performance. The PT output can be expressed as [53]

$$y(t_k) = \begin{cases} r(t_k) & if\ r_i(t) > 0\ or\ r_i(t) < 0\ ; \quad for\ all\ i = 1, 2, \dots N \\ 0; & Otherwise \end{cases} \dots\dots\dots\dots\dots (91)$$

where the $t_k$ are discrete time instants with k=1,2...N

To improve the ultrasonic detection in diagnostic and industrial applications where the coherent noise due to random scatterers can mask the target echo, the PT algorithm can be effectively used [2-3][11]. However, this method is sensitive to parameter tuning. The process of tuning can be time consuming and difficult [53]. The two problems associated with tuning are

1. The need for A-scans that contain well documented target echoes.

2. The limited understanding of the effect of the parameters on the performance of the algorithm.

### 4.1.3 Cross-Correlation

If a reference signal is available to match with a real signal, Cross-Correlation can be used. This is a commonly used signal processing technique. For example, it can be used in radar where the transmitted pulse is cross-correlated with the received signal to locate a reflection in a noisy signal. This is often referred to as matched filtering. To find the degree of similarity between two signals, the two signals can be cross-correlated. When the resulting output of the cross-correlation between two signals is at its maximum, it means that is the point where the two signals have the greatest similarity. The cross-correlation of two discrete signals ($f[n]$ and $h[n]$) is defined as [56]

$$g[n] = \sum_{m=-\infty}^{\infty} f[m]h[n+m] \ldots\ldots\ldots\ldots\ldots\ldots\ldots\ldots\ldots\ldots\ldots\ldots\ldots\ldots\ldots (92)$$

This technique is not suitable for differentiating between reflections and dispersive wave modes since the frequency range of the received signal including the coherent noise is the same as that of the transmitted signal. Therefore, the degree of correlation between the transmitted signal and the received signal with the noise is always high.

### 4.1.4 Wavelet Transforms and De-Noising

Wavelet Transforms [3][57-60] due to their localization properties that adapt better to the characteristics of the signal and image have received increased attention over

the years [61]. This is a signal processing technique that allows the signal of interest to be examined in the time and frequency domains simultaneously and is described in full by Addison [62]. The wavelet transform has been used in conventional ultrasonic testing [63-70]. Wavelet Analysis, including continuous and discrete wavelet analysis, has been used to analyze the ultrasonic guided waves employed in pipeline inspection [57] [71]. Wavelet analysis has become a well-established signal-processing technique for removing noise from ultrasonic signals to enhance the SNR in ultrasonic non-destructive testing and evaluation of strong-sound scattering materials. The wavelet transform is used as a bandpass filter to reduce noise [72]. Basic wavelet de-noising employs the discrete wavelet transform (DWT) [73-75]. Wavelet de-noising is a thresholding [76][77] procedure that reduces the smaller amplitudes of the decomposed signals. This could further reduce parts of the signal that have a low level of correlation with the wavelet. Wavelet de-noising has the effect of preserving the overall shape of the signal while reducing lower amplitude components. That is, it removes small amplitudes regardless of frequency as opposed to smoothing where high frequencies are removed, regardless of amplitude.

The de-noising technique can be described as follows [16]:

- The noisy input signal is decomposed into N levels of approximations and detailed coefficients using the selected wavelet transform.
- Thresholding of coefficients.
- The signal is reconstructed using the approximations and detailed coefficients by means of the inverse transform.

There are a number of techniques for determining the threshold that is used [62, 77]. Lazaro et al. [77] and Kazanavicius et al. [78] described the use of wavelet de-noising for conventional ultrasonic testing.

The continuous wavelet transform (CWT) of a signal y(t) is defined as convolution between the signal y(t) and wavelet $\psi_{a,b}(t)$:

$$W_y(a,b) = \int_{-\infty}^{\infty} y(t).\frac{1}{\sqrt{a}}\psi^*(\frac{t-b}{a})\text{dt} \quad \text{.....(93)}$$

where the mother wavelet is a zero average function, centered around zero with finite energy [3]. The family of daughter wavelets are obtained by translating and dilatations of the mother wavelet ψ(t):

$$\psi_{a,b}(t) = \frac{1}{\sqrt{a}}\psi(\frac{t-b}{a}) \quad \text{.....(94)}$$

where a and b are, respectively, the scale and the translation factors. The wavelet function $\psi_{a,b}(t)$ is centered on b.

An image processing method based on wavelets that is commercially available today has been used to process a corrupted image. This corrupted backwall image is shown in Figure 52 a. The processed image is shown in Figure 52 b. It can be seen that the effect of the filler particles in some areas have been mitigated. However, new artifacts are noted in the image which is not a desirable effect.

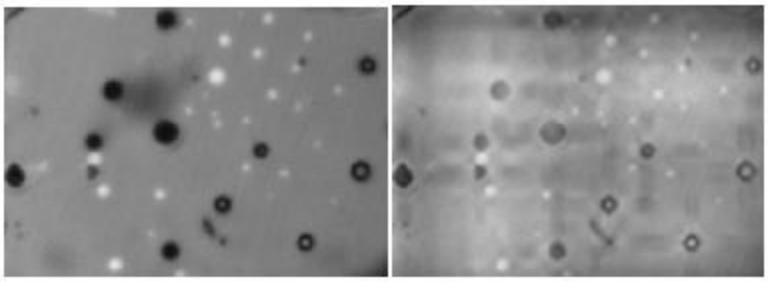

**(a)** **(b)**

**Figure 52: (a) Backwall image of a sample with filler particles (b) Processed image using a commercially available wavelet based technique**

### 4.1.5 Adaptive filtering

Conventional linear filtering methods such as correlation receiver and Wiener filter have been proven successful in previous signal detection applications. However, both implementations require some a-priori knowledge of the flaw signal and noise characteristics [21].

In the research work of [21] non-linear statistical filtering techniques using frequency diverse observations are examined which utilize the adaptive properties to improve flaw detection. A robust statistical filtering technique was discussed. While successful cases of implementing this technique were discussed, the technique fails if the spectral range is increased beyond a typical frequency range of the 5MHz transducer.

An adaptive 2-dimensional filter [79] for suppression of speckle from ultrasonic pulse-echo images, based on the use of the ratio of the local variance and local mean of the image to recognize those parts of the image which require maximum and minimum smoothing, has been found to perform well in preliminary tests on clinical images. It is

expected that the use of appropriate combinations of a range of texture features will produce even better results.

Adaptive filtering and detection was used for ultrasonic evaluation of highly scattering materials and presented in [12]. The adaptive filter presented in this paper is developed from the widely used technique of adaptive noise cancellation [80][81]. In this, the coherent noise in a signal can be suppressed provided the correlated noise in a signal is available. A adaptive filtering setup is shown in Figure 53.

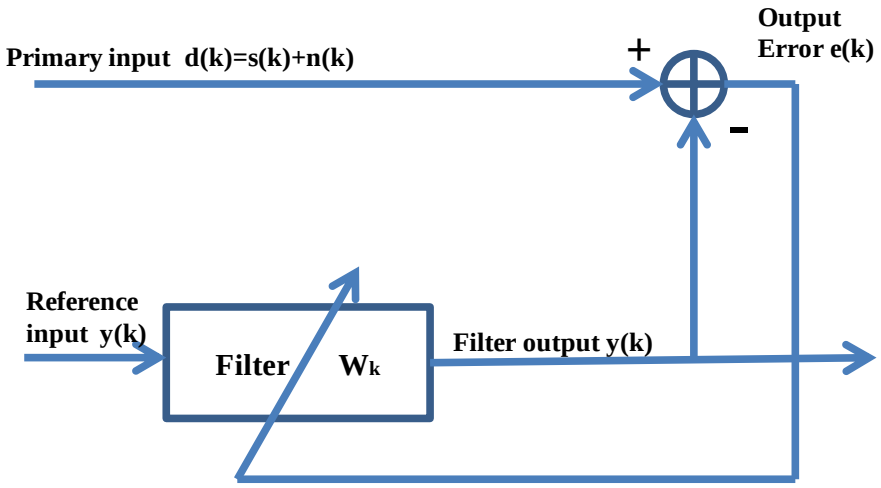


**Figure 53: Adaptive Filter with Independent Reference Signal**

Here it was assumed that the primary input d(k) can be written as d(k) = s(k) + n(k) where s(k) and n(k) are the desired target echo and the grain noise, respectively, s(k), n(k) and y(k) are all statistically stationary and n(k) is white noise with mean power $p_n$. The signal x(k) is the reference input and y(k) is the filter output. The mean square error is given by [82]

$$E[e^2(k) = E[(d(k) - y(k))^2] \text{.....(95)}$$

$$E[e^2(k)] = E\left[\left(\left(s(k) - y(k)\right) + n(k)\right)^2\right] \text{... ... ... ... ... ... . (96)}$$

$$= E\left[\left(s(k) - y(k)\right)^2 + n^2(k) + 2n(k)\left(s(k) - y(k)\right)\right] \text{... ... ... ... (97)}$$

It is assumed that y(k) is correlated with s(k) but n(k) is uncorrelated with either s(k) or y(k). This results in

$$E[e^2(k)] = E\left[\left(s(k) - y(k)\right)^2 + n^2(k)\right] \text{... ... ... ... ... ... ... (98)}$$

$$= E\left[\left(s(k) - y(k)\right)^2\right] + p_n \text{ .....(99)}$$

When the filter is optimized, the mean square error will be a minimum i.e.,

$$\min\{E[e^2(k)]\} = \min\left\{E\left[\left(s(k) - y(k)\right)^2\right]\right\} + p_n \text{.....(100)}$$

Since the possible minimum achieved is zero, the smallest possible mean error is

$$E[e^2(k)]_{min} = p_n \text{ .....(101)}$$

If this is achieved, the filter output is completely noise free i.e., y(k) =s(k). Good performance of the adaptive filter is achieved if a true defect signal in the reference input is more closely correlated with the defect in the primary input, than is the corresponding grain noise in the two inputs. One of the major disadvantages of adaptive filtering is that it can only handle processes with additive noise.

### 4.1.6 Deconvolution

A method for signal processing based on frequency deconvolution technique has been used to enhance the axial resolution in an ultrasonic system. This is done by suitable processing of the received output. The image reconstruction is based on an algorithm

evaluating the reflected and scattered signals in the A-scans. The A-scans are modeled as a response of the imaged object convolved with the shape of the ultrasonic pulse, which is determined by the transfer function of the transducers and excitation [83].

A multi-pattern adaptive inverse filter for real-time deconvolution of ultrasonic signals in scattering media is discussed in [84]. This work provides a real-time deconvolution method which considers signal distortion of the ultrasonic signal traveling in dispersive materials. The deconvolution method is based on an inverse filter whose coefficients are computed by an adaptive algorithm from a set of pattern signals scanned at different depths of the tested material. This method employs reference signals from several depths for the determination of the inverse filter coefficients. The received pulse echo signal y(t) can be represented as [83]

$$y(t) = w(t) * x(t) + n(t) \dots\dots\dots\dots\dots\dots\dots\dots\dots\dots (102)$$

where x(t) is the medium response, w(t) is the ultrasound system response and n(t) is the zero mean Gaussian noise and (*) represents convolution.

Deconvolution attempts to remove the effects of the input function w(t) from the output y(t) to achieve some close approximation of the original medium impulse response u(t). The Fourier Transform of the convolution of two function can be represented as multiplication of the Fourier Transforms.

$$Y(\omega) = W(\omega)X(\omega) \text{ .....(103)}$$

$$X(\omega) = \frac{Y(\omega)}{W(\omega)} \text{ .....(104)}$$

where Y and W denote the Fourier transforms of y and w. Also,

$$X(\omega) = \frac{YW^*}{WW^*+\varepsilon} \text{.....(105)}$$

where $W^*$ is the complex conjugate of W and ε represents the regularization parameter which is a small positive number used as a damping factor. The regularization parameter as a filter has been used to improve the estimation of the reflectivity function. This parameter has been used to control the noise content in the deconvolution result. This method was effectively used in some real time 2-D and 3-D biological tissue imaging.

## 4.2 Transfer Function Based Approach

The effect of filler particles in the time domain is not additive noise. Therefore, the clean resin signal cannot be subtracted from the received corrupted signal to model the noise. The reflections caused by filler particles is convolved with the clean resin signal, hence, modeling the noise in the time domain is mathematically complex. As discussed in Chapter 4.1.6, Deconvolution attempts to remove the effects of the input function w(t) from the output y(t) to achieve some close approximation of the original medium impulse response u(t). The Fourier Transform of the convolution of two functions can be represented as multiplication of the Fourier Transforms.

Based on the Deconvolution technique an Inverse Filter approach was explored. For a given transducer, the received signal y(t) can be expressed in the form of a convolution [70]

$$y(t) = x(t)*h(t) \quad \text{.....(106)}$$

where (*) means convolution, x(t) is the reference signal containing those factors that are not dependent on the inspection geometry. The function h(t) is the impulse response of

the system. The impulse response depends on the x-y location, but it is in terms of time. The deconvolution process finds an estimation of h(t) from x(t) and y(t).

$$H(\omega) = \frac{Y(\omega)}{X(\omega)} \quad \text{.....(107)}$$

where Y and X are Fourier transforms.

A noise model was developed based on frequency domain analysis of the modeled signals. In the time domain, the signal is modeled as convolution of two signals

$$s1(t) = s(t) * n(t) \quad \text{.....(108)}$$

where s(t) is the modeled reflected signal from the backwall of a clean sample, n(t) is the interference caused by the filler particles and s1(t) is the modeled reflected signal from the backwall of the sample with particles. In the frequency domain, the signal is modeled as

$$S_1(\omega) = S(j\omega)N(j\omega) \quad \text{.....(109)}$$

$$N(j\omega) = \frac{S_1(j\omega)}{S(j\omega)} \quad \text{.....(110)}$$

### 4.2.1 Frequency Domain Analysis of the Models

The ultrasonic signal reflected from a sample that has "n" particles is given by eq (46). This equation can be written as

$$\Im\{S_{CO}(t)\} = \Im\{S(t)\}[R_{FS}\beta_{FS}e^{-j\omega\tau_{FS}} + R_{BWc}\beta_{BWc}e^{-j\omega\tau_{BWc}} + \sum_{i=1}^{n} R_{Ti}\beta_{Ti}\,e^{-j\omega\tau_{Ti}} + \sum_{i=1}^{n} R_{Bi}\beta_{Bi}\,e^{-j\omega\tau_{Bi}}]. \quad \text{.....(111)}$$

By dividing eq (111) with eq.(16), we get

$$\frac{\Im\{S_{CO}(t)\}}{\Im\{S_{CL}(t)\}} = \frac{\Im\{S(t)\}[R_{FS}\beta_{FS}e^{-j\omega\tau_{FS}} + R_{BWc}\beta_{BWc}e^{-j\omega\tau_{BWc}} + \sum_{i=1}^{n}(R_{Ti}\beta_{Ti}\,e^{-j\omega\tau_{Ti}} + R_{Bi}\beta_{Bi}\,e^{-j\omega\tau_{Bi}})]}{\Im\{S(t)\}[R_{FS}\beta_{FS}\,e^{-j\omega\tau_{FS}} + R_{BW}\beta_{BW}e^{-j\omega\tau_{BW}}]} \text{..(112)}$$

The transfer function

$$N(\omega) = \frac{\Im\{S_{CO}(t)\}}{\Im\{S_{CL}(t)\}} = \frac{[R_{FS}\beta_{FS}e^{-j\omega\tau_{FS}} + R_{BWc}\beta_{BXc}e^{-j\omega\tau_{BWc}} + \sum_{i=1}^{n}(R_{Ti}\beta_{Ti}\,e^{-j\omega\tau_{Ti}} + R_{Bi}\beta_{Bi}\,e^{-j\omega\tau_{Bi}})]}{[R_{FS}\beta_{FS}\,e^{-j\omega\tau_{FS}} + R_{BW}\beta_{BW}e^{-j\omega\tau_{BW}}]} \text{...(113)}$$

Dividing numerator and denominator with $R_{FS}\beta_{FS}e^{-j\omega\tau_{FS}}$ , we get

$$N(\omega) = \frac{[1 + \frac{R_{BWc}\beta_{BWc}e^{-j\omega\tau_{BWc}}}{R_{FS}\beta_{FS}e^{-j\omega\tau_{FS}}} + \frac{1}{R_{FS}\beta_{FS}e^{-j\omega\tau_{FS}}}\sum_{i=1}^{n}(R_{Ti}\beta_{Ti}\,e^{-j\omega\tau_{Ti}} + R_{Bi}\beta_{Bi}\,e^{-j\omega\tau_{Bi}})]}{[1 + \frac{R_{BW}\beta_{BW}e^{-j\omega\tau_{BW}}}{R_{FS}\beta_{FS}e^{-j\omega\tau_{FS}}}]} \text{.....(114)}$$

Since $R_{BW} = R_{BWc} = -R_{FS}$ and $R_{Bi} = -R_{Ti}$ , the above equation can be written as

$$N(\omega) = \frac{[1 - \frac{R_{FS}\beta_{BWc}e^{-j\omega\tau_{BWc}}}{R_{FS}\beta_{FS}e^{-j\omega\tau_{FS}}} + \frac{1}{R_{FS}\beta_{FS}e^{-j\omega\tau_{FS}}}\sum_{i=1}^{n}R_{Ti}(\beta_{Ti}\,e^{-j\omega\tau_{Ti}} - \beta_{Bi}\,e^{-j\omega\tau_{Bi}})]}{[1 - \frac{R_{FS}\beta_{BW}e^{-j\omega\tau_{BW}}}{R_{FS}\beta_{FS}e^{-j\omega\tau_{FS}}}]} \text{.....(115)}$$

Simplifying the above equation, we get

$$N(\omega) = \frac{[1 - \frac{\beta_{BWc}}{\beta_{FS}}e^{-j\omega(\tau_{BWc}-\tau_{FS})} + \frac{1}{R_{FS}\beta_{FS}}\sum_{i=1}^{n}R_{Ti}(\beta_{Ti}\,e^{-j\omega(\tau_{Ti}-\tau_{FS})} - \beta_{Bi}\,e^{-j\omega(\tau_{Bi}-\tau_{FS})})]}{[1 - \frac{\beta_{BW}}{\beta_{FS}}e^{-j\omega(\tau_{BW}-\tau_{FS})}]} \text{.....(116)}$$

For single particle case,

$$N(\omega) = \frac{[1 - \frac{\beta_{BWc}}{\beta_{FS}} e^{-j\omega(\tau_{BWc} - \tau_{FS})} + \frac{R_{T1}\beta_{T1} e^{-j\omega(\tau_{Ti} - \tau_{FS})}}{R_{FS}\beta_{FS}} + \frac{R_{B1}\beta_{B1} e^{-j\omega(\tau_{Bi} - \tau_{FS})}}{R_{Fs}\beta_{FS}}]}{[1 - \frac{\beta_{BW}}{\beta_{FS}} e^{-j\omega(\tau_{BW} - \tau_{FS})}]} \quad \text{.....(117)}$$

Let $\alpha_1 = \frac{\beta_{BW}}{\beta_{FS}}; \alpha_2 = \frac{\beta_{BWc}}{\beta_{FS}}$; $\beta_1 = \frac{R_{T1}\beta_{T1}}{R_{Fs}\beta_{FS}}$; $\beta_2 = \frac{R_{B1}\beta_{B1}}{R_{FS}\beta_{FS}}$; $T = \tau_{BW} - \tau_{FS}$; $T_1 = \tau_{T1} - \tau_{FS}$

$T_2 = \tau_{B1} - \tau_{FS}$ and $T_3 = \tau_{BWc} - \tau_{FS}$

$$H(s) = \frac{[1 + \beta_1 e^{-sT_1} + \beta_2 e^{-sT_2} - \alpha_2 e^{-sT_3}]}{[1 - \alpha_1 e^{-sT}]} \quad \text{.....(118)}$$

**Case 1:** For a sample thickness of 832um, and a particle size of 77um and particle depth of 50um, $T = \tau_{BW} - \tau_{FS}$; $T_1 = \tau_{T1} - \tau_{FS}$ $T_2 = \tau_{B1} - \tau_{FS}$ and $T_3 = \tau_{BWc} - \tau_{FS}$

To identify the poles of the transfer function, we first write

$$H_1(s) = [1 - \alpha_1 e^{-sT}] \quad \text{.....(119)}$$

Using the same method discussed in Chapter 3, the real part of the pole is determined as $\sigma = -\frac{1}{T}\ln\frac{1}{|\alpha_1|}$, where $\alpha_1 = 0.7549$, $\tau_{FS} = 14.567us$, $\tau_{BW} = 15.0142us$ and $T = 0.4472us$.

Hence, $\sigma = -0.6287$. Since $\alpha_1$ is positive and real, $\omega = \pm 0, \pm\frac{2\pi}{T}, \pm\frac{4\pi}{T}, \pm\frac{6\pi}{T}, \ldots$. The poles of the transfer function are shown in Figure 54.

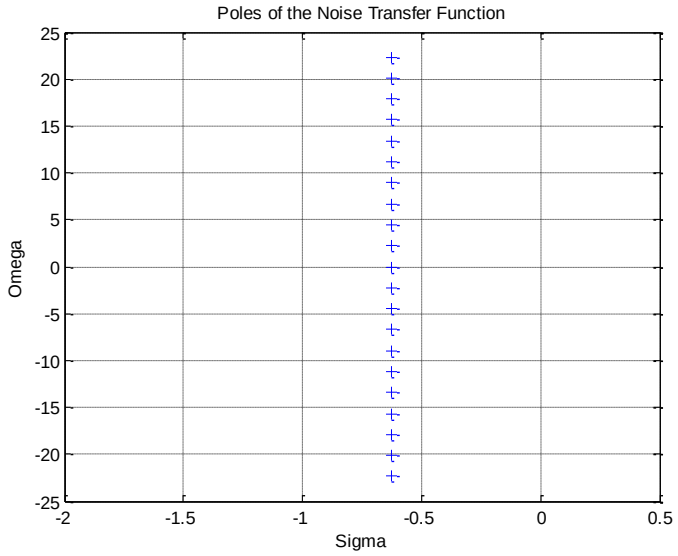


**Figure 54: Poles for the Noise Transfer Function N(ω)**

To identify the zeros of the transfer function, we first write

$$H_2(s) = [1 + \beta_1 e^{-sT_1} + \beta_2 e^{-sT_2} - \alpha_2 e^{-sT_3}] \quad \text{.....(120)}$$

$T = 0.4472us$; $T_1 = 0.0269us$ $T_2 = 0.0536us$ and $T_3 = 0.4325$. Therefore $T_2 = 2T_1$ and

$T_3 = 16T_1$; $\beta_1 = 1.0194$; $\beta_2 = -1.0451$; $\alpha_2 = 0.7683$

$$H_2(s) = [1 + 0.0194e^{-sT_1} - 1.0451e^{-2sT_1} - 0.7683e^{-16sT_1}] \quad \text{.....(121)}$$

Let $x = e^{-sT_1}$

$$H_2(x) = [1 + 0.0194x - 1.0451x^2 - 0.7683x^{16}] \quad \text{.....(122)}$$

Using MATLAB, the zeros of $H_2(x)$ were computed and shown in Table 2.

**Table 2: Zeros of $H_2(x)$ with 77um particle size**

| Cartesian | Angle | Magnitude |
|---|---|---|
| 0.9387 + 0.3052i | 0.3143 | 0.9871 |
| 0.9387 - 0.3052i | -0.3143 | 0.9871 |
| 0.9063 | 0 | 0.9063 |
| 0.7747 + 0.6926i | 0.7295 | 1.0392 |
| 0.7747 - 0.6926i | -0.7295 | 1.0392 |
| 0.4333 + 0.9687i | 1.1502 | 1.0612 |
| 0.4333 - 0.9687i | -1.1502 | 1.0612 |
| -0.0007 + 1.0677i | 1.5715 | 1.0677 |
| -0.0007 - 1.0677i | -1.5715 | 1.0677 |
| -0.4347 + 0.9681i | 1.9928 | 1.0612 |
| -0.4347 - 0.9681i | -1.9928 | 1.0612 |
| -0.7760 + 0.6911i | 2.414 | 1.0391 |
| -0.7760 - 0.6911i | -2.414 | 1.0391 |
| -0.9393 + 0.3012i | 2.8313 | 0.9864 |
| -0.9393 - 0.3012i | -2.8313 | 0.9864 |
| -0.8986 | 3.1416 | 0.8986 |

To determine the zeros of $e^{-sT_1}$, let $s = \sigma + j\omega$. Since $x = e^{-sT_1}$, we can write

$$e^{-(\sigma + j\omega)T_1} = 0.9063 \quad \text{.....(123)}$$

$$e^{-\sigma T_1} e^{-j\omega T_1} = 0.9063 \quad \text{.....(124)}$$

$$\sigma = \frac{-1}{T_1} \log(0.9063) \quad \text{.....(125)}$$

Therefore, $\sigma = 3.6574$ and $\omega = 0$ radians. Also,

$$e^{-(\sigma + j\omega)T_1} = 0.9871 \angle 0.3143 \quad \text{.....(126)}$$

$$e^{-\sigma T_1} e^{-j\omega T_1} = 0.9871 \angle 0.3143 \quad \text{.....(127)}$$

$$e^{-\sigma T_1} = 0.9871 \quad \text{.....(128)}$$

$$e^{-j\omega T_1} = \angle 0.3143 \quad \text{.....(129)}$$

Therefore, $\sigma = 0.4827$ and $\omega = 43.0263$ radians

Similary,

$$e^{-(\sigma + j\omega)T_1} = 0.9871\angle -0.3143 \quad \text{.....(130)}$$

$$e^{-\sigma T_1} e^{-j\omega T_1} = 0.9871\angle -0.3143 \quad \text{.....(131)}$$

$$e^{-\sigma T_1} = 0.9871 \quad \text{.....(132)}$$

$$e^{-j\omega T_1} = \angle -0.3143 \quad \text{.....(133)}$$

Therefore, $\sigma = 0.4827$ and $\omega = -43.0263$ radians. After computing all the zeros for $e^{-(\sigma + j\omega)T_1}$, the sigma to omega plot is shown in Figure 55. The frequency response of the transfer function for this case is shown in Figure 56.

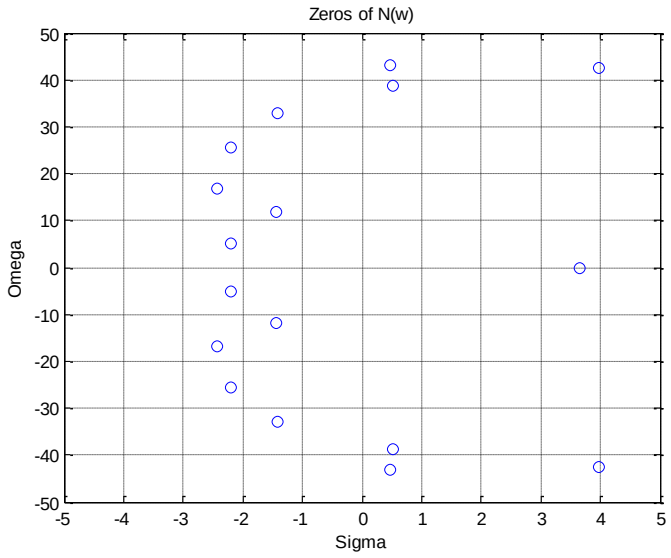


**Figure 55: Zeros for the Noise Transfer Function N(ω) with 77um particle**

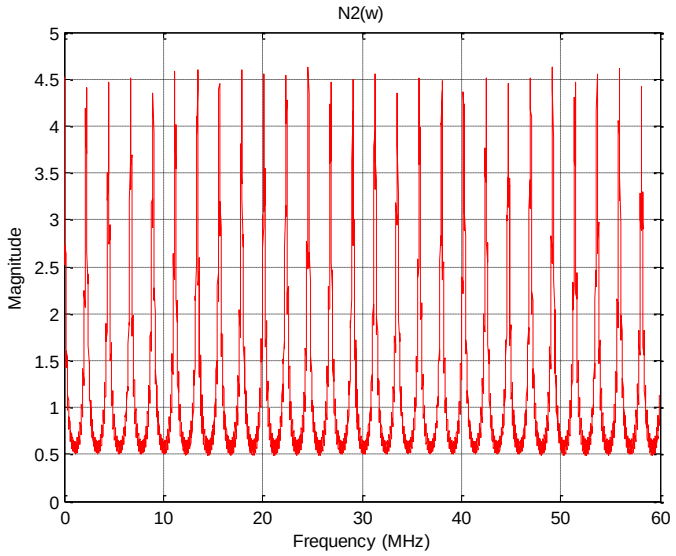


**Figure 56: Frequency Response of the Noise Transfer Function N(ω) for 77um case**

**Case 2:** For a sample thickness of 832um, a particle size of 232um and particle depth of 50um, the zeros are computed as shown below. The poles are not affected by the size of the particle. Therefore, they remain unchanged.

$$H_2(s) = [1 + \beta_1 e^{-sT_1} + \beta_2 e^{-sT_2} - \alpha_2 e^{-sT_3}] \quad \text{.....(134)}$$

$T = 0.4472us$; $T_1 = 0.0269us$ $T_2 = 0.1073us$ and $T_3 = 0.4029$. Therefore $T_2 = 4T_1$ and $T_3 = 15T_1$; $\beta_1 = 1.0194$; $\beta_2 = -1.0451$; $\alpha_2 = 0.7683$

$$H_2(s) = [1 + 0.0194e^{-sT_1} - 1.0451e^{-4sT_1} - 0.7683e^{-15sT_1}] \quad \text{.....(135)}$$

$$H_2(x) = [1 + 0.0194x - 1.0451x^4 - 0.7683x^{15}] \quad \text{.....(136)}$$

Using MATLAB, the zeros of $H_2(x)$ were computed and shown in Table 3.

**Table 3: Zeros of $H_2(x)$ with 232um particle size**

| Cartesian | Angle | Magnitude |
|---|---|---|
| 0.9797 + 0.3619i | 0.3539 | 1.0444 |
| 0.9797 - 0.3619i | -0.3539 | 1.0444 |
| 0.927 | 0 | 0.927 |
| 0.7141 + 0.8094i | 0.8479 | 1.0794 |
| 0.7141 - 0.8094i | -0.8479 | 1.0794 |
| 0.2349 + 0.9885i | 1.3375 | 1.016 |
| 0.2349 - 0.9885i | -1.3375 | 1.016 |
| -0.0566 + 0.9337i | 1.6313 | 0.9354 |
| -0.0566 - 0.9337i | -1.6313 | 0.9354 |
| -0.4864 + 0.9437i | 2.0467 | 1.0617 |
| -0.4864 - 0.9437i | -2.0467 | 1.0617 |
| -0.8865 + 0.6048i | 2.5429 | 1.0732 |
| -0.8865 - 0.6048i | -2.5429 | 1.0732 |
| -0.9626 + 0.1247i | 3.0128 | 0.9706 |
| -0.9626 - 0.1247i | -3.0128 | 0.9706 |

The zeros and the frequency response of the transfer function for this case are shown in Figure 57 and Figure 58 respectively.

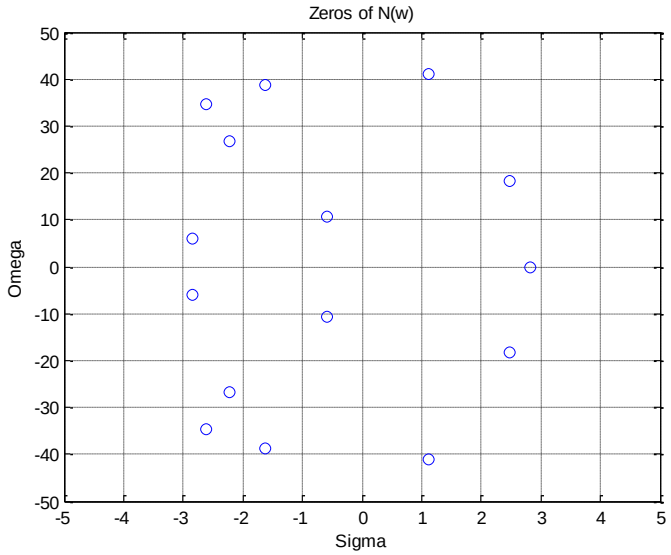


**Figure 57: Zeros of the Noise Transfer Function N(ω) with particle size of 232um**

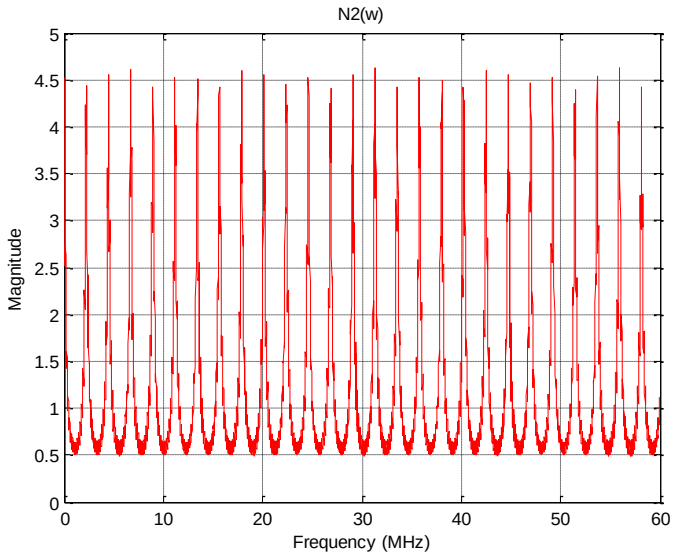


**Figure 58: Frequency Response of the Noise Transfer Function N(ω) with particle size of 232um**

**Case 3:** For a sample thickness of 832um, and a particle size of 383um and particle depth of 50um, the zeros are computed as shown below. The poles do not change since the thickness of the sample did not change.

$$H_2(s) = [1 + \beta_1 e^{-sT_1} + \beta_2 e^{-sT_2} - \alpha_2 e^{-sT_3}] \quad \text{.....(137)}$$

$T = 0.4472us$; $T_1 = 0.0269us$ $T_2 = 0.1596us$ and $T_3 = 0.3741$. Therefore $T_2 = 6T_1$ and $T_3 = 14T_1$; $\beta_1 = 1.0194$; $\beta_2 = -1.0451$; $\alpha_2 = 0.7683$

$$H_2(s) = [1 + 0.0194e^{-sT_1} - 1.0451e^{-6sT_1} - 0.7683e^{-14sT_1}] \quad \text{.....(138)}$$

$$H_2(x) = [1 + 0.0194x - 1.0451x^6 - 0.7683x^{14}] \quad \text{.....(139)}$$

Using MATLAB, the zeros of $H_2(x)$ were computed and shown in Table 4.

**Table 4: Zeros of $H_2(x)$ with 383um particle size**

| Cartesian | Angle | Magnitude |
|---|---|---|
| 0.9979 + 0.4466i | 0.4208 | 1.0933 |
| 0.9979 - 0.4466i | -0.4208 | 1.0933 |
| 0.9372 | 0 | 0.9372 |
| 0.5465 + 0.7962i | 0.9693 | 0.9657 |
| 0.5465 - 0.7962i | -0.9693 | 0.9657 |
| 0.3130 + 1.0001i | 1.2675 | 1.0479 |
| 0.3130 - 1.0001i | -1.2675 | 1.0479 |
| -0.3157 + 1.0005i | 1.8765 | 1.0491 |
| -0.3157 - 1.0005i | -1.8765 | 1.0491 |
| -0.5466 + 0.7920i | 2.1749 | 0.9623 |
| -0.5466 - 0.7920i | -2.1749 | 0.9623 |
| -0.9972 + 0.4450i | 2.7219 | 1.092 |
| -0.9972 - 0.4450i | -2.7219 | 1.092 |
| -0.9332 | 3.1416 | 0.9332 |

The zeros and the frequency response for the transfer function for this case is shown in Figure 59 and Figure 60 respectively.

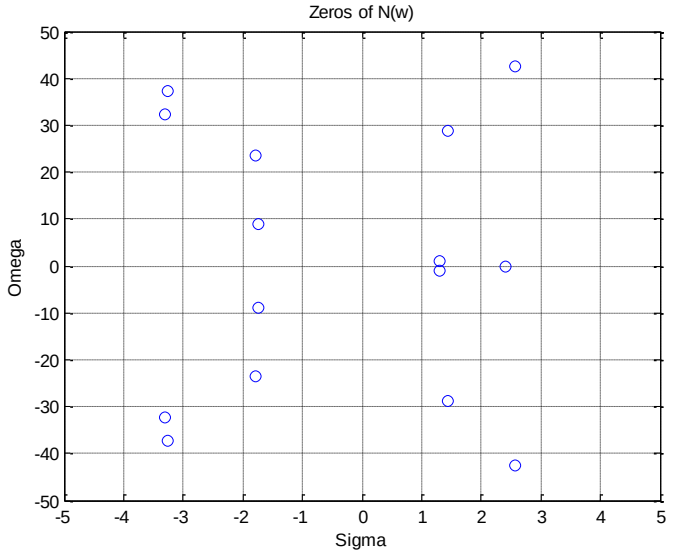


**Figure 59: Zeros of the Noise Transfer Function N(ω) with particle size of 383um**

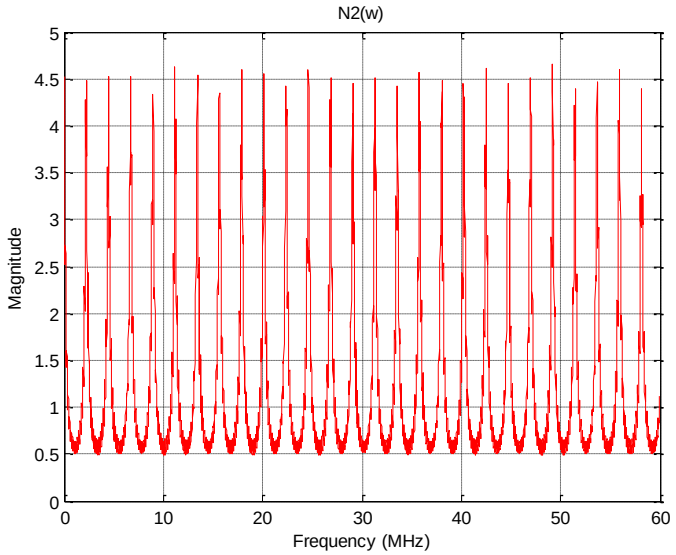


**Figure 60: Frequency Response of the Noise Transfer Function N(ω) with particle size of 232um**

## 4.3 Conclusions

The poles and zeros of the noise transfer function for 3 different particle sizes were analyzed. With increase in particle size, the change in the values of sigma was more noticeable than the change in the values of Omega. Also, the number of zeros in the right hand plane increased with the increase in the particle size. The frequency response for the noise transfer function was also analyzed of the 3 cases. A very subtle change in the magnitude was noticed at some select frequencies with increase in particle size, but no other conclusions could be drawn.

# CHAPTER 5: RESULTS FOR SIMULATED STRUCTURE

## 5.1 Comparison of Mathematical FFT to MATLAB FFT

In order to confirm that the mathematical (analytical) FFT of the ultrasonic reflections matched with the result obtained using the FFT command in MATLAB to convert time domain signal for the ultrasonic reflections, a test was conducted. The mathematical FFT of a ultrasonic reflections from a clean sample given by

$$\Im\{S_{CL}(t)\} = \frac{1}{2}\left[ e^{\frac{-(\omega+2\pi f_c)^2}{4\alpha}} + e^{\frac{-(\omega-2\pi f_c)^2}{4\alpha}} \right] * (R_{FS}\beta_{FS}\, e^{-j\omega\tau_{FS}} + R_{BW}\beta_{BW} e^{-j\omega\tau_{BW}}) \quad \text{.....(140)}$$

was compared to the FFT obtained using the same command in MATLAB to convert the time domain signal from a clean sample given by

$$S_{CL}(t) = R_{FS}\beta_{FS}\, e^{-\alpha(t-\tau_{FS})^2} \cos(2\pi f_c(t-\tau_{FS})) + R_{BW}\beta_{BW}\, e^{-\alpha(t-\tau_{BW})^2} \cos(2\pi f_c(t-\tau_{BW})) \text{..(141)}$$

The time domain signal given by eq.(141) is shown in Figure 61. This signal was converted to frequency domain and show in Figure 62 comparison. The FFTs are basically identical.

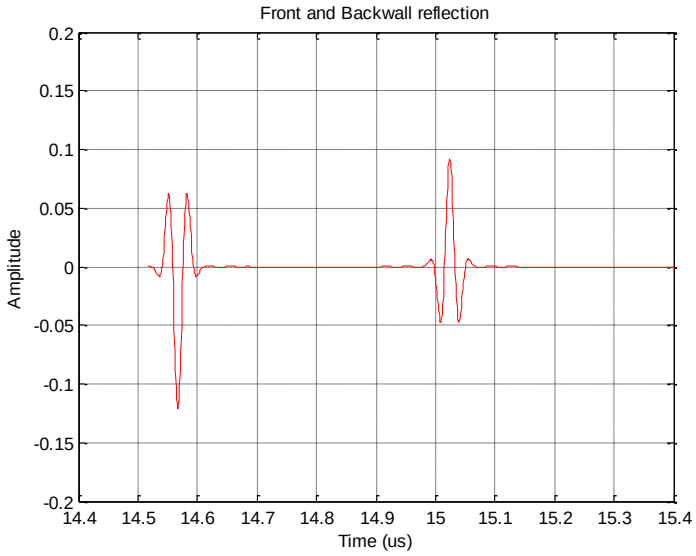


**Figure 61: Time Domain reflections for clean sample**

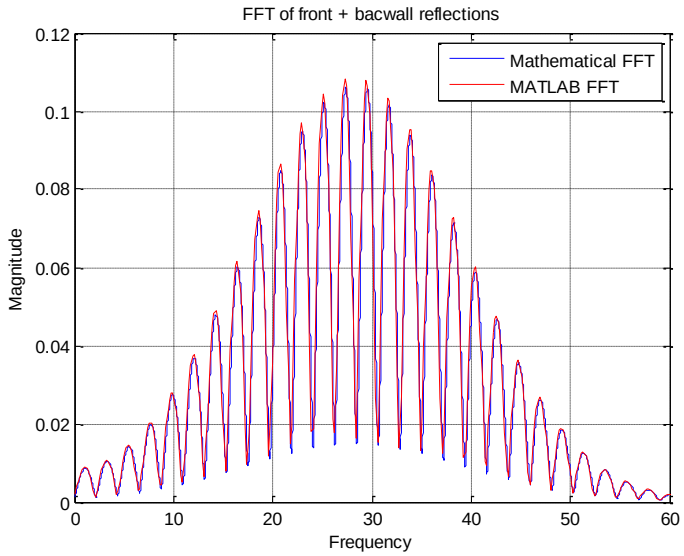


**Figure 62: Comparison of Mathematically computed FFT with MATLAB FFT**

## 5.2 Simulation Time Domain Ultrasonic Reflections

Based on the frequency response data analysis conducted in section 3.3, only a 250um particle case was considered for further evaluation in this research work. A 3-dimensional matrix was created to represent the various locations on the sample where data is collected. The depth was initially sliced into thickness of 250um which is the size of the particle. The occurrence of "1" in the array indicates the presence of the particle as shown in Figure 63. It is assumed that a particle is never present in the top and bottom layers of the sample. For a case where the sample is 1mm in total thickness, this array allowed for only four possible positions for particle placement in the model. This is illustrated in Figure 63.

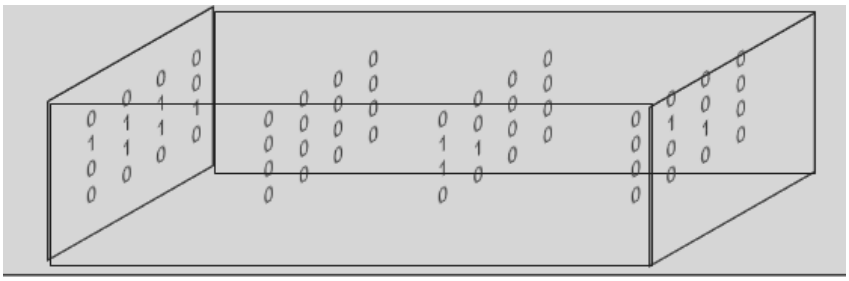

**Figure 63: Layer thickness is same as the particle size**

In order to have more flexibility in adjusting this position of the particle with finer depth resolution, the depth was sliced into thickness of 50um as shown in Figure 64. The occurrence of "1" for the first time in the array indicates the particle starts at that depth. The repeating of "1" 5 times represents the size of a 250um particle. If the particle is to be modeled as only 200um, the "1" is repeated 4 times. This allowed for adjusting

the particle depth by 50um and therefore, opening up the possibilities of placing the particle at various depths during modeling. It is also assumed that a particle is never present in the top and bottom layers of the sample.

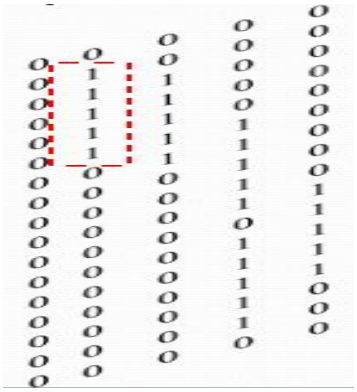

**Figure 64: Layer thickness is 5 times smaller than the particle size**

The purpose of having multiple arrays is to mimic various positions of the transducer on a sample in x (scan) and y (step) axes. The various layers represent the z (depth) in the sample.

A modeled signal without the presence of the particle in shown in Figure 65. A modeled signal with a particle present half way through the depth of the sample is shown in Figure 66 and a case where a particle is closer to the surface is shown in Figure 67.

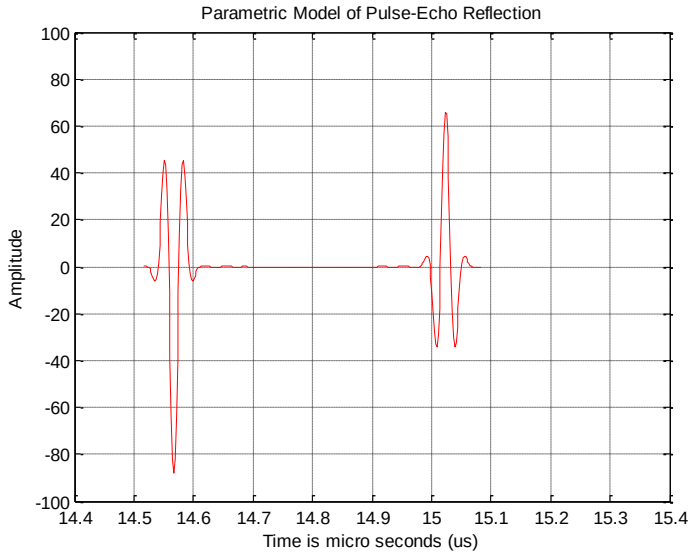


**Figure 65: Parametric model for reflections from clean sample**

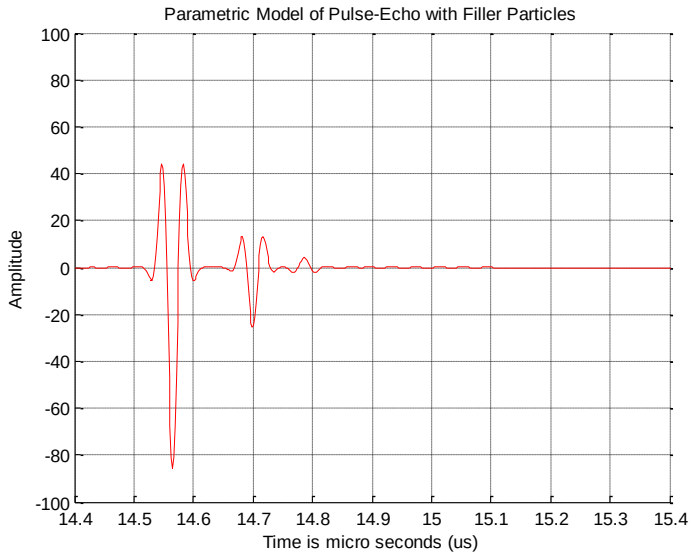


**Figure 66: Model signal with particle halfway through the depth**

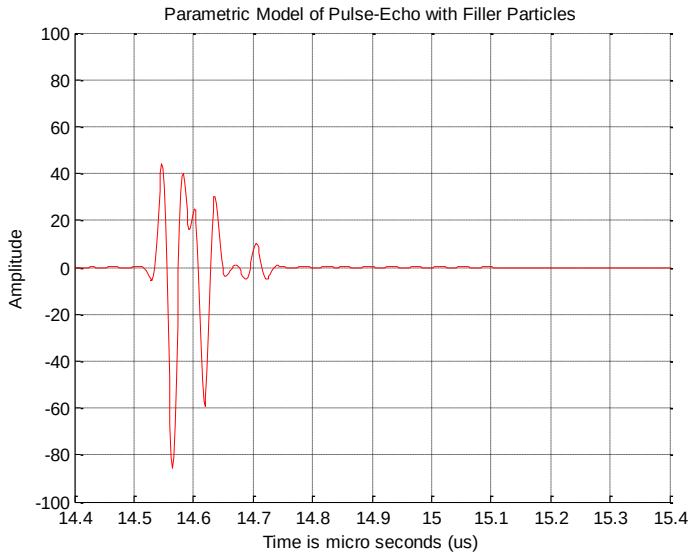


**Figure 67: Model signal with particle closer to the surface of the sample**

Using a matrix without any particles to create the ultrasonic reflections, the peak amplitude from the backwall was recorded at each x-y location to generate a simulated C-scan image from the backwall. This image is shown in Figure 68a. A similar matrix with four particles at different depths and x-y locations was modeled and the amplitudes from the backwall were recorded. The simulated C-scan obtained is shown in Figure 68b.

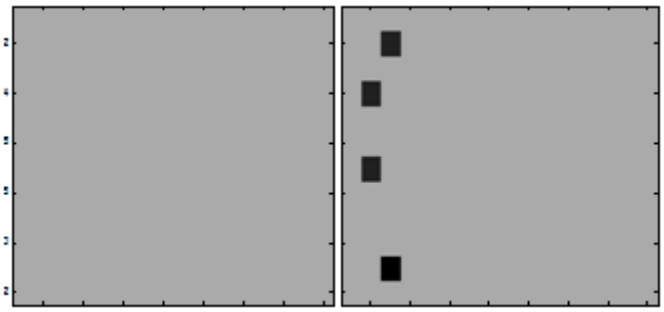

a) (b)

**Figure 68: (a) Modeled C-scan with no particles (b) Modeled C-scan with four particles in different locations**

## 5.3 Applying Transfer Function to Various Particle Scenarios

The transfer function based on the parametric model and a case with a particle closer to the bottom of the sample that is given by the array [0;0;0;0;0;0;0;0;0;0;1;1;1;1;1;0;0] was applied to a model case where the particle was in the middle of the bulk given by [0;0;0;0;1;1;1;1;1;0;0;0;0;0;0;0;0]. It should be noted in Figure 69 that the backwall reflection was restored to the expected amplitude with the expected shape and phase. This speaks to the robustness of the approach. This is important since one cannot predict at what depth the obstructing filler particles may be located.

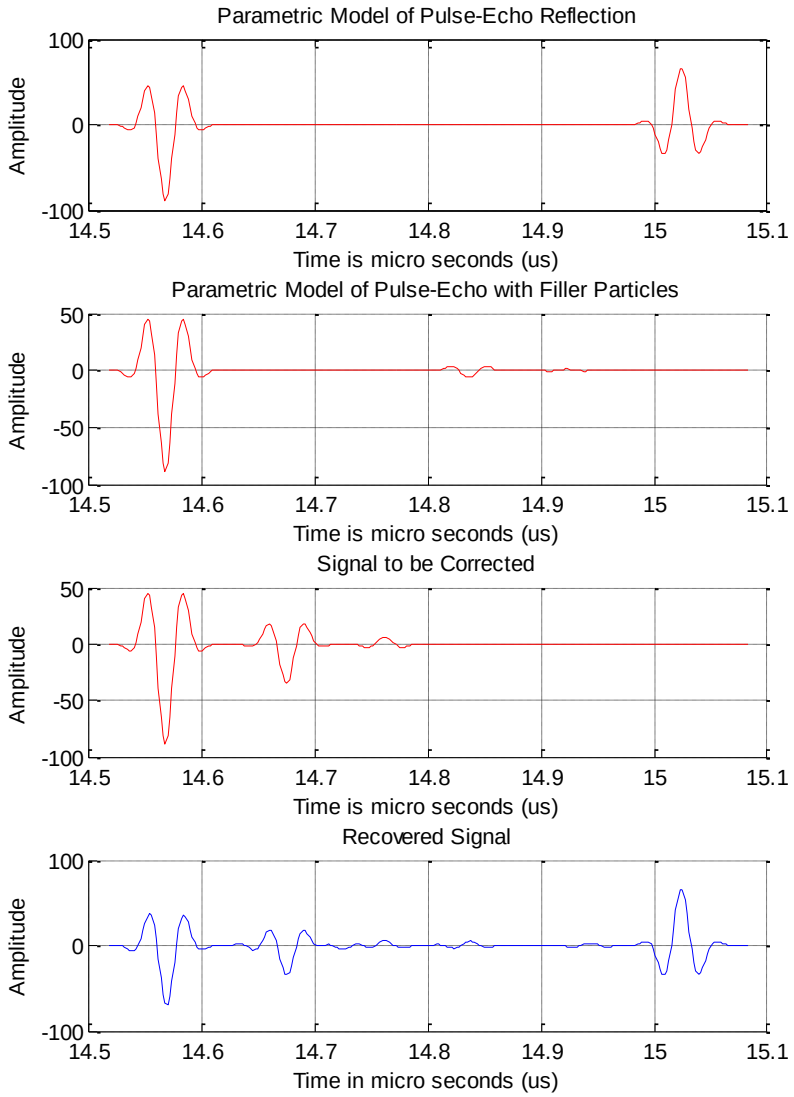


**Figure 69: Case where Transfer function based on particle close to the bottom applied to the signal with particle in the middle of the bulk to obtain a recovered signal where backwall is fully restored**

The transfer function based on the parametric model and a case with one particle close to the bottom of the sample and one close to the top of the sample represented by the array [0;0;1;1;1;1;1;0;0;0;1;1;1;1;1;0;0] was applied to a model case where the particle was in the middle of the bulk given by [0;0;0;0;1;1;1;1;1;0;0;0;0;0;0;0;0].

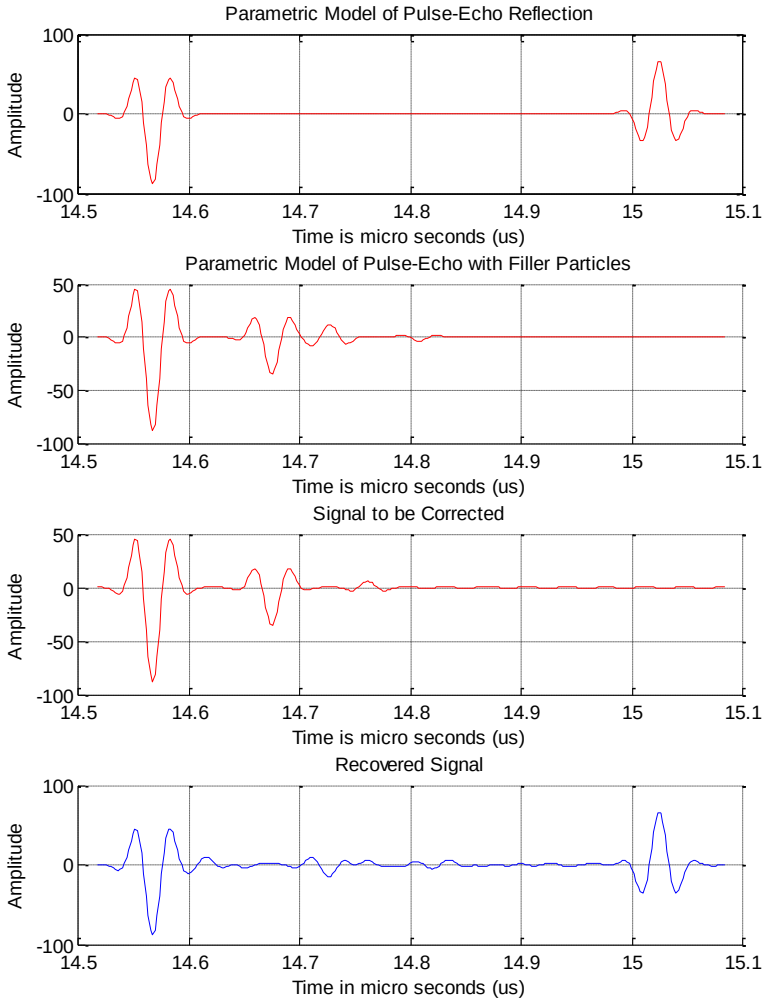


**Figure 70: Case where Transfer function based on one particle close to the top and one particle closer to the bottom applied to the signal with particle in the middle of the bulk to obtain a recovered signal where backwall is fully restored**

It should be noted in Figure 70 that the backwall reflection was restored to the expected amplitude with the expected shape and phase.

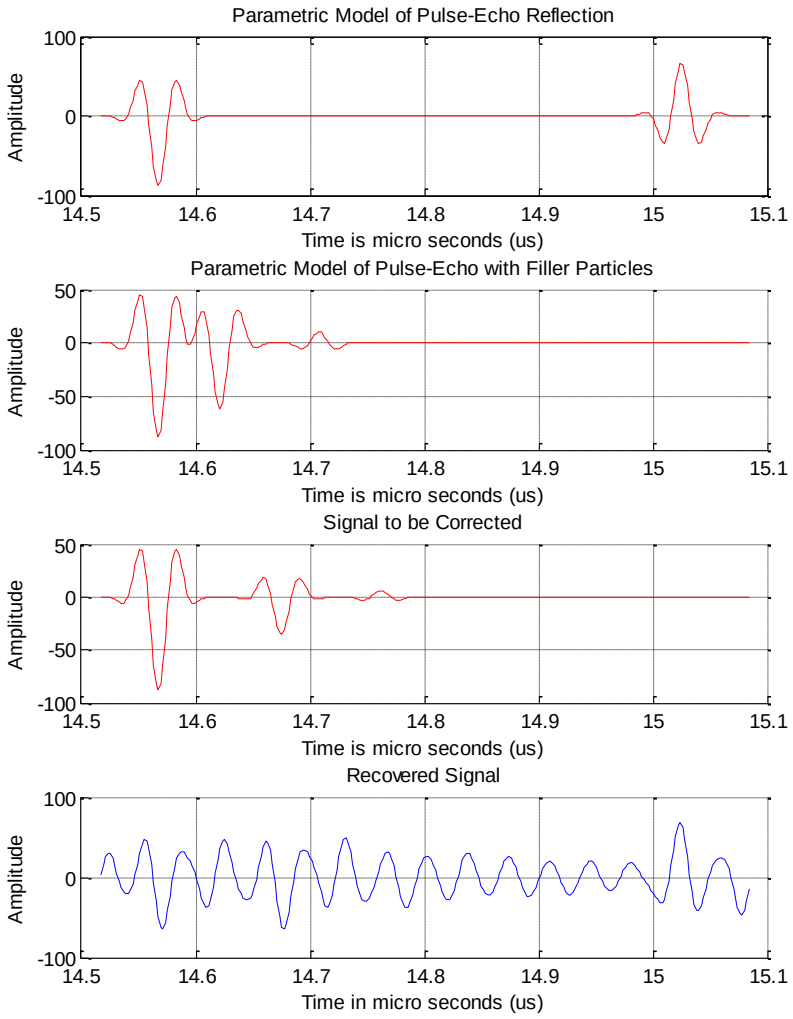


**Figure 71: Case where Transfer function based on a particle close to the top of the sample applied to the signal with particle in the middle of the bulk to obtain a recovered signal where the signal is noisy but backwall is restored**

The transfer function based on the parametric model and a case with a particle close to the top of the sample represented by the array [0;0;1;1;1;1;1;0;0;0;0;0;0;0;0;0;0] was applied to a model case where the particle was in the middle of the bulk given by [0;0;0;0;1;1;1;1;1;0;0;0;0;0;0;0;0].

It should be noted in Figure 71 that the backwall reflection was restored. However, the entire signal seemed to have a ringing effect with no clear distinction between the front surface reflection, particle locations and the backwall. This was most likely caused by the particle in the model used to create the transfer function being so close to the top that it caused an overlap between the front surface signal and the particle signal.

The error which is the difference in the restored signal backwall amplitude compared to the expected signal backwall amplitude based on transfer function generated on various particle positions have been calculated and plotted. It was noted that the error is zero when the particle in the model that is used to generate the transfer function is in the same position as that of the particle model it is applied to.

The resulting absolute error when a transfer function based on a particle close to the surface is applied to the various model particle cases is detailed in Table 5. The Mean Square Error (MSE) was computed to be 7.7506.

**Table 5: Error for Transfer function based on particle close to the surface**

| P.M B-W Amp | Time of BW occurrence | Model used for T.F | Model amp used for T.F | Model used to apply T.F | B.W Amplidute with Particles | Amplitude of Recovered Signal | Time of recovered B.W occurrence | Error | Sq(Error) |
|---|---|---|---|---|---|---|---|---|---|
| 65.67 | 15.0235 | [0;1;1;1;1;1;0;0;0;0;0;0;0;0;0;0;0] | 0.467 | [0;1;1;1;1;1;0;0;0;0;0;0;0;0;0;0;0] | 0.467 | 65.691 | 15.023 | 0.021 | 0.000441 |
| 65.67 | 15.0235 | [0;1;1;1;1;1;0;0;0;0;0;0;0;0;0;0;0] | 0.467 | [0;0;0;0;0;0;1;1;1;1;1;0;0;0;0;0;0] | 0.467 | 68.93 | 15.025 | 3.26 | 10.6276 |
| 65.67 | 15.0235 | [0;1;1;1;1;1;0;0;0;0;0;0;0;0;0;0;0] | 0.467 | [0;0;0;0;0;0;0;0;0;0;0;1;1;1;1;1;0] | 0.467 | 67.8545 | 15.023 | 2.1845 | 4.77204 |
| 65.67 | 15.0235 | [0;1;1;1;1;1;0;0;0;0;0;0;0;0;0;0;0] | 0.467 | [0;0;1;1;1;1;1;0;0;0;1;1;1;1;1;0;0] | 0.467 | 69.62 | 15.025 | 3.95 | 15.6025 |
| | | | | | | | | MSE | 7.750645 |

The absolute error for the four cases of particle positions that have been corrected are shown in Figure 72.

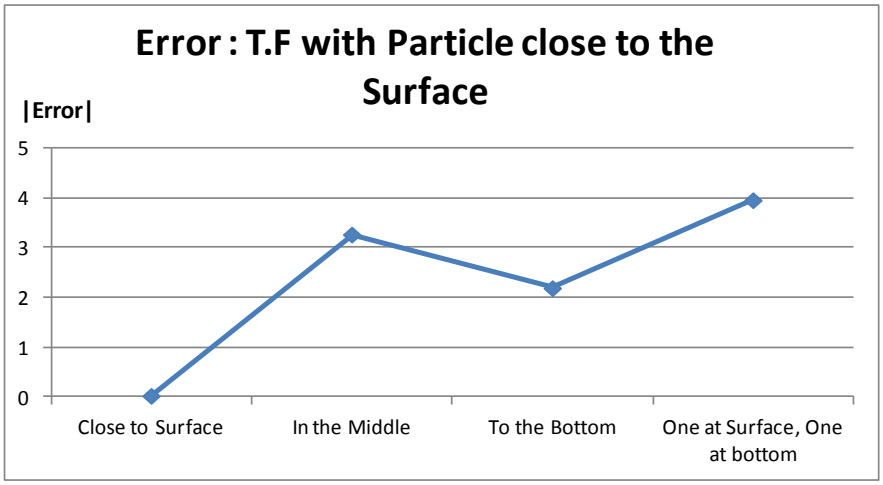


**Figure 72: Error when T.F based on particle close to the surface is applied to various particle models**

The error when a transfer function based on a particle in the middle is applied to the various modeled particle cases is shown in Table 6. The absolute error for the four cases of particle positions that have been corrected is shown in Figure 73. The MSE was computed to be 1.3747.

**Table 6: Error for Transfer Function based on particle in the middle**

| P.M B-W Amp | Time of BW occurrence | Model used for T.F | Model amp used for T.F | Model used to apply T.F | B.W Amplidute with Particles | Amplitude of Recovered Signal | Time of recovered B.W occurrence | Error | Sq(Error) |
|---|---|---|---|---|---|---|---|---|---|
| 65.67 | 15.0235 | [0;0;0;0;0;0;1;1;1;1;1;0;0;0;0;0;0] | 0.467 | [0;1;1;1;1;1;1;0;0;0;0;0;0;0;0;0;0] | 0.467 | 67.5 | 15.023 | 1.83 | 3.3489 |
| 65.67 | 15.0235 | [0;0;0;0;0;0;1;1;1;1;1;0;0;0;0;0;0] | 0.467 | [0;0;0;0;0;0;1;1;1;1;1;0;0;0;0;0;0] | 0.467 | 65.691 | 15.023 | 0.021 | 0.000441 |
| 65.67 | 15.0235 | [0;0;0;0;0;0;1;1;1;1;1;0;0;0;0;0;0] | 0.467 | [0;0;0;0;0;0;0;0;0;0;0;1;1;1;1;1;0] | 0.467 | 67.0347 | 15.023 | 1.3647 | 1.862406 |
| 65.67 | 15.0235 | [0;0;0;0;0;0;1;1;1;1;1;0;0;0;0;0;0] | 0.467 | [0;0;1;1;1;1;1;0;0;0;1;1;1;1;1;0;0] | 0.467 | 66.206 | 15.023 | 0.536 | 0.287296 |
| | | | | | | | | MSE | 1.374761 |

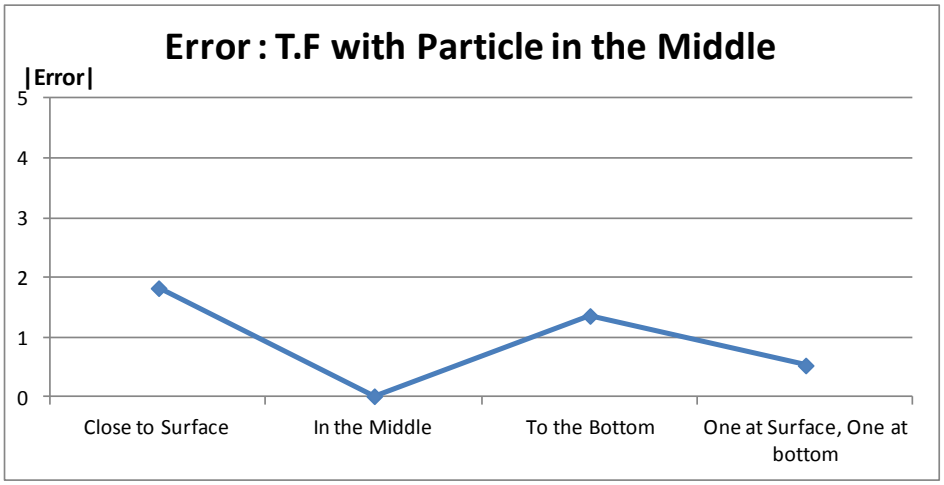


**Figure 73: Error when T.F based on particle in the middle is applied to various particle models**

The error when a transfer function based on a particle close to the bottom is applied to the various modeled particle cases is shown in Table 7. The absolute error for the four cases of particle positions that have been corrected are shown in Figure 74. The MSE was computed to be 1.5900.

**Table 7: Error for Transfer Function based on particle at the bottom**

| P.M B-W Amp | Time of BW occurrence | Model used for T.F | Model amp used for T.F | Model used to apply T.F | B.W Amplidute with Particles | Amplitude of Recovered Signal | Time of recovered B.W occurrence | Error | Sq(Error) |
|---|---|---|---|---|---|---|---|---|---|
| 65.67 | 15.0235 | [0;0;0;0;0;0;0;0;0;0;1;1;1;1;1;0] | 0.467 | [0;1;1;1;1;1;0;0;0;0;0;0;0;0;0;0] | 0.467 | 67.91 | 15.023 | 2.24 | 5.0176 |
| 65.67 | 15.0235 | [0;0;0;0;0;0;0;0;0;0;1;1;1;1;1;0] | 0.467 | [0;0;0;0;0;0;1;1;1;1;1;0;0;0;0;0] | 0.467 | 66.8 | 15.023 | 1.13 | 1.2769 |
| 65.67 | 15.0235 | [0;0;0;0;0;0;0;0;0;0;1;1;1;1;1;0] | 0.467 | [0;0;0;0;0;0;0;0;0;0;0;1;1;1;1;1;0] | 0.467 | 65.6916 | 15.023 | 0.0216 | 0.0004666 |
| 65.67 | 15.0235 | [0;0;0;0;0;0;0;0;0;0;1;1;1;1;1;0] | 0.467 | [0;0;1;1;1;1;1;0;0;0;1;1;1;1;1;0;0] | 0.467 | 65.9255 | 15.023 | 0.2555 | 0.0652802 |
| | | | | | | | | MSE | 1.5900617 |

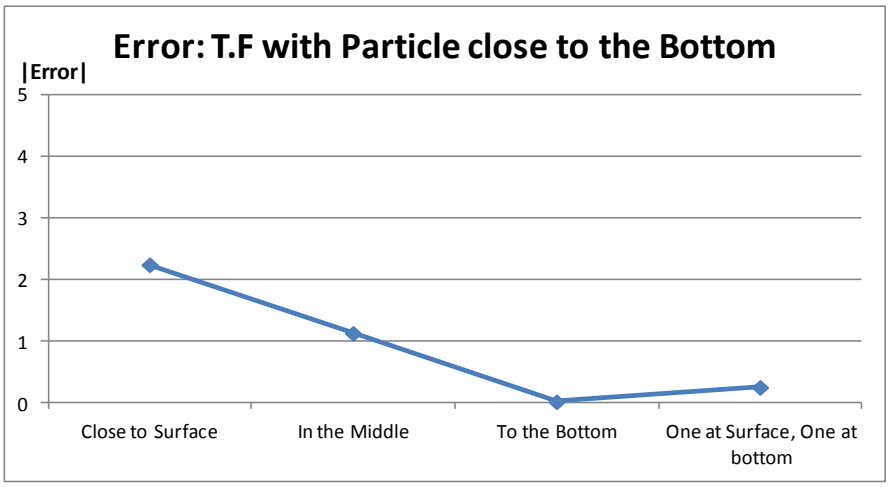


**Figure 74: Error when T.F based on particle close to the bottom is applied to various particle models**

The error when a transfer function based on one particle close to the surface and one particle close to the bottom is applied to the various modeled particle cases is shown in Table 5. The absolute error for the four cases of particle positions that have been corrected are shown in Figure 75. The MSE was computed to be 2.3668.

**Table 8: Error for Transfer Function based on one particle close to the top and the other close to the bottom**

| P.M B-W Amp | Time of BW occurrence | Model used for T.F | Model amp used for T.F | Model used to apply T.F | B.W Amplidute with Particles | Amplitude of Recovered Signal | Time of recovered B.W occurrence | Error | Sq(Error) |
|---|---|---|---|---|---|---|---|---|---|
| 65.67 | 15.0235 | [0;0;1;1;1;1;1;0;0;0;1;1;1;1;1;0;0] | 0.467 | [0;1;1;1;1;1;0;0;0;0;0;0;0;0;0;0;0] | 0.467 | 64.46 | 15.051 | 1.21 | 1.4641 |
| 65.67 | 15.0235 | [0;0;1;1;1;1;1;0;0;0;1;1;1;1;1;0;0] | 0.467 | [0;0;0;0;0;0;1;1;1;1;1;0;0;0;0;0;0] | 0.467 | 62.915 | 15.023 | 2.755 | 7.590025 |
| 65.67 | 15.0235 | [0;0;1;1;1;1;1;0;0;0;1;1;1;1;1;0;0] | 0.467 | [0;0;0;0;0;0;0;0;0;0;0;1;1;1;1;1;0] | 0.467 | 65.0274 | 15.023 | 0.6426 | 0.4129348 |
| 65.67 | 15.0235 | [0;0;1;1;1;1;1;0;0;0;1;1;1;1;1;0;0] | 0.467 | [0;0;1;1;1;1;1;0;0;0;1;1;1;1;1;0;0] | 0.467 | 65.6916 | 15.023 | 0.0216 | 0.0004666 |
| | | | | | | | | MSE | 2.3668816 |

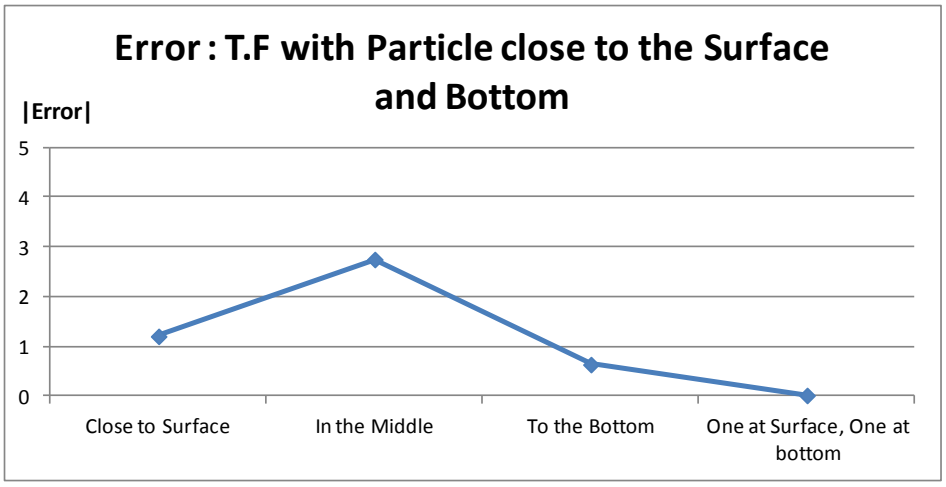


**Figure 75: Error when T.F based on one particle close to the surface and one close to the bottom is applied to various particle models**

The mean square error (MSE) computed for each transfer function is show in Figure 76. The transfer function generated based on the particle in the middle has the lowest MSE.

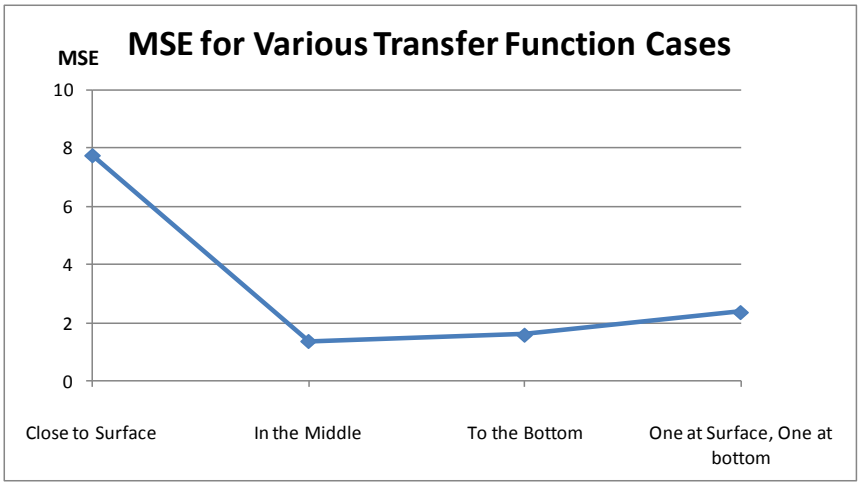


**Figure 76: Mean Square error for various transfer function cases**

This transfer function is applied to various modeled C-scans and real C-scans discussed hereafter in this dissertation. A modeled C-scan with particles at various depths is shown in Figure 77a and the recovered C-scan is shown in Figure 77b. The effect of modeled filler particles is mitigated as seen in this figure.

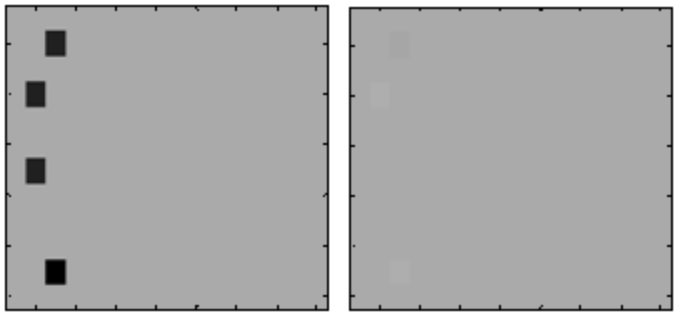

(a) (b)

**Figure 77: (a) Modeled C-scan with filler particles (b) Recovered modeled C-scan**

The contrast ratio between the background and a particle location was computed on the modeled image and recovered imaged. This is shown in Table 9. It is desired to have the contrast ratio of 1. From the Table 9, it can be noted that for all modeled particle locations, the contrast ratio in the recovered image is in the range of 0.958-1.003.

**Table 9: Contrast Ratio in Modeled C-scan Image**

| Particle Location in Depth | Pixel Intensity (Before) | Pixel Intensity (After) | Background Intensity | Contrast Ratio (Before) | Contrast Ratio (After) |
|---|---|---|---|---|---|
| Middle | 0.1933 | 65.4397 | 65.6916 | 339.8427315 | 1.003849345 |
| Top | 0.1933 | 68.5111 | 65.6916 | 339.8427315 | 0.958846085 |
| Bottom | 0.1947 | 66.0339 | 65.6916 | 337.3990755 | 0.994816299 |
| Top and Bottom | 3.2277E-06 | 67.2687 | 65.6916 | 20352449.11 | 0.976555218 |

# CHAPTER 6: RESULTS FOR A REAL SAMPLE STRUCTURE

Since the transfer function approach showed promising results with simulated data, the performance of this approach on a real case was evaluated.

## 6.1 Clean Resin Sample

First, a sample was made with resin material of 800um thickness. This sample is shown in Figure 78a along with the thickness measured using Vernier Caliper in Figure 78 b.

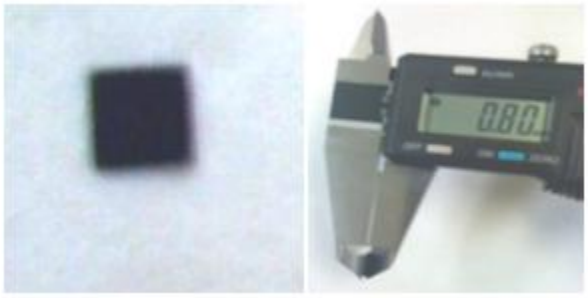


**(a)** **(b)**

**Figure 78: (a) Clean Resin Sample (b) Measurement of Clean Resin Sample**

The 75MHz 12mm focal length transducer was used to obtain the backwall reflection from this sample. The transducer was focused on the backwall reflection. The reflection signal measured by the transducer is shown in Figure 79.

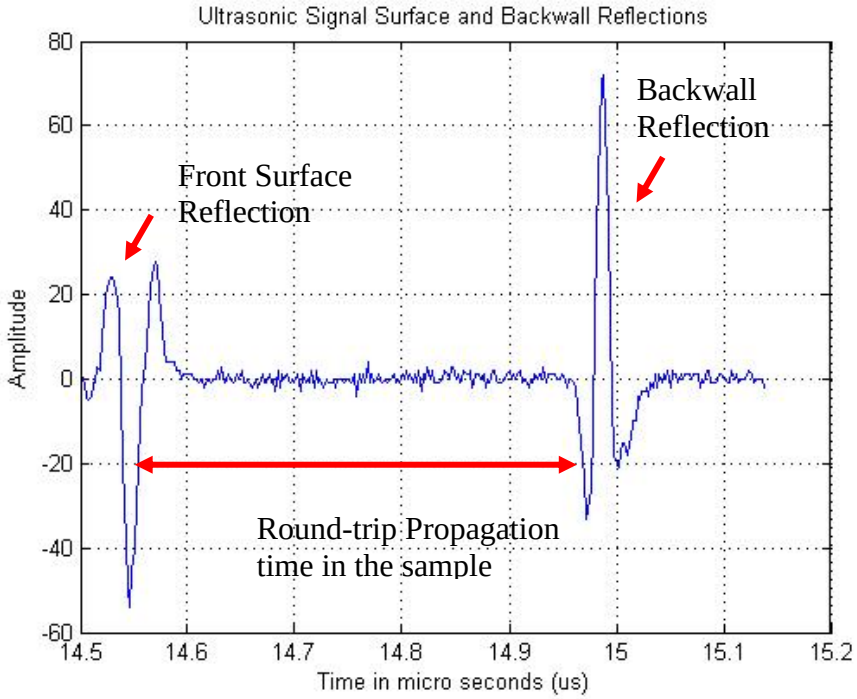


**Figure 79: Ultrasonic A-scan for the Clean Resin Sample**

The purpose of obtaining the reflection from the clean resin sample is to be able to compare it to the signal from one of the parametric models discussed so far. Adjustments to the selected model will then be made to get a very close match between the two signals. The resulting model will be the parametric model that will be used in this research study. Also, the thickness (D) of the clean resin sample was measured to be

800um and the round-tip propagation time (T) from the surface of the sample to the backwall in Figure 79 was noted to 0.43 micro-seconds (us). Therefore, the acoustic material velocity (V) of resin can be calculated as

$$D = V * T / 2 \quad \text{.....(142)}$$

$$V = 2 * D / T \quad \text{.....(143)}$$

$$V = 2 * 0.8 / (14.98 - 14.55) \quad \text{.....(144)}$$

$$V = 3.721 mm / us \quad \text{.....(145)}$$

A total of five measurements were taken on the sample and tabulated as shown in Table 10. The mean value is 3.721mm/us and the standard deviation is 0.0063.

**Table 10: Material Velocity**

| Thickness (mm) | Propagation Time (us) | Acoustic Velocity (mm/us) |
|---|---|---|
| **0.8** | **0.43** | **3.721** |
| **0.8** | **0.424** | **3.732** |
| **0.8** | **0.4301** | **3.72** |
| **0.8** | **0.4303** | **3.718** |
| **0.8** | **0.4305** | **3.7158** |
| | **MEAN** | **3.721** |
| | **STANDARD DEVIATION** | **0.0063** |

The value of 3.721mm/us for material velocity was used for all the experimental work discussed in this dissertation.

The sample was imaged using the setup shown in Figure 3 of Chapter 2. The resulting C-scan image from the backwall of the sample is shown in Figure 80.

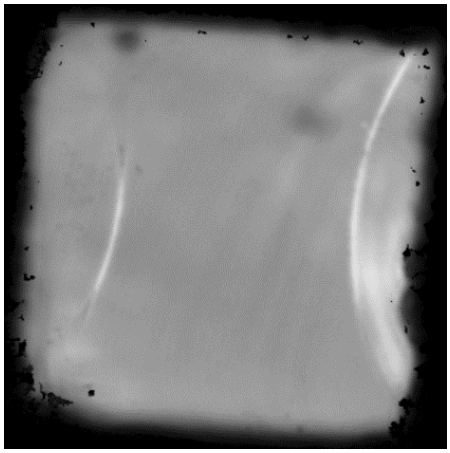

**Figure 80: C-scan image from the backwall of clean resin sample**

The model was developed in MATLAB and the resulting Ultrasonic pulse-echo reflections from the front surface of the Resin material and the backwall reflections are shown in Figure 81.

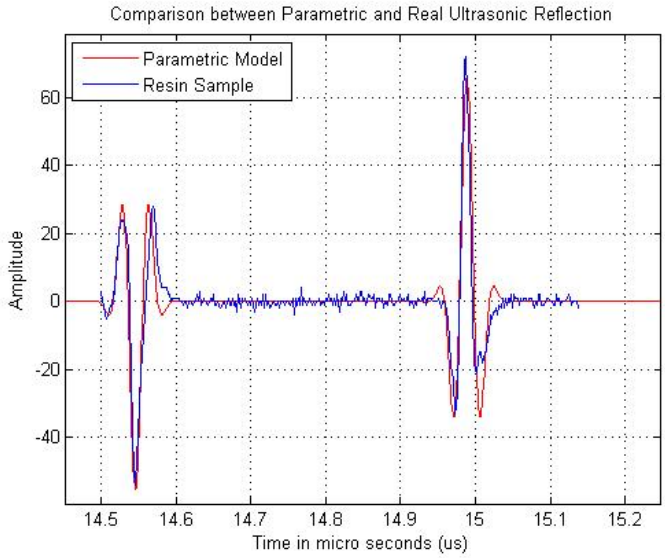


**Figure 81: Comparison between Parametric Model and Real Data**

The reflections from the parametric model were overlapped with the reflections from the real sample and shown in Figure 81.

The correlation between the parametric model and real data was computed both at the front surface as well as the backwall. There was a 95% correlation at the front surface and a 93% correlation at the backwall interface, thus confirming that the model is robust. The result is shown in Figure 82.

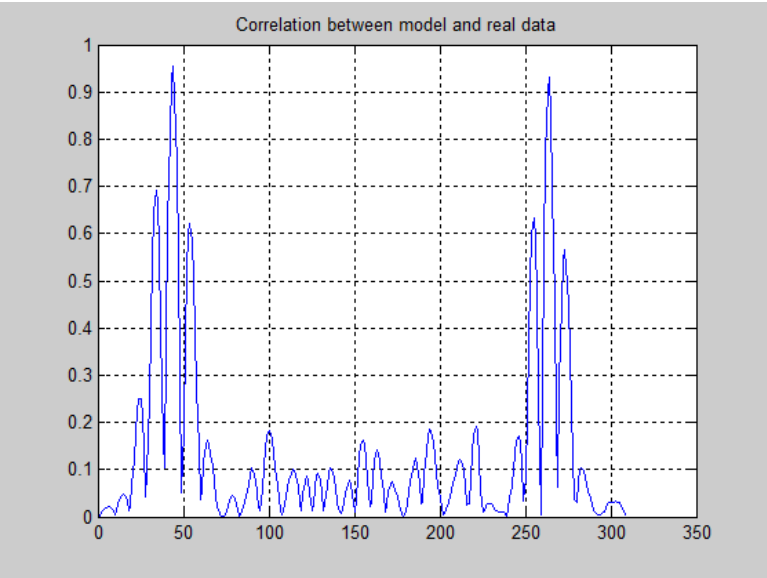


**Figure 82: Correlation between Parametric model and Real signal**

## 6.2 Resin Sample with Filler Particles

It is important to understand the effect of filler particles on an Ultrasonic Pulse-Echo reflection in order to mitigate or remove the effect. The scattering caused by the filler particles is referred to as noise. Once again, a sample similar to the clean resin sample was made. However, filler particles were mixed into the resin material before

curing it. Glass beads within the size range of 150um-250um were chosen as the filler particles and an optical microscopic image of these beads is shown in Figure 83.

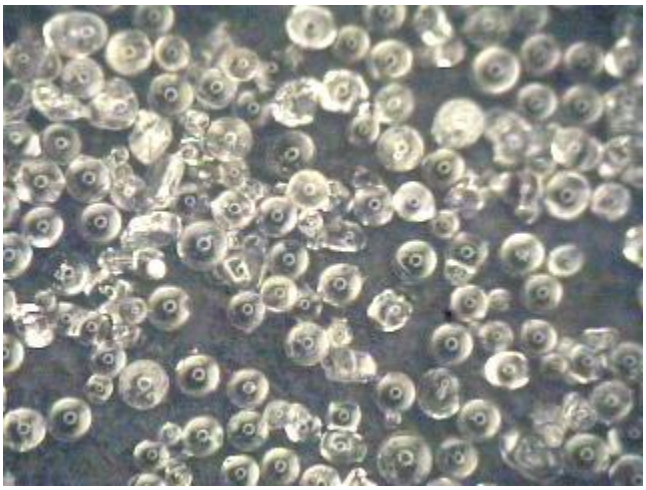

**Figure 83: Glass Beads in the range of 150um-250um used as Filler Particles**

A sample was made and the sample was scanned using a 75MHz 12mm transducer to obtain the backwall reflection and also to capture the effect of the filler particles on the Ultrasonic signal. This A-scan is shown in Figure 84. It should be noted that the signal is corrupted due to the signal scattering caused by the filler particles. The additional signals noted by green ellipses in Figure 84 are referred to as Noise. After studying the A-scans, it seemed like the particles settled closer to the bottom of the sample during the curing process.

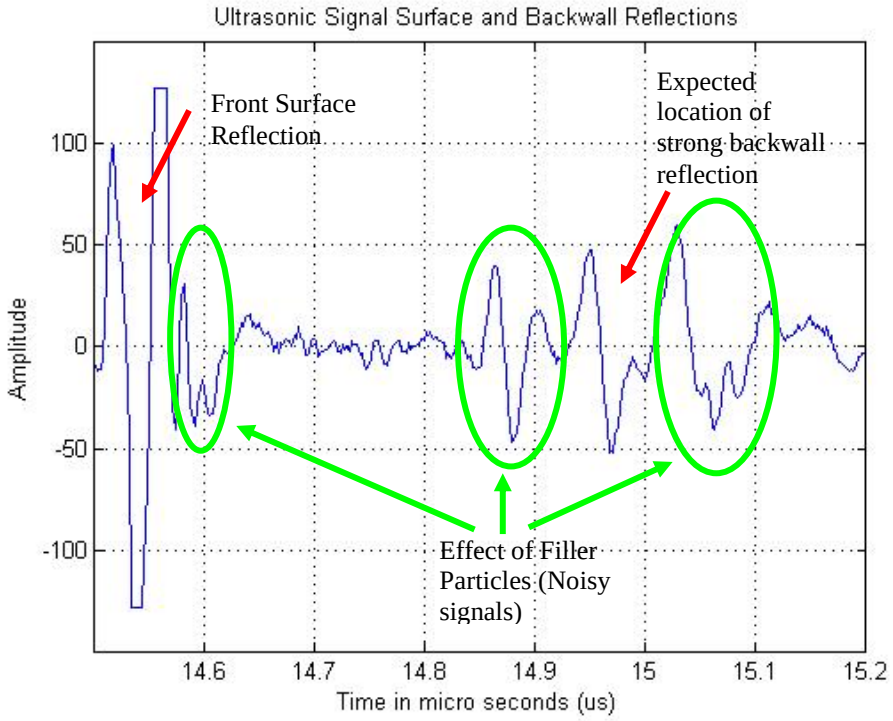


**Figure 84: Amplified Reflection from a Resin Sample with Dense Filler Particles**

The sample with filler particles was scanned using the setup shown in Figure 3 in Chapter 2. The resulting image is shown in Figure 85. The arrows indicate the shadow effects noted due to the presence of the filler particles. The white spots noted in the image are caused by voids/air pockets. These are defects and imaging these defects is desirable.

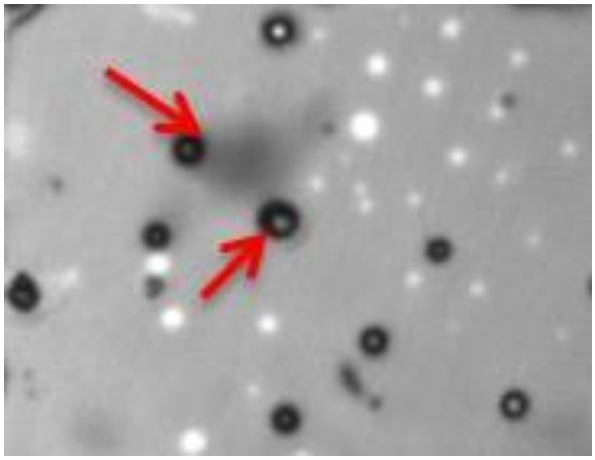

**Figure 85: C-scan image of a resin sample with filler particles**

## 6.3 Applying Transfer Function to Signals from the Real Sample

The real signal from a sample that has filler particles is represented as y(t). This signal is converted to the frequency domain as Y(jω). The transform of the uncorrupted signal is computed as

$$X(j\omega) = \frac{Y(j\omega)}{N(j\omega)} \quad \text{.....(145)}$$

X(jω) is converted into the time domain signal x(t), which is the expected uncorrupted signal from the backwall of the sample. The transfer function was applied to signals from a real sample where filler particles are known to be present. A model with a particle in the middle of the sample given by the array [0;0;0;0;0;1;1;1;1;1;0;0;0;0;0;0;0] shown in Figure 86 was used to create a transfer function as shown in Figure 87. This transfer function was applied to a real signal from the sample as shown in Figure 85. The

recovered signal is shown in Figure 89 where the backwall reflection is completely restored.

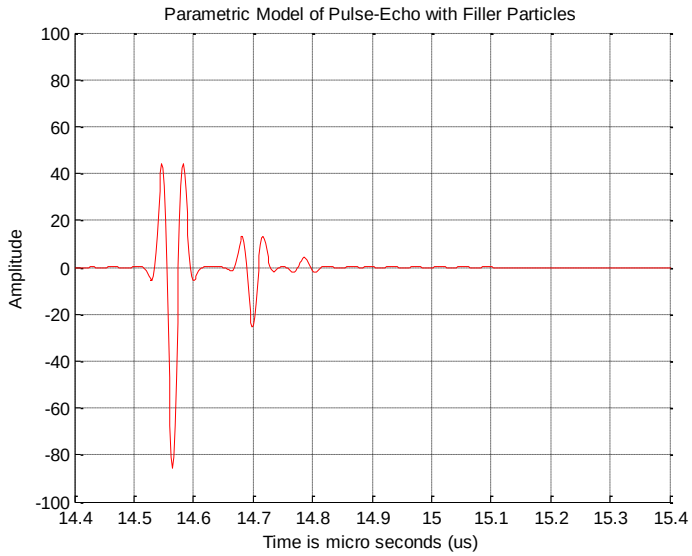


**Figure 86: Modeled particle signal with particle closer in the middle**

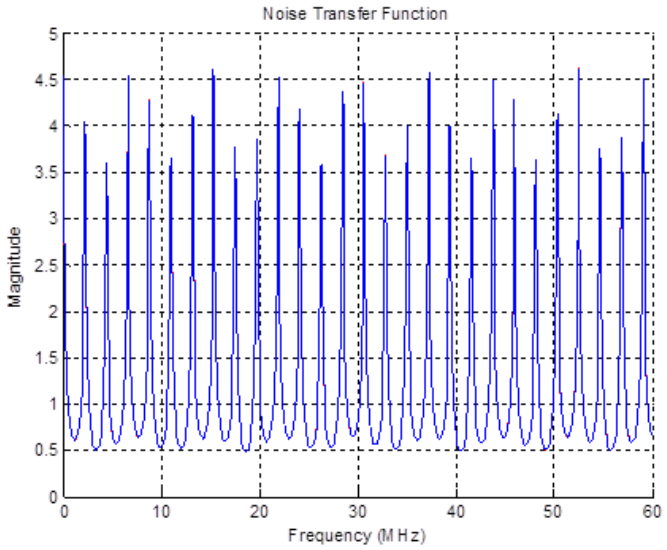


**Figure 87: Transfer function based on the modeled particle signal with particle in the middle**

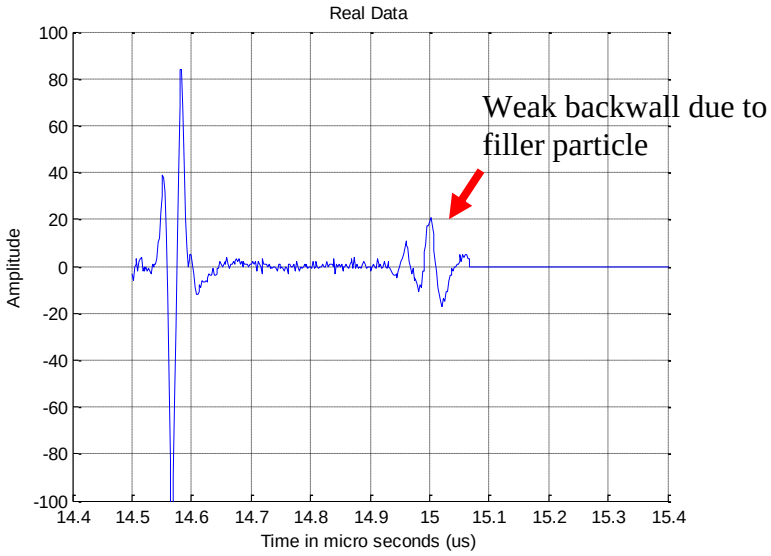


**Figure 88: Real Signal from a sample with filler particles**

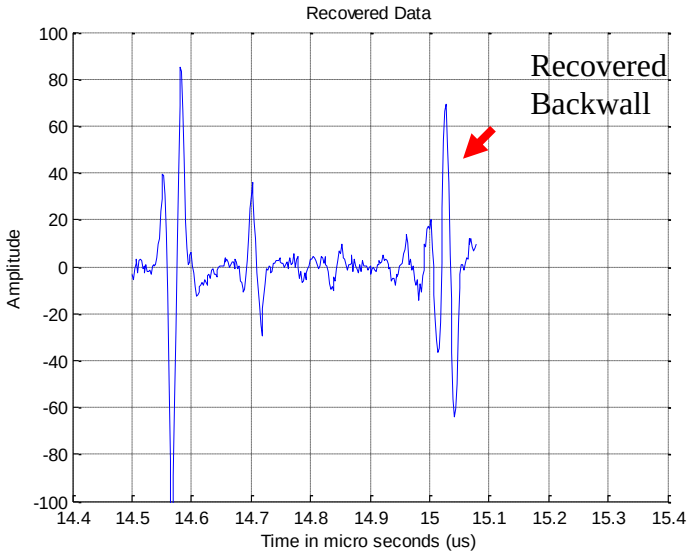


**Figure 89: Restored signal after applying the transfer function**

## 6.4 Transfer Function Applied To Entire Image

The transfer function generated based on the particle in the middle was applied to the entire data set in a real image. Figure 90a shows the original image, Figure 90b shows the corrected image where a transfer function was created based on one 250um particle in the middle. The effect of filler particles was mitigated. Most of the bright spots in the image which are voids are still visible. However, some of the really small voids were not noticeable in the recovered image anymore. A gray scale variation was noted from the bottom left corner to the top right corner of the image.

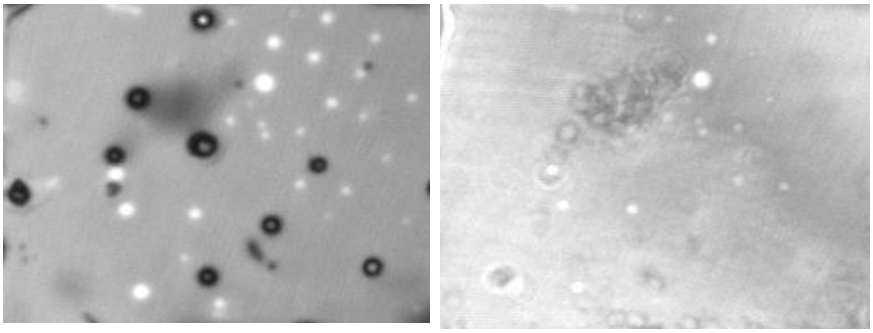

(a) (b)

**Figure 90: (a) Original Image (b) Corrected Image**

Also, the gray scale variation from the bottom left to the top right noted in the corrected image in Figure 90b was of particular interest. Therefore, A-scans from the sample were studied from two different locations on the sample. One from the middle right corner and one from the bottom left corner. The signals from these two locations were overlapped on top of the expected parametric model signal as shown in Figure 91a and Figure 91b. The transfer function was developed based on the thickness measured in the A-scan shown in Figure 91a. This transfer function was applied to the A-scan case shown in Figure 91b and the corrected signal is shown in Figure 91c. It can be seen that when the transfer function is applied to a case where the backwall is not aligned, the corrected signal has a higher amplitude than expected.

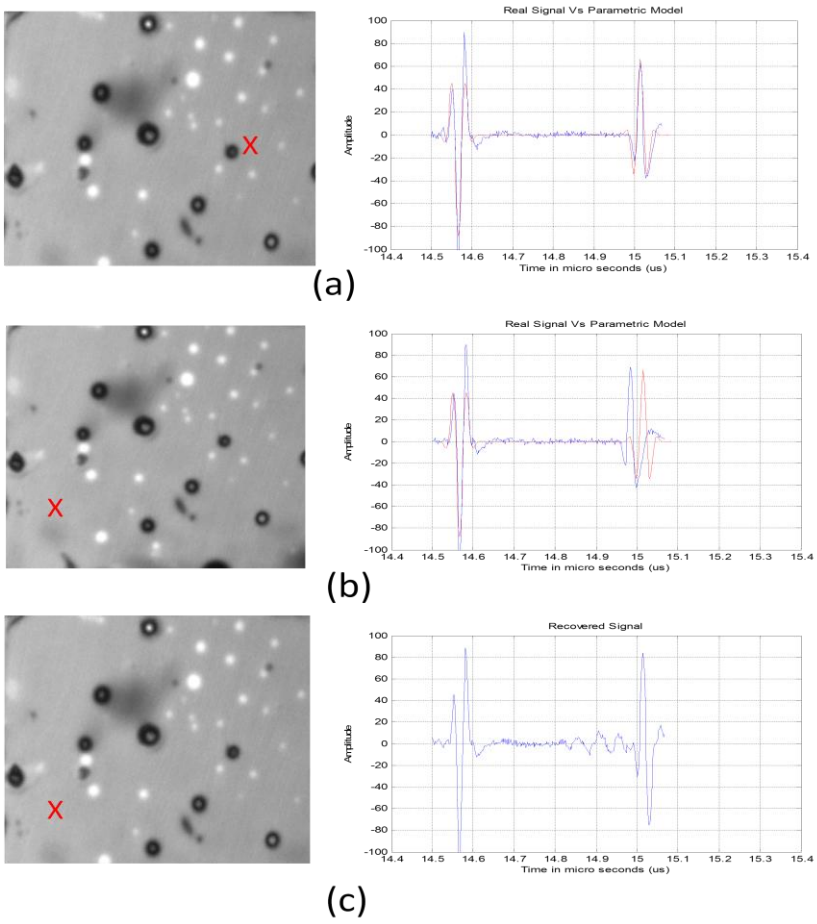


**Figure 91: (a) Case where A-scan from the selected location matches the parametric model (b) Case where A-scan from the selected location does not match the parametric model. (c) Corrected signal from the selected location indicating increase in amplitude**

In Figure 92a, the C-scan with a green line indicating the cross-section position is shown. The corresponding B-scan along the green line on the sample is shown in Figure 92b. It can be seen that the backwall is at an angle instead of a straight line, thus confirming the thickness variation from one corner of the sample to the other. Based on this, it was concluded that the transfer function's performance is sensitive to the thickness variation of the material.

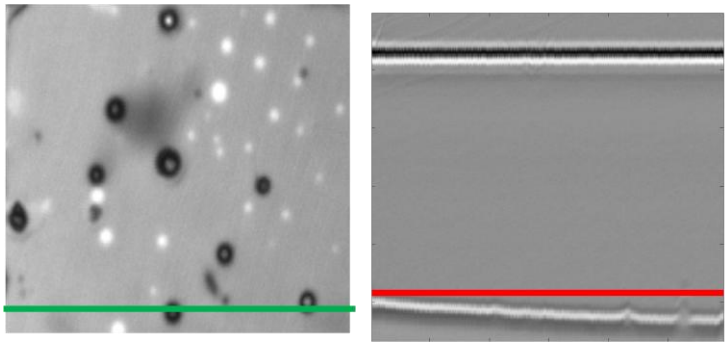

(a) (b)

**Figure 92: (a) C-scan with green line indicating cross-section position (b) B-scan along the green line showing warping indicated by the red line**

An alternative selective correction method is discussed in the next section where the correction is performed only when a particle is detected in the propagation path of the ultrasound.

## 6.5 Selective Correction: Applying Transfer Function Based on Threshold & Particle Presence

A program was written to apply the Transfer function based on the backwall amplitude and the presence of the particle in the bulk of the material. The program reads the A-scan data from an x-y location. The backwall amplitude is measured and if this amplitude is greater than 40%, the original amplitude is recorded and no correction to the signal is made. If the amplitude is less than 40%, the program checks to see if this reduction in amplitude is due to a pattern on the backwall or if it is due to an obstruction by a particle in the bulk. If a peak in the bulk is detected that has an amplitude greater than 10%, then a correction is made to the signal at that x-y location. The corrected amplitude is recorded. If any peaks detected in the bulk have an amplitude less than 10%, no correction is made and the original amplitude is recorded. Once the program completes this process for every single x-y location, all the amplitude data that was recorded is used to reconstruct the C-scan image.

The flowchart in Figure 93 gives some insight into how a correction to a signal is made based on selected criteria.

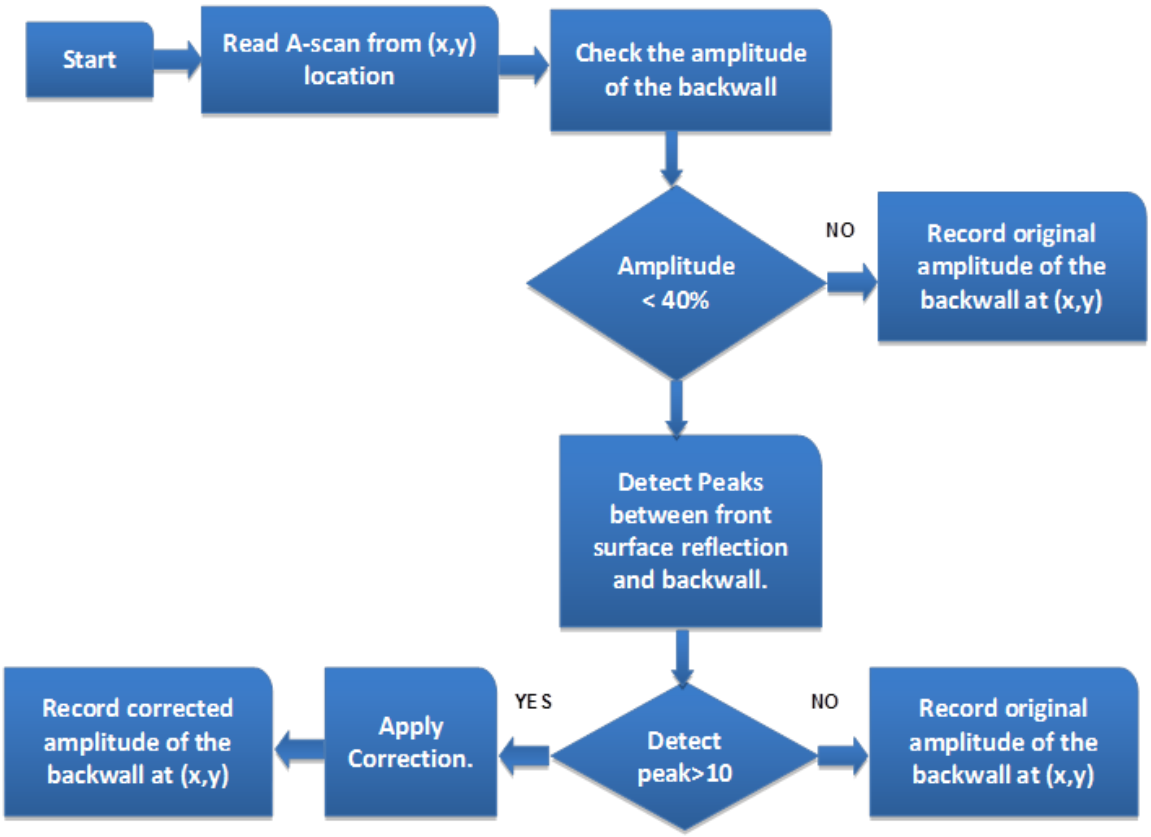


**Figure 93: Flowchart for Selective Correction based on presence of a particle**

The original image from the sample with resin particles is again shown in Figure 94a and the shadows due to the filler particles have been indicated with the red arrows. The selective correction technique was applied on the image. The transfer function was based on modeling the particle in the middle. The resulting image is shown in Figure 94b. The shadow effects caused by the filler particles have been mitigated and there is no brightness variation from left to right.

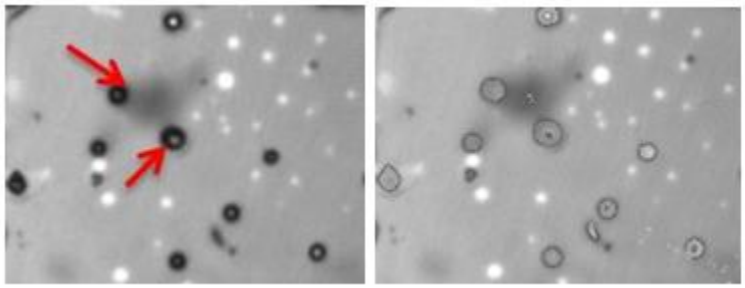

**(a)** **(b)**

**Figure 94: (a) Backwall image of resin sample with fillers (b) Recovered image**

The contrast ratio was computed on 10 different particle locations before and after the transfer function was applied. This can be seen in Table 11. The contrast ratio before correction is in the range of 2.1-4.35. The contrast ratio after correction is in the range of 0.96-1.013. While it is clear that there is improvement in areas where there are shadow effects due to filler particles, there is still a ring noted around the corrected area. This is discussed in the section 7.3. on future work.

**Table 11: Contrast Ratio on a C-scan image of a real image from an unpatterned sample**

| Particle No. | Pixel Intensity (Before) | Pixel Intensity (After) | Background Intensity | Contrast Ratio (Before) | Contrast Ratio (After) |
|---|---|---|---|---|---|
| 1 | 21 | 74.5261 | 74 | 3.523809524 | 0.992940728 |
| 2 | 32 | 70.80771 | 68 | 2.125 | 0.960347397 |
| 3 | 31 | 72.0335 | 73 | 2.35483871 | 1.013417368 |
| 4 | 17 | 75.9434 | 74 | 4.352941176 | 0.974409889 |
| 5 | 29 | 74.7054 | 69 | 2.379310345 | 0.923628011 |
| 6 | 38 | 76.4062 | 65 | 1.710526316 | 0.850716303 |
| 7 | 22 | 73.9387 | 67 | 3.045454545 | 0.906156045 |
| 8 | 38 | 72.5904 | 69 | 1.815789474 | 0.950538914 |
| 9 | 23 | 72.7563 | 69 | 3 | 0.948371481 |
| 10 | 23 | 73.6178 | 63 | 2.739130435 | 0.855771294 |
| | | | Mean | 2.704680052 | 0.937629743 |
| | | | Std. Deviation | 0.812063029 | 0.05137642 |

## 6.6 Applying Transfer Function to Entire Patterned Backwall Sample

It is important to test out the transfer function technique on a sample that has a pattern on the backwall. Therefore, a sample was created with Aluminum substrate with two rectangular pieces of tape stuck on the substrate. Then, resin material was added on top and particles were mixed into it before curing. The resin was sanded to make it smooth and of uniform thickness. The sample was imaged using a 75MHz transducer and the C-scan image was obtained.

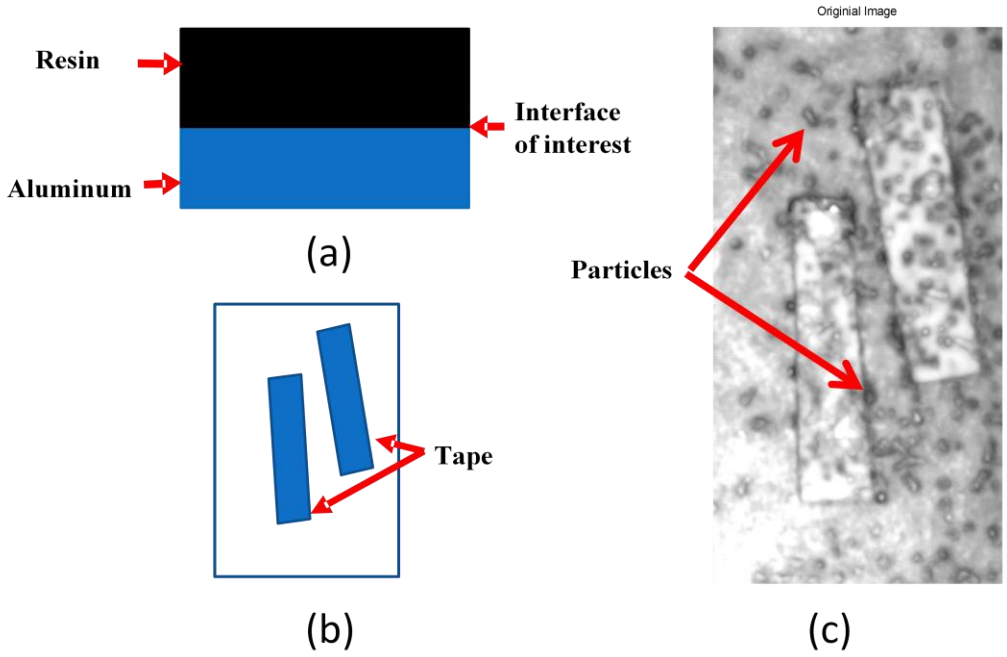


**Figure 95: (a) Side view sketch of the sample (b) top view sketch of the sample (c) C-scan image of the sample**

The side view and top view of the sample along with the C-scan image are shown in Figure 95a, Figure 95b and Figure 95c respectively. A couple of cases where shadows caused by the presence of the filler particles have been indicated in the C-scan image using red arrows in Figure 95c.

A location on the sample was picked to capture the A-scan. This location is shown in Figure 96a. The thickness was noted to be 855um. The model was matched taking this thickness into account and the same particle location was used as in the previous case to generate a transfer function. This was applied to the entire image and the recovered image is shown in Figure 96b.The pattern from the edges of the tape in some areas is still visible as indicated with green arrows in the image. Also, it was noted that the effect of the particles was mitigated. A gray scale variation was noted in the recovered image.

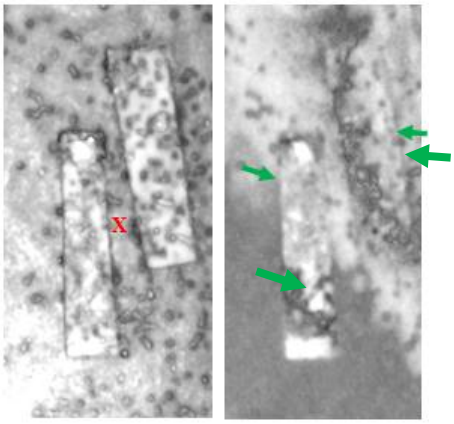


(a) (b)

**Figure 96: (a) Original image with location where thickness for parametric model was measured to be 855um (b) corrected image using 855um resin thickness**

A B-scan was performed on the sample to understand the variation in the thickness of the resin as this was not expected. It can be noted from the B-scans shown in Figure 97a which is the vertical cross-section and Figure 97b which is the horizontal cross-section that the resin to the aluminum interface is not flat and variation can be seen. The locations for both vertical and horizontal cross-sections are indicated as green and blue line respectively in Figure 97c.

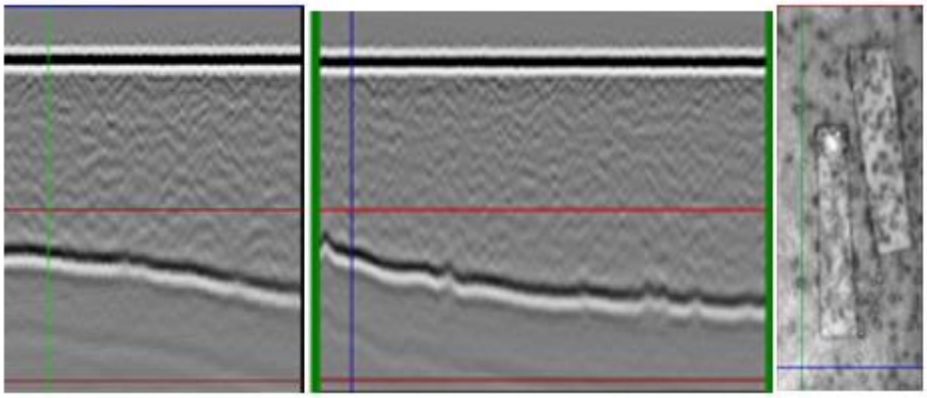

(a) (b) (c)

**Figure 97: (a) Vertical cross-section view (b) horizontal cross-section view (c) C-scan showing the vertical criss-section location (green line) and horizontal cross-section location (blue line)**

## 6.7 Selective Correction: Applying Transfer Function Based on Threshold & Particle Presence

As discussed in section 6.5, the transfer function was applied to the patterned image only in areas where particles were detected. A thickness of 855um was used to create the parametric model and the particle model was developed with the particle in the

middle. The original image and the resulting corrected image are shown in Figure 98a and Figure 98b respectively. The image seemed a little improved as shown in Figure 97b. The particle around the right edge of the image seemed to have blended well with the background.

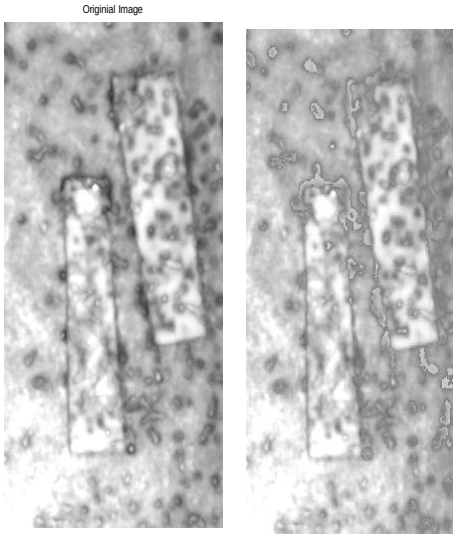


(a) (b)

**Figure 98:(a) original image (b) corrected image with resin thickness of 855um**

The contrast ratio was computed on 10 different particle locations before and after the transfer function was applied. This can be seen in Table 12. The contrast ratio before correction is in the range of 1.33-2.28. The contrast ration after correction is in the range of 0.932-1.024.

**Table 12: Contrast Ratio on a C-scan image from a patterned sample**

| Particle No. | Pixel Intensity (Before) | Pixel Intensity (After) | Background Intensity | Contrast Ratio (Before) | Contrast Ratio (After) |
|---|---|---|---|---|---|
| 1 | 44 | 75.1011 | 70 | 1.590909091 | 0.932076894 |
| 2 | 41 | 67.3201 | 69 | 1.682926829 | 1.024953914 |
| 3 | 41 | 75.9933 | 75 | 1.829268293 | 0.986929111 |
| 4 | 42 | 76.3892 | 72 | 1.714285714 | 0.942541616 |
| 5 | 48 | 73.8176 | 67 | 1.395833333 | 0.907642622 |
| 6 | 51 | 66.468 | 68 | 1.333333333 | 1.023048685 |
| 7 | 28 | 64.789 | 64 | 2.285714286 | 0.987822007 |
| 8 | 49 | 75.7822 | 74 | 1.510204082 | 0.976482604 |
| 9 | 45 | 82.4482 | 81 | 1.8 | 0.982435032 |
| 10 | 51 | 75.6181 | 76 | 1.490196078 | 1.005050378 |
| | | | Mean | 1.663267104 | 0.976898286 |
| | | | Std. Deviation | 0.273998549 | 0.036699048 |

# CHAPTER 7: CONCLUSIONS

## 7.1 Discussion

Literature research was conducted to get an understanding of past and current work to improve non-destructive ultrasonic images of bulk materials in the presence of filler particles. The first paper on signal scattering dates back to the 1970s.

Signal scattering in various applications have been studied previously. This includes ultrasonic signal scattering in medical tissue imaging, scattering in industrial applications where materials such as stainless steel, titanium, concrete etc., have been studied.

Various parametric models were explored, but a Gaussian model was selected to develop the model for ultrasonic reflections from clean resin sample as well as reflections from a resin sample with filler particles (glass beads) at a single x-y location. The signals were analyzed in the frequency domain to understand the effect due to presence of a particle. It was determined that for a given sample thickness around 850um, one filler particle caused the power of the signal to reduce by at least a third at that particular x-y location compared to a case with no particles. Any additional particles in depth at the same x-y location had a negligible impact on the power of the signal. The depth of the particle also did not have any noticeable effect. For particle sizes in the range of 50um-250um, there was marginal reduction in signal power with increase in particle size.

A significant amount of work has been done and contributed to the mitigation of noise caused by scattering. A few popular techniques such as time averaging, split spectrum processing with polarity thresholding, cross-correlation, wavelet transform, adaptive filtering, deconvolution and inverse filtering etc., have been studied. A method of particular interest was Inverse Filtering. In order to implement this technique, the ultrasonic reflections in resin material with and without filler particles that were modeled were used. The poles and zeros of the noise transfer function were analyzed. It was determined that the poles were not affected by the presence of the particle. Various cases of particle sizes were studied to understand the effect on the zeros. As the particle size increased, the number of zeros in the right hand plane increased. For the sample thickness of 830um and particle sizes of 77um, 232um and 383um, the frequency response of the transfer function was studied. There was some change in magnitude at some random frequencies but it did not provide any insight into the effect of particle size on the frequency response.

A 3-dimensional matrix array was developed to mimic a sample with various x- y positions on the sample and also depth, z. The top and bottom rows of the matrix are always populated with "0" as it is assumed that there is never a particle protruding out of the surface or the backwall. The presence of a "1" in the array indicates the presence of a particle in that layer at that depth. In order to mitigate the effect of the filler particle, first, the ultrasonic reflection in clean resin material and in resin material with filler particles were modeled. These modeled signals were converted into frequency domain to develop a transfer function.

This transfer function was applied to the frequency domain version of the modeled signal with a particle. The backwall signal was restored. This test was repeated on various cases of particle positions. The signal was restored successfully. This demonstrated that in many cases the correction based on a single particle depth can be applied effectively to situations where the actual depth of the particle varies. The error between the restored signal and ideal signal for each case was computed. The mean square error was also computed. It was determined that the transfer function based on the particle in the middle had the lowest mean square error. This transfer function was used for additional analysis. The c-scan image from the backwall was constructed based on the simulated resin sample with four particles each at different depths and different x-y location. The transfer function based on the particle in the middle was applied to raw modeled data and the image was again reconstructed. The shadow effect due to the presence of the particle was mitigated. The contrast ratio between the background and the particle locations were computed to be in the range of 0.958-1.003.

A clean resin sample was prepared and the ultrasonic reflection from the sample was compared to the modeled reflection from a clean resin sample. There was 95% correlation with the front surface reflection and 93% correlation with the backwall. Resin samples with filler particles mixed into it before curing were prepared. The resulting ultrasonic backwall reflections in the presence of these fillers were compared to both the parametric model and also the signal from the clean resin sample. The reflections in the presence of the fillers were obstructed and the resulting backwall reflections of interest

were very weak. The presence of filler particles in resin material scattered the ultrasound and affected the quality of the resulting backwall image.

The transfer function generated based on the particle in the middle was applied to the raw a-scan data from the real resin sample with filler particles. The corrected signals were used to reconstruct the image. The shadow effect due to the presence of the filler particles was mitigated. Most of the bright spots (voids) that are defects were not affected and visible in the corrected image. However, some of the voids were not clearly visible. A gray scale variation was noted from the bottom left corner of the image to the top right corner. B-scans were performed on the sample to note that the sample is not of uniform thickness and slight variation was noted. This variation attributed to over correction in some areas and under correction in some causing a gray scale variation.

To overcome this effect, a selective correction method was explored. The algorithm checks for a reduction in backwall intensity as well as a presence of a signal in between the front surface and back wall reflection to determine that there is a particle in the path of the Ultrasound before applying the transfer function. The resulting image showed correction in areas where shadows due to presence of particles were noted earlier. The contrast ratio before correction is in the range of 2.1-4.35. The contrast ratio after correction is in the range of 0.96-1.013. However, a dark ring like boundary was noted for most of the corrected areas. This is most likely due to the curvature of the particle. When the ultrasound hits the boundary of the particle, the resulting signal is of a weak amplitude due to scattering and a signal is not registered in between the front surface and the backwall.

As a test to see how this technique performs on a sample with a pattern on the backwall, a sample was created with tape attached on to an Aluminum substrate. Resin was poured over this substrate and particles were mixed into it prior to curing the sample. The transfer function created from the model with particle in the middle was applied to this image. The resulting image showed the pattern on the substrate. Although care was taken to make sure that the resin had uniform thickness, the substrate had some thickness variation. The variation was more dramatic in this sample and therefore, the grayscale variation in the corrected image was also very significant.

The selective correction method was applied to the image and correction was made in areas where shadows of filler particles were noted. The contrast ratio before correction is in the range of 2.1-4.35. The contrast ration after correction is in the range of 0.90-1.02.

## 7.2 Limitations

The transfer function method is sensitive to variation in the thickness of the sample. When the transfer function is applied to an entire image where the thickness of the resin is not uniform and the image was reconstructed using the corrected data, the gray scale variation can be significant depending on the extent of the thickness change. The resulting image can look worse than what was originally available. After close observation, it is clear that the areas where particles were present have been corrected and signal was restored. It has been observed that for the transfer function method to be effective, the thickness of the resin material has to be within a tight tolerance of a few microns. Thickness variation can result in over or under corrected signals.

## 7.3 Future Work

### 7.3.1 Thickness Variation

As noted in the previous section, during the analysis of the results from the patterned and un-patterned samples, it was found that the thickness variation in the resin can have a negative impact on the effectiveness of the transfer function implementation to mitigate the effect of filler particles. In order to overcome this issue, it would be ideal to incorporate a way to check the thickness of the resin in the real sample at every x-y location by measuring the time between the front surface and backwall reflections. This would provide the thickness information that can be used to adjust the model accordingly. Although, to implement such a solution in real time is going to be very time consuming, the resulting corrected image can show improvement. For industrial applications, such variations in material thicknesses are not common as samples are manufactured with equipment and processes to make sure that material thicknesses are within tight tolerances. It is recommended that further testing should be conducted and image quality evaluated to determine if there is any value is applying the transfer function to the entire image.

### 7.3.2 Selective Correction

When selective correction was applied based on the backwall amplitude threshold and the presence of a particle in the bulk, a ring was noted around the corrected area. This effect is most likely caused due to the curvature of the spherical filler particles. This problem is illustrated in Figure 99a.

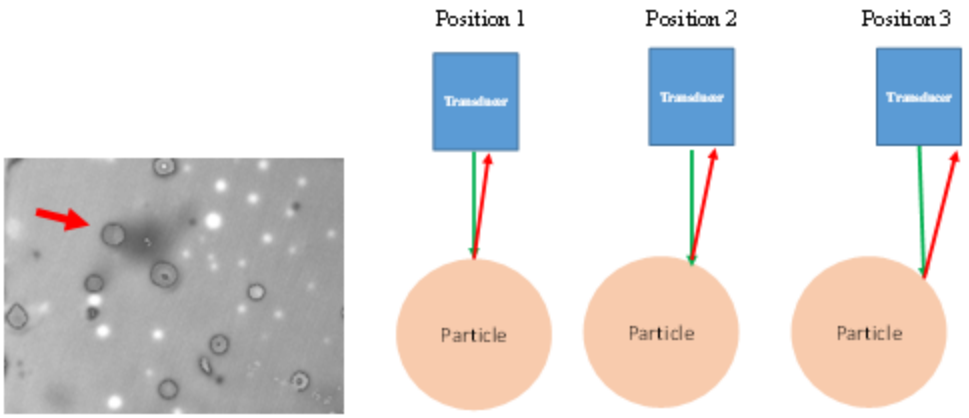


(a) (b)

**Figure 99: (a) Ring noted around the correction (b) Effect of curvature on the ultrasonic reflection**

When the transducer is right at the top most position of the sphere, the signal reflected back has the highest possible amplitude. As the transducer moves farther away in any direction (either in x, y or both) from this position, the reflected signal is going to get weaker. As the transducer moves to position 3 as shown in Figure 99b, almost no reflected signal is measured by the transducer as the signal completely scattered. In this position, although the backwall amplitude is below the threshold, a particle is not detected in the bulk as the signal reflected back from the particle is very weak also. Therefore, no correction is applied. This is the reason for a ring like pattern around the corrected areas. In order to address this issue, the following methods are proposed.

#### 7.3.2.1 Approach 1: Modeling Curvature

In this method, the curvature of the particles can be taken into account when modeling the parametric model with particles. Research has been conducted to study the

effect of curvature on ultrasonic reflection [85 86]. The effect of surface curvature on grain noise was discussed in [87]. The Curle's equation and acoustic scattering by a sphere is discussed in [88]. After taking curvature into account during modeling and generating the transfer function, the results should be analyzed and compared to the cases discussed in this dissertation.

#### 7.3.2.2 Approach 2: Spherical Particles

In this research work, spherical glass beads were used as filler particles. When a signal due to a particle is detected in the bulk of the material, the program needs to keep track of the maximum amplitude of the reflected signal from the particle as well as its x-y location on the image. Once the correction is completed on one particle, the maximum number of corrected pixels in either x or y are determined. As an example, the top view of a particle is shown in Figure 100. A maximum of eleven corrections are made along the x axis and each pixel is 20um. The total corrected length (diameter) is 220um. It has been estimated from the image in Figure 100 that the ring is approximately 20um. It is estimated that the particle is ~250um. Therefore, the program performs a correction on one additional pixel around the entire particle to compensate for the curvature of the particle. The maximum number of corrected pixels along the x-axis is now 13 making the total corrected length to be 260um.

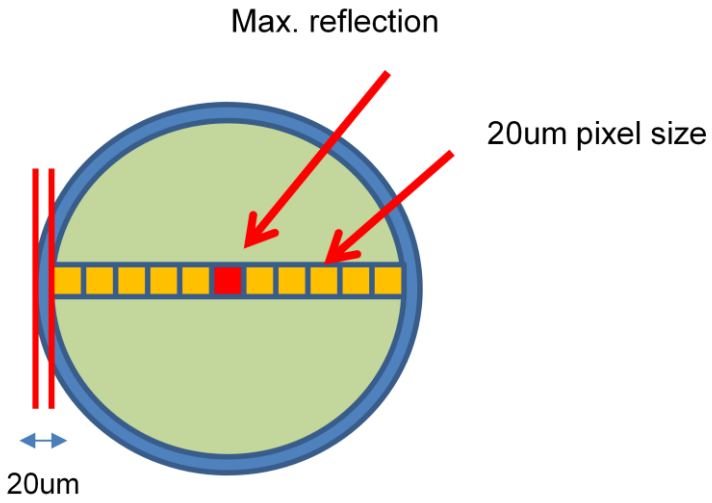


**Figure 100: Top view of the spherical particle with correction**

If filler particles are of different shapes such as oval, then this technique will have to be improvised as the book-keeping mechanism becomes more complex and tedious to implement. Therefore, another technique called a neighborhood algorithm is discussed in the next section.

#### 7.3.2.3 Approach 3: Oval Particles – Neighborhood Algorithm

When a particle is oval in shape, the ring around the particle may not be of uniform width and this is illustrated in Figure 101.

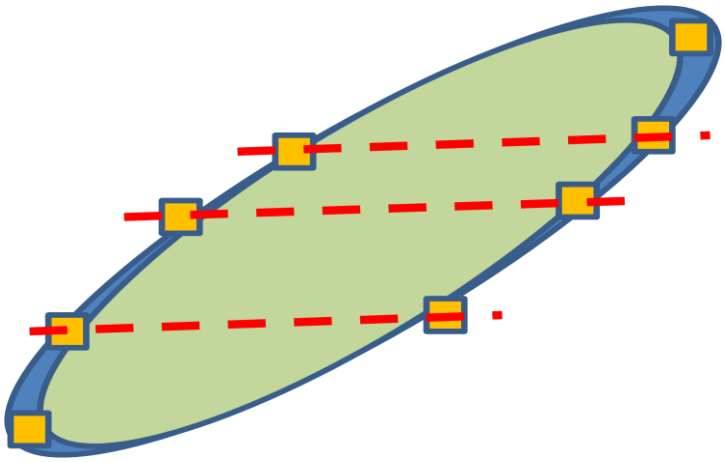

**Figure 101: Topview of oval particle with correction**

In this approach, a user defined neighborhood value “n” is used to determine the number of additional pixels on each side of the particle in a scan line that are corrected. When a particle is detected for the first time in a scan line, the program automatically corrects “n” pixels before the particle in that scan line as well as “n” pixels after the last time the particle is detected in the same scan line. An illustration of a case without neighborhood algorithm when n=0 is shown in Figure 102a. The orange boxes indicate the pixels when a particle is detected. A case with neighborhood algorithm when n=1 is shown in Figure 102b. Once again, the orange boxes indicate pixels when a particle is detected. The green boxes indicate the additional pixels that are corrected as determine by the neighborhood value "n".

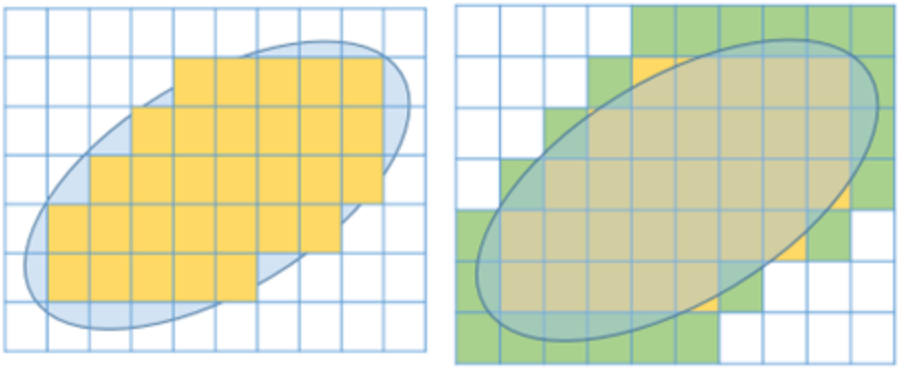

(a) (b)

**Figure 102: (a) Topview of oval particle correction without neighborhood algorithm (n=0) (b) Topview of oval particle correction with neighborhood algorithm (n=1)**

Hopefully, some of these suggested techniques for future work can provide further improvement to the work discussed in this dissertation.

## REFERENCES


1. Sannie, J., Wang, T., Bigutay, N.M., "Analysis of Homomorphic Processing from Ultrasonic Grain Signal Characterization", IEEE Transaction on Ultrasonics, Ferroelectrics and Frequency Control,, Vol. 36, No. 3. May 1999, 365-375

2. Karaojiuzt, M. Defect detection in concrete using split spectrum processing. Ultrasonics, IEEE Symposium (IUS). (1998) , 1 p. 843 - 846.

3. Zhang, G., & Harvey, D. (2012). Contemporary ultrasonic signal processing approaches for nondestructive evaluation of multilayered structures. Nondestructive Testing and Evaluation, 27(1), 1-27.

4. Lazaridis, P., Digalakis, V. V., " Space-Time Linear Predictive Filtering for the Improvement of Signal-To-Noise Ratio in Ultrasonic Imaging", 1991 IEEE, Ultrasonics Symposium, 795-798

5. Newhouse, V.L., Bilgutay, N.M., Saniie, J. and Fergason, E.S. Flaw-to-grain echo enhancement by spilt-spectrum processing Ultrasonics (1982) 20 59-68

6. Karpur, P., Shankar, P.M., Rose, J.L., and Newhouse,V.L., Split-spectrum processing: optimizing the processing parameters using minimization Ultrasonics (1987) 25 204-208

7. Bilgutay, N.M., Newhouse, V.L., and Fergason, E.S. Flaw visibility enhancement by split-spectrum processing techniques Proc 1981 IEEE Ultrasonics Symp (1981) 878-883

8. Bilgutay, N.M., Saniie, J., Furgason, E.S. and Newhouse, V.L., Flaw-to-grain echo echancement Ultrasonics International 1979 Butterworth Scientific, Guildford Surrey, UK (1979) 152-157

9. Li Yue and Ying Ching-Fu Two signal processing techniques for the enhancement of the flaw-to-grain echo ratio Ultrasonics (1987) Vol 25 March 90-94

10. Karpur, P., Shankar, P.M., Rose, J.L., and Newhouse,V.L., Split-spectrum processing: determination of the available bandwidth for spectral splitting Ultrasonics (1988) 26 204-209

11. Bilgutay, N.M., Bencharit, U., Murthy, R. and Saniie, J. Analysis of a non-linear frequency diverse clutter suppression algorithm Ultrasonics (1990) 28 90-96

12. Yong, Zhu and John P. Weight Ultrasonic Nondestructive Evaluation of Highly Scattering Materials Using Adaptive Filtering and Detection IEEE Transactions on Ultrasonics, Ferroelectrics, and Frequency Control, Vol. 41, No 1, January 1994.

13. Izquierdo, M.A.G, Hernández, M.G, Anaya, J.J, & Martinez, O. (2004). Speckle reduction by energy time–frequency filtering. Ultrasonics, 42(1), 843-846

14. M. G. Pecht, L. T. Nguyen, and E. B. Hakim, Eds., Plastic Encapsulated Microelectronics. New York: Wiley, 1995.

15. L. Lantz, S. Hwang, and M. Pecht, "Characterization of plastic encapsulant materials as a baseline for quality assessment and reliability testing," Microelectron. Rel., vol. 42, pp. 1163–1170, 2002.

16. Matz, Vaclav, Smid, Radislav, Starman, Stanislav, & Kreidl, Marcel. (2009). Signal-to-noise ratio enhancement based on wavelet filtering in ultrasonic testing. Ultrasonics, 49(8), 752-759.

17. https://www.nde-ed.org/EducationResources/CommunityCollege/ Ultrasonics/ EquipmentTrans/DataPres.htm

18. Olin, B., & Meeker, W. (1996). Applications of Statistical Methods to Nondestructive Evaluation. Technometrics, 38(2), 95-112.

19. Lu, Y., & Ahn, I. (2011). Comparison of time frequency analysis techniques for ultrasonic NDE signal.Electro/Information Technology (EIT), 2011 IEEE International Conference on, 1-6.

20. Bedetti, T., Dorval, V., Jenson, F., & Derode, A. (2013). Characterisation of ultrasonic structural noise in multiple scattering media using phased arrays. Journal of Physics: Conference Series, 457(1), 12.

21. Li, X., Murthy, R., Donohue, K., Bilgutay, N.M., Adaptive and Robust Filtering Techniques for Ultrasonic Flaw Detection, 1989 IEEE, Ultraosonics Symposium, 1145-1149

22. R. Demirli, J. Saniie, “Model-Based Estimation of Ultrasonic Echoes, Part I: Analysis and Algorithms,” IEEE Transactions on Ultrasonics, Ferroelectrics, and Frequency Control, vo. 48, no. 3, pp. 787-802, May 2001.

23. R. Freemantle, R. Challis, and J. White, “A Z-Transform Technique for Thin-Layer Reverberation Cancellation Applied to Ultrasonic NDT of Adhered Structures,” IEE Colloquium on Advanced Techniques for Collection and Interpretation of NDT Data, vol, 102, pp. 7/1-4, 1994.

24. T. Kundu, “Complete Acoustic Microscopial Analysis of Multilayered Specimens” J. Appl. Mech., vol. 59, no. 1, pp.54-60, 1992.

25. V. Kinra, and V.Iyer, “Ultrasonic Measurement of the Thickness, Phase Velocity, Density or Attenuation of a Thin-Viscoelastic Plate. Part I: The Forward Problem” Ultrasonics, vol. 33, no. 2, pp.95-109, 1995.

26. ——, “Ultrasonic Measurement of the Thickness, Phase Velocity, Density or Attenuation of a Thin-Viscoelastic Plate. Part II: The Inverse Problem,” Ultrasonics, vol. 33, no. 2, pp. 111–122, 1995.

27. S. Rokhlin and W. Huang, “Ultrasonic Wave Interaction with a Thin Anisotropic Layer between Two Anisotropic Solids: Exact and Asymptotic-Boundary-Condition Methods,” J. Acoust. Soc. Am., vol. 92. no. 3, pp. 1729-42, 1992.

28. R. Demirli, J. Saniie, “Model-Based Estimation of Ultrasonic Echoes, Part II: Nondestructive Evaluation Applications,” IEEE Transactions on Ultrasonics, Ferroelectrics, and Frequency Control, vo. 48, no. 3, pp. 803-811, May 2001.

29. C.A. Zala, “High Resolution Inversion of Ultrasonic Traces,” IEEE Trans. Ultras., Ferroel. Freq. Control, vol. 39, n. 4, 1992, pp. 458-463.

30. L.W. Schmerr, Jr., Fundamentals of Ultrasonic Nondestructive Evaluation. A Modeling Approach, Plenum Press, NY, 1998.

31. C. Zhu and V.K. Kinra, “A Time-Domain technique for Ultrasonic NDE of Thin Layered Media,” Review of Progress in QNDE, vol. 13, 1994, pp. 165-172

32. F. Hagglund, “Characterization of Thin Multi-Layered Materials Using Ultrasound,” Doctoral Thesis, Lulea Univeristy of Technology, Lulea, Sweden.

33. Zhiwei Hou, Z., Qiufeng Li, Q., Jie Chen, J., & Dong Gong, D. (2010). "Research on improving time-domain resolution of pulse-echo methods by compensation filtering". Mechatronics and Automation (ICMA), 2010 International Conference on, 1880-1885

34. Michael, F., Insana, Robert, F. Wagner, David, G. Brown, Timothy, J., Hall (1990). "Describing small-scale structure in random media using pulse-echo ultrasound". The Journal of Acoustical Society of America, Vol. 87, No.1, 179-192.

35. S. Kraus and K. Goebbels, "Improvement of signal-to-noise ratio for the ultrasonic testing of coarse grained materials by signal averaging techniques," in Proc. First Int. Symp. Ultrason. Mater Charact., Gaithersburg, June 7-9, 1978.

36. P. M. Shankar, U. Bencharit, N. M. Bilgutay, and J. Saniie, "Grain noise suppression through bandpass filtering," Materials Evaluation, vol. 46, pp. 1100-1104, July 1988.

37. R. Murthy, N. M. Bilgutay, and J. Saniie, "Application of bandpass filtering in ultrasonic nondestructive testing," Review of Progress in Quantitative Nondestructive Evaluation of Materials (QNDE), vol. 8, pp. 75S767, 1989.

38. V. L. Newhouse, N. M. Bilgutay, J. Saniie, and E. S. Furgason, "Flawto-grain echo enhancement by split-spectrum processing," Ultrasonics, vol. 20, pp. 59-68, Mar. 1982.

39. N. M. Bilgutay and J. Saniie, "The effect of grain size on flaw visibility enhancement using split-spectrum processing," Materials Evaluation, vol. 42, pp. 808-814, May 1984.

40. L. Yue er. al., Two signal processing techniques for the enhancement of the flaw-to-grain echo ratio, Ultrasonics, vol. 25, pp. 90-94, Mar. 1987.

41. V. L. Newhouse, et. al., "A real time split spectrum processing system,'' Ultrasonics Internat. I989 Conf. Proc.. pp. 4346, 1989.

42. N. M. Bilgutay, et al., "Analysis of a nonlinear frequency diverse clutter suppression algorithm," Ultrasonics, vol. 28, pp. 90-96, 1990.

43. V. L. Newhouse, er al., "Split spectrum processing: performance of the polarity-thresholding algorithm in signal-to-noise ratio enhancement in ultrasonic applications," Rev. Quantitative NDE, vol. 7A, pp. 865-874,1988.

44. P. Karpur, et. al., “Split spectrum processing: determination of the available bandwidth for spectral splitting,” Ultrasonics, vol. 26, pp. 204-209, July 1988.

45. J. L. Rose, P. Karpur, and V. L. Newhouse, “Utility of split-spectrum processing in ultrasonic nondestructive evaluation,” Materials Evaluation, vol. 46, Jan. 1988

46. Bazulin, E. (2013). Reconstruction of the images of reflectors from ultrasonic echo signals using the maximum-entropy method. Russian Journal of Nondestructive Testing, 49(1), 26-48.

47. Bazulin, A., & Bazulin, E. (2009). Deconvolution of complex echo signals by the maximum entropy method in ultrasonic nondestructive inspection. Acoustical Physics,55(6), 832-842.

48. Chiou, Chien - Ping, Thompson, R. Bruce, & Schmerr, Lester W. (1993). Model-based signal processing techniques for ultrasonic flaw detection: Simulation studies.

49. Zhang, G., & Harvey, D. (2012). Contemporary ultrasonic signal processing approaches for nondestructive evaluation of multilayered structures. Nondestructive Testing and Evaluation, 27(1), 1-27.

50. Bilgutay, N., Popovics, J., Papovics, S., Karaoguz, M., "Recent Developments in Concrete Non Destructive Evaluation", IEEE 2009, 3393-3396

51. Bilgutay, N.M., Bencharit., U., Saniie, J.,"Enhanced Ultraonic Imaging using Split Spectrum Processing and Polarity Thresholding", IEEE Transactions on Acoustics, Speech, And Signal Processing, Vol, 37, No.10, October 1989

52. Li, X., Bilgutay, N., & Murthy, R. (1992). Spectral histogram using the minimization algorithm-theory and applications to flaw detection. Ultrasonics, Ferroelectrics and Frequency Control, IEEE Transactions on, 39(2), 279-284.

53. Gustafsson, M.G. Nonlinear clutter suppression using split spectrum processing and optimal detection. IEEE transactions on ultrasonics, ferroelectrics, and frequency control. (01/1996) , 43 (1), p. 109 - 124

54. S . S. Wolff, J . B. Thomas, and T. R. Williams, “The polarity-coincidence correlator: A nonparametric detection device,” IRE Trans. Irrform. Theory, vol. IT-8, pp. 5-9. Jan. 1965.

55. J . L. Rose, P. Karpur. and V. L. Newhouse. “Utility of split spectrum processing in NDE,” presented ASNT Fall 1986 Conference, Iiew Orleans, LA, Oct. 3-5, 1986.

56. Oppenheim, A V and Schafer, R W, 'Discrete-Time Signal Processing', Prentice-Hall, 1989, p66

57. Chen, Hanxin, Zuo, Ming J., Wang, Xiaodong, & Hoseini, Mohammad R. (2010). An adaptive Morlet wavelet filter for time-of-flight estimation in ultrasonic damage assessment. Measurement, 43(4), 570-585

58. Hoseini, Mohammad R., Zuo, Ming J., & Wang, Xiaodong. (2012). Denoising ultrasonic pulse-echo signal using two-dimensional analytic wavelet thresholding. Measurement, 45(3), 255.

59. Rodríguez, M.A, San Emeterio, J.L, Lázaro, J.C, & Ramos, A. (2004). Ultrasonic flaw detection in NDE of highly scattering materials using wavelet and Wigner–Ville transform processing. Ultrasonics, 42(1), 847-851

60. Chen, Y., & Raheja, A. (2005). Wavelet lifting for speckle noise reduction in ultrasound images. Conference Proceedings : Annual International Conference of the IEEE Engineering in Medicine and Biology Society. IEEE Engineering in Medicine and Biology Society. Annual Conference, 3, 3129-32.

61. Chen, C.H., "Application of Wavelet Transforms to Ultrasonic NDE and Remote-Sensing Signal Analysis"., IEEE, 1994. 472-475

62. P S Addison, ‘The illustrated wavelet transform handbook’, IOP Publishing Ltd. ISBN: 0 7503 0692 0, 2002

63. D Pagodinas, ‘Ultrasonic signal processing methods fordetection of defects in composite materials’, ISSN 1392-2114, Ultragarsas, No 4 (45), 2002.

64. R Drai, M Khelil and A Benchaala, ‘Time frequency and wavelet transform applied to selected problems in ultrasonics NDE’, NDT and E International, Vol 35, No 8, pp 567-572, December 2002.

65. R Drai, M Khelil and A Benchaala, ‘Flaw detection in ultrasonics using wavelets transform and split spectrum processing’, 15th World Conference on NDT, Rome, 2000.

66. J N Watson, P S Addison and A Sibbald, 'Temporal filtering of NDT data using wavelet transforms', Proceedings of the 16th World Conference on NDT, Montreal, Canada, September 2004.

67. K I Park, U S Park, H K Ahn, S I Kwun and J W Byeon, 'Experimental wavelet analysis and applications to ultrasonic non-destructive evaluation', 15th World Conference on NDT, Rome, 2000.

68. C H Chen, W L Hsu and S K Sin, 'A comparison of wavelet deconvolution techniques for ultrasonic NDT', International Conference on Acoustics, Speech, and Signal Processing, New York, April 1988.

69. S Legendre, D Massicotte, J Goyette, and T K Bose, 'Wavelet transform based method of analysis for Lamb-wave ultrasonic NDE signals', IEEE Trans. Instrum. Meas, 49, 3: 524-530,2000.

70. Yang, Wen-Xian, Hull, J.Barry, & Seymour, M.D. (2004). A contribution to the applicability of complex wavelet analysis of ultrasonic signals. NDT and E International, 37(6), 497-504.

71. W.X. Yang, J.B. Hull, M.D. Seymour, A contribution to the applicability of complex wavelet analysis of ultrasonic signals, NDT&E International 37 (2004) 497–504.

72. S. Song, P. Que, Wavelet based noise suppression technique and its application to ultrasonic flaw detection, Ultrasonics 44 (2006) 180– 193.

73. R.R. Coifman, D.L. Donoho, Translation-invariant de-noising, in: Wavelets and StatisticsLecture Notes in Statistics, 103, Springer- Verlag, 1995, pp. 125 -150.

74. G.P. Nason, B.W. Silverman, The stationary wavelet transform and some statistical applications, in: Wavelets and StatisticsLecture Notes in Statistics, 103, Springer-Verlag, 1995, pp. 281–299.

75. M. Lang, H. Guo, J.E. Odegard, C.S. Burrus, Noise reduction using an undecimated discrete wavelet transform, IEEE Signal Processing Letters 3 (1996) 10–12

76. Abbate, J. Koay, J. Frankel, S.C. Schroeder, P. Das, Signal detection and noise suppression using a wavelet transform signal processor: application to ultrasonic flaw detection, IEEE Trans. Ultrason. Ferroelec. Freq. Control 44 (1997) 14–25.

77. J.C. Lazaro, J.L. San Emeterio, A. Ramos, J.L. Fernandez, Influence of thresholding procedures in ultrasonic grain noise reduction using wavelets, Ultrasonics 40 (2002) 263–267

78. E Kazanavicius, A Mikuckas and I Mikuckiene, 'Wavelet transform based signal processing method for nondestructive testing', Proc. IEEE International Symposium on Intelligent Control, Houston, Texas, Oct 5-8, 2003

79. Bamber. J.C., Daft., C., Adaptive filtering for reduction of speckle in ultrasonic pulse-echo images, Ultrasonics, January, 1986, 41-44

80. B. Widrow, et. al.. "Adaptive noise cancelling: Principles and applications," Proc. IEEE, vol. 63, pp. 1692-1716, Dec. 1975. [I61

81. B. Widrow and S. D. Steams, "Adaptive signal processing." Englewood Cliffs, NJ: Prentice-Hall, 1985

82. Yong Zhu, & Weight. (1994). Ultrasonic nondestructive evaluation of highly scattering materials using adaptive filtering and detection. Ultrasonics, Ferroelectrics and Frequency Control, IEEE Transactions on, 41(1), 26-33.

83. Ali, M., & Elsayed, G. (2013). Reflectivity function reconstruction using the frequency deconvolution technique. Acoustical Physics, 59(5), 580-583

84. Izquierdo, M.A.G., Anaya, J.J., Martínez, O., & Ibañez, A. (1999). Multi-pattern adaptive inverse filter for real-time deconvolution of ultrasonic signals in scattering media. Sensors & Actuators: A. Physical,76(1), 26-31.

85. Spies, M. (1999). "Simulation of ultrasonic testing of complex-structured materials and components".Ultrasonics Symposium, 1999. Proceedings. 1999 IEEE, 1, 791-800

86. Chen, H., Luo, X., & Ma, H. (2007). "Scattering of elastic waves by elastic spheres in a NaCl-type phononic crystal". Physical Review B, 75(2), 024306.

87. Margetan, Frank J., Yalda, Isaac, Thompson, R. Bruce, Umbach, J., Suh, U., Howard, P. J., . . . Gilmore, R. (1997). "Ultrasonic Grain Noise Modeling: Recent Applications to Engine Titanium Inspections".

88. Davis, A., & Nagem, R. (2006). "Curle's equation and acoustic scattering by a sphere". The Journal of the Acoustical Society of America, 119(4), 2018-26.

## BIOGRAPHY

Shwetha Jakkidi has worked in the non-destructive inspection area for more than 10 years. She graduated with a Master of Science degree in Electrical and Computer Engineering from George Mason University in 2002 and Bachelor of Engineering degree in Electronics and Computer Engineering from Manukau Institute of Technology, Auckland, New Zealand in 2000. Shwetha worked with Sonix, Inc for 11 years and has been a liaison between industry needs and Sonix, an Ultrasonic Inspection equipment manufacturer.

## LIST OF PUBLICATIONS

Jakkidi. S., Cook, G., McKeon, J. C.P.," Ultrasound Material Characterization of Complex Matrix Material and Mitigation of Noise using Signal Processing Techniques", ASNT 24th Research Symposium March 19th 2015

Jakkidi, S, & Cook, Gerald. (2005). Landmine geo-location using dynamic modeling and get tracking.(Author Abstract). IEEE Transactions on Aerospace and Electronic Systems, 41(1), 51.

Jakkidi, S.; Cook, G., "Geo-location of detected landmines via mobile robots equipped with multiple sensors," IECON 02 [Industrial Electronics Society, IEEE 2002 28th Annual Conference of the] , vol.3, no., pp.1972,1977 vol.3, 5-8 Nov. 2002

Cook, G., Jakkidi, S., Kansal, S., Sherbondy, K.D., Amazeen, C., "Impact of uneven terrain on geo-location errors for mines detected via vehicular mounted sensors", Proc. SPIE 4742, Detection and Remediation Technologies for Mines and Minelike Targets VII, (13 August 2002);